VELOCITY MAP IMAGING: FROM GASES TO SURFACES

A thesis submitted to The University of Manchester for the degree of
Doctor of Philosophy
in the Faculty of Engineering and Physical Sciences

2013

MIKE REID

SCHOOL OF CHEMISTRY

Contents

Word Count: 37,849

List of Figures

List of Tables

Abstract

Velocity Map Imaging: From Gases to Surfaces

Doctor of Philosophy, The University of Manchester

Mike Reid, *July 2013*

A standard velocity map imaging (VMI) spectrometer makes use of three electrodes and produces VMI focussing conditions over a region of space only one to two mm in diameter. This is more than acceptable for a standard gas phase photodissociation (the archetypal VMI experiment) since all of the products are produced and ionised within the region defined by the intersection of a laser beam with a molecular beam, typically one mm or so wide.

However, the great benefit of VMI (its excellent velocity resolution) cannot reliably be obtained in other reaction dynamics studies, such as those involving surface desorptions, since the product fragments are scattered into, and typically ionised over, a much larger region of space than that in which the VMI conditions exist.

This thesis outlines the first systematic study of the relationship between "weak extraction" and the area over which VMI focussing conditions remain valid, and shows that, by making use of weak extraction, the VMI focussing conditions produced by our apparatus prevail over an area $\sim$12 mm in diameter.

A new VMI spectrometer has been constructed and used to study the near threshold photodissociation of chloroform. The potential to use the apparatus for surface VMI studies was then investigated. This document contains an overview of gas phase photodissociation processes and the development of the VMI technique, followed by a detailed description of the newly constructed apparatus. A study of the photodissociation of chloroform ($CHCl_3$) in the gas phase, and experiments and simulations which were carried out in order to determine the feasibility of adapting the spectrometer for surfaces are discussed. Finally, a description of the necessary modifications which were made to the apparatus in order to enable surface experiments is provided.

Declaration

No portion of the work referred to in this thesis has been submitted in support of an application for another degree or qualification of this or any other university or other institute of learning.

Copyright Statement

University Library, The University Library's regulations (see http://www.manchester.ac.uk/library/aboutus/regulations) and in The University's policy on Presentation of Theses.

Acknowledgements

There are many people to whom I owe a great deal of gratitude for all their help, advice and support during the course of completing the research which constitutes this thesis.

The Photon Science Institute and its support staff, for providing the lab space in which I worked and for the long-term loan of the probe laser system, and Dr. Peter Gorry for donating his excimer laser to our group.

The MChem students who worked in the lab with me (Jenifer, Vignon and Vicki) kept me sane by giving me someone other than the equipment to talk to.

Dr. Chris Muryn was a seemingly endless source of spare parts when pieces of the kit inexplicably stopped working, and his advice on troubleshooting often came in useful and saved me some time.

The guys in the workshops for machining and wiring up various parts of the apparatus, and also for helping to repair things as needed (i.e. when I dropped them).

Prof. Simon Pimblott, for his help during my undergraduate work and for putting in a good word for me when I applied to work on this project.

My superviser Sven, for giving me the opportunity to work with him, for being ever ready to share his knowledge and expertise, for his constructive comments on my work and writing, for many interesting and valuable discussions and, most importantly, for his good nature and patience.

My friends, for making sure that on my time off I always enjoyed myself

and forgot about the lab for a while. In particular Lottes, for always being there to talk to.

My immediate and extended family, and my in-laws, for all their support and encouragement.

My mother, to whom I owe far more than I could ever write down.

Finally, Amber. For everything.

List of Abbreviations

BDE	*Bond Dissociation Energy*
CCD	*Charge Coupled Device*
COI	*Centre of Inversion*
FWHM	*Full Width at Half Maximum*
LIF	*Laser Induced Fluorescence*
MCP	*Micro Channel Plate*
MPI	*Multi Photon Ionisation*
MS	*Mass Spectrometry*
NS	*Newton Sphere*
PES	*Potential Energy Surface*
PFTS	*Photofragment Translational Spectroscopy*
PRS	*Photofragment Recoil Spectroscopy*
REMPI	*Resonance Enhanced Multi Photon Ionisation*
SHV	*Super High Voltage*
TOF	*Time Of Flight*
TOF-MS	*Time Of Fight Mass Spectrometry*
TTL	*Transistor Transistor Logic*
UHV	*Ultra High Vacuum*
UV	*Ultra Violet*
VMI	*Velocity Map Imaging*
YAG	*Yttrium Aluminium Garnet*

Chapter 1

Introduction

Reaction dynamics is concerned with the study of elementary chemical reactions, and aims to determine the mechanisms by which such fundamental processes occur. To ensure reliability and accuracy of the results obtained from reaction dynamics studies, the majority of experiments are concerned with isolated molecules (i.e. molecules in the gas phase).

It is a feature of reaction dynamics experiments that the internal quantum states and kinetic energies of the reactant and product molecules must be known as accurately as possible. The use of high resolution laser spectroscopy allows the internal energies of products to be determined. To determine the kinetic energies of gaseous products, one frequently used technique is velocity map imaging (VMI), which extracts the full three dimensional velocity distribution of the products from gas phase reactions, most typically from photodissociation reactions.

While studies of gas phase reactions are crucial due to the fact that they are the simplest system to study, and also because of their relevance to real world systems (e.g. in atmospheric chemistry), the dynamics of chemical processes in other phases is also hugely important. Surfaces, for example, are inherently more complex and therefore (arguably) more interesting than gases, and they play a key role in many areas of chemistry, such as in heterogeneous catalysis and in membrane processes in biological systems.

For a surface reaction dynamics study, the ideal situation would be to apply a powerful gas phase technique (e.g. VMI) to the surface in question. Indeed, several recent studies have done just this. However, it should be noted that a "standard" VMI spectrometer will not necessarily provide the conditions required to ensure that VMI's main advantage (high velocity resolution) can be brought to bear when studying surfaces. The problem, then, is to determine how a standard VMI spectrometer can be suitably adapted in order to allow surface dynamics to be studied with resolution comparable to that provided by VMI in the gas phase.

It has been known for some time that "weak extraction" can increase the region of space over which VMI can reliably be used, thus enabling its application to bimolecular (scattering) dynamics studies and, potentially, surface dynamics studies as well. However, none of the handful of groups who have published surface studies using VMI made use of weak extraction and, in addition, no direct investigation nor systematic experimental verification of the increased VMI area obtained with weak extraction have yet been carried out.

In order to determine the feasibility of using VMI for surface studies, a gas phase VMI spectrometer has been constructed which makes use of weak extraction. The apparatus was designed to ensure an optimal compromise between complexity and effectiveness. Experiments and simulations were carried out to determine whether or not weak extraction provides the necessary conditions to allow VMI to be fully effective when surface processes are studied. This work constitutes the only systematic study of the increased VMI area produced by using weak extraction conditions. This has important implications for experiments whose product fragments must be detected over a large area (surface desorptions, collisional dynamics etc). By characterising the weak extraction and VMI conditions, it has been shown that this newly constructed apparatus can go on to be reliably used for studying surface reaction dynamics with all the power of VMI.

This thesis begins with a general overview of photodissociation processes and of the evolution of the VMI technique. This is followed by a detailed description of the apparatus which has been constructed. A gas phase VMI study of the photodissociation of chloroform is included as an example of a "typical" VMI experiment, and also in order to illustrate what type of information can be obtained from VMI experiments. The experiments which characterised the VMI conditions are discussed in chapter 5 and, finally, a description of the modifications made to the apparatus which allow surfaces to be studied is included.

Chapter 2

Background

2.1 Reaction Dynamics

Chemical reaction dynamics is the study of chemical processes and is concerned with determining, in as much detail as possible, exactly what happens during an elementary chemical reaction. This is achieved by characterising reactants, products and transition states in terms of the velocities and energies of the atoms and molecules involved.[1] The importance of this field was recognised in 1986 when Herschbach, Lee and Polanyi were awarded the Nobel Prize "*...for their contributions concerning the dynamics of chemical elementary processes.*"[2]

In bimolecular reactions, two molecules collide, energy is transferred between them, and this energy transfer results in a rearrangement of the atoms in the system via the breaking of bonds and the formation of new compounds. Molecules can also collide without reacting, with (elastic) or without (inelastic) a change in their internal energy. Unimolecular reactions involve the decay of a single reactant into products, after interaction with a photon for example (a photodissociation reaction). The majority of reaction dynamics studies involve processes in the gas phase. Because gaseous molecules are isolated, the energy transfer between them can be studied with high resolution and without the complication of additional collisions obscuring or distorting information. Recently, interest in a phase somewhere between gases and liquids, termed "clusters," is increasing, as is interest in applying techniques which were traditionally used in the gas phase to other systems. Dynamics at surfaces are important: Gerhardt Ertl was awarded the Nobel prize for chemistry in 2007 "*...for his studies of chemical processes on solid surfaces*," which were carried out in order to illuminate the mechanisms of processes relevant to catalysis.[3] In recent years, photochemistry at solid surfaces has garnered much attention due to the desire to fabricate devices which can harvest solar energy.[4]

Determining how an elementary process takes place is not a simple task. Aside from determining the identity of the products, there are a number of

parameters which must be considered with regard to the reactant molecule(s). One quantum state of a molecule may react quite differently to another. The kinetic energy and the orientation of the reactants are also important. In bimolecular processes the reactants may need to have a minimum kinetic energy in order to overcome an activation barrier. In addition, reactants may need to collide at certain angles to ensure optimal overlap of the reactant atomic or molecular orbitals, and in unimolecular reactions involving absorption of a photon, the reactant molecule must be aligned correctly with respect to the photon's electric field in order to increase the probability of the photon being absorbed.

Having fully characterised these variables for the reactants, the products can then be analysed in terms of their internal and kinetic energies, and the directions in which they are travelling. With everything characterised, the results can be used to determine details about the underlying mechanism by which the reaction takes place, i.e. information about the potential energy surface(s) (PES) and transition states involved can be obtained.

In an ideal experiment, all variables relating to the reactant(s) would be controlled. Reactants would be prepared in a specific quantum state with full control over both their alignment and kinetic energy. After reacting, the product(s) would then be fully characterised using appropriate techniques, providing the ability to elucidate reaction mechanisms in great detail, and investigate the effects on the reaction of varying the initial parameters. The ultimate goal of reaction dynamics is to completely control the outcome of elementary reactions. While no experiment has yet been carried out in which every reactant variable has been parameterised and all product variables determined, huge strides have been made in the past few decades. A number of sophisticated techniques now exist, which have their roots in experiments reported in the middle of the 20^{th} century. Flash photolysis laid the foundation for all photochemical pump probe experiments, including the now ubiquitous imag-

ing techniques which have evolved from Time Of Flight Mass Spectrometry (TOF-MS).[5–9] Fluorescence detection, with the associated Doppler lineshape analysis methods, stems from the earliest reports of chemiluminescence from excited state product molecules by Polanyi.[10,11]

Modern techniques allow investigators to probe reaction mechanisms in great detail. For example, for a given reaction it is now possible to identify products produced with different quantum states. The presence of multiple reaction pathways is thus indicated, and the branching ratios between these pathways can often be quantified. Each product quantum state can then have its associated kinetic energy and angular distribution recorded, providing information on vector correlations (the mutual alignment of certain vector quantities which constitute experimental variables or parameters, e.g. laser polarisation, product angular distribution etc) for each reaction pathway.

The experimental technique with which this project is concerned is velocity map imaging (VMI), a method particularly suited to studying photodissociation dynamics. While it is a relatively recent development (it was first reported sixteen years ago), its roots can be traced back through a long line of techniques to the invention of mass spectrometry a century or so ago.

2.2 Photodissociation

2.2.1 A Simple Photodissociation

Before discussing VMI, a basic understanding of the photodissociation process is necessary and is provided here, having been drawn from the standard texts on the subject.[12,13] The simplest photodissociation process involves the direct dissociation of a diatomic "parent" molecule. The parent is initially in a stable (usually ground) electronic state, i.e. it resides on a "bound" potential energy surface. Upon absorption of a photon, an electronic excitation of the parent molecule occurs, promoting the parent to an unstable excited state (see Fig. 2.1). On this "repulsive" surface, the most stable molecular configuration is achieved by increasing the bond length to infinity. I.e. The bond breaks and the two atoms fly apart along the direction of the bond, thus maximising the distance between them.

A simple consideration of conservation of energy can show that the sum of the kinetic and internal energies of the parent molecule, as well as the energy of the photon, must equal the kinetic and internal energy of the fragments produced, less the energy required to break the bond:

$$E_{h\nu} + E_P = BDE_{AB} + E_{IntA} + E_{IntB} + E_{KinA} + E_{KinB}$$

E_{hv} is the photon energy; E_P is the total energy of the parent diatomic molecule (AB); BDE_{AB} is the bond dissociation energy of the A-B bond; E_{IntA}, E_{IntB}, E_{KinA} and E_{KinB} represent the internal and kinetic energies of the A and B fragments produced. If A and B are atomic fragments, their internal energies corresponds only to electronic states, if they are polyatomic they correspond to rotational, vibrational and electronic states. If the initial energy of the parent molecule, the BDE and the photon energy are known accurately, analysis of the external and internal energies of the products can

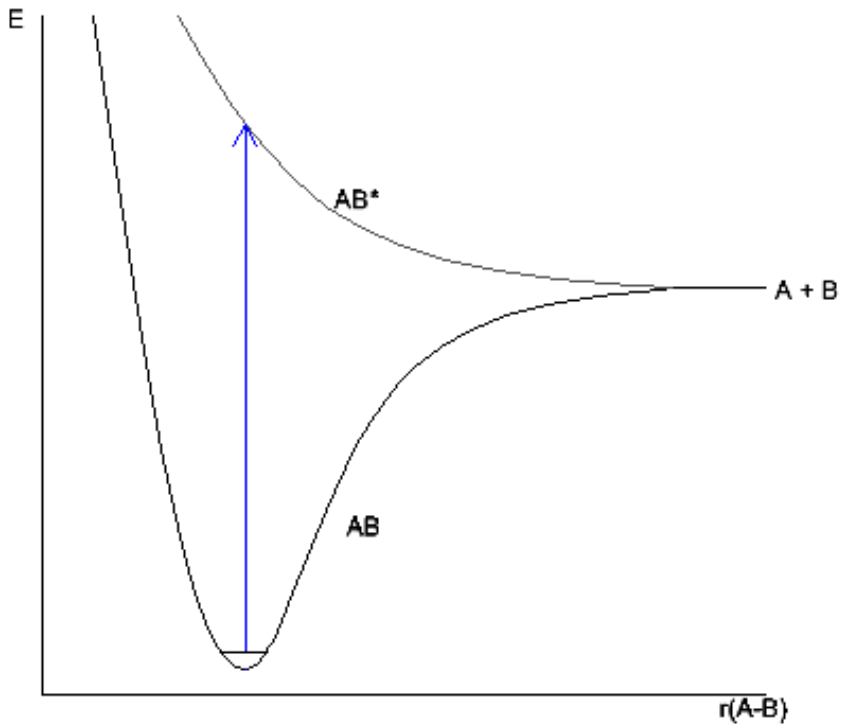

Figure 2.1: PESs involved in a simple photodissociation. A molecule in a stable (bound) state may be promoted to an unstable (repulsive) state by absorption of a photon (blue arrow) from which it dissociates.

provide information about the surfaces on, and mechanism by, which the dissociation process occurs.

Many photodissociation processes are much more complex than this simple picture. Polyatomic photofragments can have excess energy channelled into rotation and vibrational modes of excitation. In addition, the above description implies a dissociation involving only two PESs, however in some cases multiple excited PESs may be accessible. This can result in competition between multiple channels, each producing products with different internal and kinetic energies. Finally, the PES to which the photon promotes the reactant may not be purely repulsive; the reactant molecule may then undergo fast (on the order of femtoseconds to picoseconds) non-radiative transitions in order to access a repulsive PES before dissociation.[14] The presence of multiple prod-

uct channels is observable, and the branching ratios between them is often quantifiable, using imaging techniques.

2.2.2 Vector Correlations in Photodissociation

One of the main driving factors in the development of imaging techniques was the desire to be able to determine information on vector correlations in photodissociation.[15–19] There are three main vectors to be concerned with: E - the polarisation of the photon's electric field; μ - the transition dipole moment associated with the transition; V - the velocity of the photofragments.

An electromagnetic wave is composed of two perpendicular oscillating fields: one electric and one magnetic. They can be described by two vectors aligned perpendicular to one another, which are themselves perpendicular to the direction of propagation of the wave. The magnetic field can be disregarded for the purposes of this document; "polarisation" henceforth refers only to the electric field vector, E. In "normal" light these vectors are randomly aligned, but by using a laser source, linearly polarised light (light containing photons which all have E aligned together) can be produced. The polarisation can usually be amended to produce photons with E aligned at any desired angle. E is thus an experimentally defined parameter, and the alignments of the other vectors described here are correlated with the alignment of E.

For any transition between two quantum states of a molecule there exists a "transition dipole moment," μ. This is not simply a characteristic of the molecule (like an electric dipole moment), rather it is a parameter of the transition between two internal states of molecule, and depends on their symmetries. μ can lie either along the symmetry axis of the molecule, i.e. along the bond in a simple molecule (a diatomic), or perpendicular to it. The probability that a photon (of the correct energy) will be absorbed by a molecule is dependent on the angle, θ, between μ and E, and follows a $\cos^2\theta$ distribution. I.e. When μ and E are aligned parallel to one another the probability of absorption is 1,

when they are aligned perpendicularly the probability of absorption is 0.

μ is not an experimental observable, but it is correlated to an observable vector quantity: the recoil velocity of photofragments V. The alignment of μ can be determined by observing the correlation of E with V (known as E-μ-V correlation). There are two extreme cases when using polarised light: the fragments will fly apart along the bond axis, which is either parallel to E or perpendicular to it. The probability of a molecule absorbing a photon and thus dissociating, depends on its orientation: molecules aligned such that μ lies along E have a probability of one for absorption, those aligned such that μ lies perpendicular to E have a probability of absorption of zero. For molecules aligned such that μ lies at an angle between 0^o and 90^o with respect to E, the probability of absorption follows a $\cos^2$ distribution. Upon absorbing the photon the bond rapidly breaks and the fragments fly apart along the bond axis. If μ lies parallel to the bond (and therefore the bond is parallel to E) the fragments fly apart along the direction of E, if μ lies perpendicular to the bond, then the fragments fly apart along an axis perpendicular to E. Therefore, by examining the correlation between the experimental parameter E, and the experimental observable V, it is possible to determine the nature of μ for that particular transition, thereby shedding light on the nature of PESs involved in the dissociation.

The E-μ correlation was first formalised by Zare and Herschbach in 1963.[15] It was elegantly demonstrated experimentally four years later by Solomon's "photolysis mapping" technique. Fig. 2.2 shows a diagram of the apparatus used by Solomon.[20] The experiment involved coating the inside of a hemispherical glass bulb with tellurium and then filling it with a low pressure of the reactant molecules. A laser beam was directed through the bulb, and the radical photofragments produced were shown to etch the coating in well defined areas. This was the first experimental evidence for the anisotropy of photofragment velocity as a result of the E-μ-V correlation.

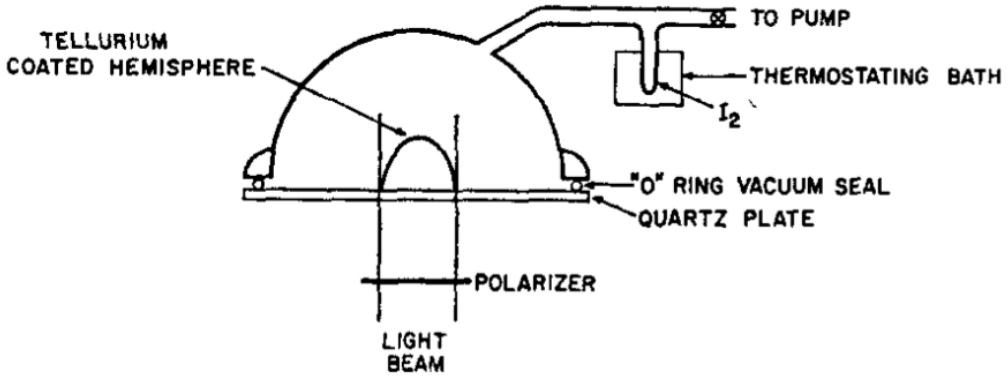

Figure 2.2: The apparatus used in Solomon's "Photolysis Mapping" experiment, which was the first to experimentally demonstrate the alignment of the transition dipole moment with the electric field vector of the dissociating photons.

2.2.3 The Angular Distribution of Photofragments

The recoil velocity, V, has two components: speed and direction. The speed is determined by the amount of energy from the photodissociation which is partitioned into translation of the fragments. The direction is a result of the E-μ-V correlation and is described by the anisotropy parameter:

$$I(\theta) = \frac{1 + \beta P_2(cos\theta)}{4\pi}$$

θ is the angle between E and V; β is the anisotropy parameter, and P_2 is the second order Lengendre Polynomial:

$$P_2(cos\theta) = \frac{1}{2}(3cos^2\theta - 1)$$

β has limiting values of +2 for a parallel transition and -1 for a perpendicular transition, Fig. 2.3 describes the angular distribution (in two dimensions) of fragments undergoing parallel and perpendicular transitions. In the case of parallel transitions (β=+2) the photofragment distribution follows a $\cos^2\theta$ distribution. Most fragments recoil with $\theta = 0^o$ and no fragments recoil with

θ = 90°. A similar relationship holds for perpendicular (β = -1) transitions except that they follow a $\sin^2\theta$ rather than $\cos^2\theta$ distribution.

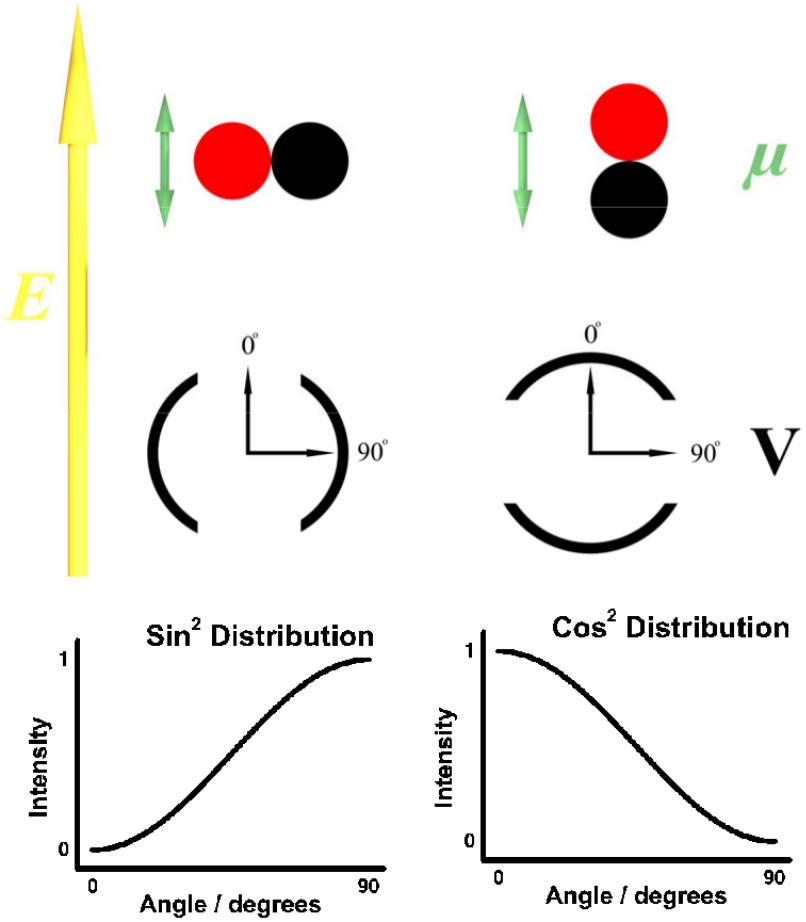

Figure 2.3: Description of perpendicular (left) and parallel (right) transitions and the angular distributions of the photofragments which result. In a perpendicular transition, μ is aligned perpendicular to the bond which is broken and therefore the fragment velocities (V) follow a $\sin^2\theta$ distribution with respect to E, i.e. the maximum intensity is observed at 90° to E. In a parallel transition, μ is aligned parallel to the bond and so the fragment velocities follow a $\cos^2\theta$ distribution with respect to E. By experimentally determining the correlation between E and V the E-μ correlation can be derived.

Photoproducts having angular distributions indicative of purely parallel or perpendicular transitions, i.e. following a purely $\cos^2\theta$ or $\sin^2\theta$ angular distribution and thus having $\beta = 2$ or -1, respectively, are extreme cases. In reality, β parameters are usually somewhere between these limits. One possibility is a value of $\beta = 0$, which corresponds to an isotropic angular distribution. This can

occur if the lifetime of the excited state produced is longer than the rotational period of the molecule. I.e. In the time between excitation and dissociation, the group of excited parent molecules have their alignments randomised by rotations in all directions. As a result, a measurement of the β parameter not only yields information on the symmetry of the two states involved in the transition, it also provides insight into the timescale of the dissociation.

2.2.4 The Newton Sphere

Experiments rarely involve dissociating one molecule at a time. Rather, they involve a very large number of molecules randomly aligned in three dimensions interacting with a large number of polarised photons. In practice, crossing a molecular beam with a laser beam results in an expanding "cloud" of fragments in three dimensions, known as a Newton Sphere (NS). In theory, only a thin two dimensional slice through the centre of the sphere of photofragments is required, as it would contain all the information necessary to elucidate the dynamics of the dissociation. In practice, experiments produce the full three dimensional NS, and various methods are employed to selectively detect only the centre slice (see section 2.6).

2.3 The Evolution of VMI

Photodissociation experiments aim to answer a number of questions: What are the reaction products?; What are the internal and kinetic energies of these products?; What is the angular distribution of these products with respect to the polarisation of the photons? The answers to these questions provide a great deal of insight into the dynamics of the photodissociation process, and much effort has therefore been expended to develop experimental techniques which can provide this information.

Over time, different techniques have been developed which answer more and more of these questions, from early mass spectrometry (MS) studies (used to determine the identity of the products) to modern imaging techniques (which can potentially answer all of the above questions within a single experiment). VMI is the latest in this line. It has been widely reviewed in the literature; the salient points regarding how it works and a brief description of the information which can be obtained from it is provided in this chapter.[14,21–25]

2.3.1 Identifying Products

When a chemical reaction occurs the first question is: "What are the products"? One way to answer this is to use mass spectrometry (MS), the development of which won Aston the Nobel Prize in 1922.[26] Aston, carrying on from the work by Thompson, built the first "mass spectrograph," used for separation and detection of isotopes. Mass spectrometry has since been widely applied in reaction dynamics. With conventional MS, the products of a chemical reaction undergo electron-impact ionisation and are then separated (by a magnetic field) based on their mass:charge ratio. This allows the detection of the masses of all fragments present, and hence determination of the identity of all product species, which in turn provides insight into the mechanisms by which the reaction takes place. One problem with standard MS is that

the electrostatic fields must be varied to detect different masses, and it can therefore take a long time to scan through the entire distribution of product masses. As a result, the reaction conditions may change over the course of the scan, meaning the ratios of the peaks cannot always be accurately compared or quantitatively analysed.

Time Of Flight mass spectrometry (TOF-MS) was developed in the late 1940s and allows the determination of all product masses simultaneously. TOF-MS, like standard MS, involves ionising the products, but then electrostatic fields are used to deflect all of the ions along a field free "drift" region (the TOF tube) to the detector, and from their arrival time their masses can be calculated. The fields result in all fragments having the same kinetic energy. Hence, fragments of higher mass travel more slowly along the TOF tube, arriving later. In this way, by detecting the arrival of fragments as a function of time, and averaging this over a number of reaction cycles, any change in reaction conditions (provided it affects all the products in the same way) will be averaged out, and relative intensities can be accurately determined.

The electrostatic fields in early TOF experiments were provided by two electrodes. The first electrode, the "repeller", was held at a positive voltage, the second electrode, the "ground", was ground (held at 0 V). Products were ionised in the region between the electrodes, and the ions were then repelled from the first electrode, through a hole in the second (which was covered by a grid to keep the fields homogenous and to keep the drift region field-free) into the drift region and toward the detector. The first apparatus was named the "ion velocitron".[7] Early TOF-MS was limited to studying fragments with low mass; initially only fragments with masses below 20 amu could be reliably detected.[6]

This upper limit for mass detection was increased to 75 amu by the use of multiple fields.[9] A third electrode, the "extractor", was added between the repeller electrode and ground electrode and was kept at a lower voltage

than the repeller. This provided two separate and homogenous fields, and the ratio between them could be tuned by varying the potential on the extractor electrode, thereby improving the resolution. By far the greatest improvement in TOF-MS was the development of the Wiley McLaren spectrometer, which involved holding the repeller and extractor electrodes at the same voltage before pulsing the voltage of the repeller electrode to a higher value in order to accelerate the ions to the detector.[8] This modification provided detection of masses up to 300 amu.

2.3.2 Determining Internal and Kinetic Energies

Having developed a technique to determine the identity of the products, the next goal was to investigate the internal and kinetic energy of these products. Advances in the ability to resolve various internal states of molecules is a result of the progress in laser science. In conventional MS and TOF-MS, the products are ionised via electron impact. This is useful in that all non-charged products (neutrals and radicals) are ionised and thus detected, but it has several drawbacks. The ions produced may fragment before detection and, more importantly, resolution of internal states is impossible. A narrow-bandwidth laser allows the detection of a single species in one quantum state only. This means that different states of the products can be probed separately. These quantum state specific results are essential for accurate comparison to theoretical models and represent one of the huge benefits laser technology has provided to chemistry.[27]

Kinetic energy resolution was achieved with Photochemical Recoil Spectroscopy (PRS), which involves photodissociating a molecule under field free conditions, and measuring the time the fragments (the small solid angle of the expanding Newton Sphere which happened to be travelling towards the detector) take to reach the detector (a standard mass spectrometer).[28] The standard mass spectrometer was soon replaced with a TOF spectrometer and this

version of the technique, dubbed Photo-Fragment Translational Spectroscopy (PFTS), is still in use today.[29,30] The other main technique for determining the fragments' kinetic energy is analysis of the Doppler lineshapes following product fluorescence, which is improved by the use of standard high-resolution lasers. The fluorescence may be spontaneous or induced, e.g. Laser Induced Fluorescence (LIF). This is limited to light molecules (with a large Doppler shift) and also has the drawback that very different processes can give similar lineshapes and so analysis is not always straightforward.

2.3.3 Angular Distributions

The final goal in photodissociation dynamics studies was to determine the angular distribution of the photofragments immediately after dissociation. The previously described techniques detected either the entire Newton Sphere (NS) without any discernment of the distribution of product fragments within it (as with MS and TOF-MS), or else detected a small proportion of the NS: those fragments which happened to be naturally travelling towards the detector (as with PRS and PFTS).

The angular distribution can be measured using PFTS provided that either the detector or the polarisation of the photolysis laser can be rotated. By rotating the detector or the polarisation of the photolysis laser, and measuring the signal intensity as a function of the angle, the angular distribution can be determined.[28,31,32] Measuring angular distributions in this manner is rather slow, requiring many averages at each angle, is experimentally difficult, and it can be challenging to detect very light species such as hydrogen atoms. One elegant solution to the latter problem is the "Rydberg Tagging" TOF method, in which H atom products are not ionised, but are excited to a Rydberg state.[33] The neutral hydrogen NS then continues along its initial trajectory without being perturbed by fields, and the H atoms then undergo field ionisation just before colliding with the detector. This technique offers very high resolution

but requires the species of interest, once excited, to have a relatively long lifetime. To date it has mainly been applied to only H and O products, but with great success.

In the more general case, one ideally wants to determine the entire angular distribution of photofragments for each reaction cycle, rather than having to run multiple cycles to successively detect different solid angles of the NS. This goal was realised in 1987 with the Photo-Fragment Imaging (PFI) (or "Ion Imaging") technique reported by Chandler and Houston.[34] The benefits of PFI over PFTS are similar to those of TOF-MS over conventional MS, i.e. the fragments travelling in all directions are detected at the same time, and therefore any variation in experimental conditions during the experiment will not bias the results (as long as it affects all fragments in the same way).

Velocity map imaging (VMI) was derived from PFI ten years later by the fortuitous discovery of several subtle but powerful amendments which vastly increased the resolution of the image produced. As a result, VMI is now a widely used technique, employed in laboratories all over the world.[22,24,35–38]

2.4 Photofragment Imaging

2.4.1 The Development of PFI

After inducing a dissociation via absorption of a photon, a NS of expanding photofragments is produced, from which the kinetic energy and angular distribution of the fragments must be determined. This was usually achieved by dissociating the molecules in field-free conditions, and then varying the angle of the photon polarisation and measuring the intensity of the solid angle of fragments detected as a function of the angle between the photon's electric field polarisation and the detector. A much more elegant method was created in 1987 when Chandler and Houston reported their PFI technique.[34] They used an MCP with a phosphor screen coupled to it, which provided position sensitive detection (see section 3.6.1 for more information). This type of detector had previously been used in other fields, for example to study the velocity distributions of Rh atoms desorbed from an Rh surface by ion bombardment.[39] By combining this detection system with TOF-MS, the anisotropy of the fragments' velocities, and their maximum kinetic energy, could be determined in a single experiment.

In PFI, a molecular beam is directed along the TOF axis. It passes through small grid-covered holes in the centres of the electrodes. The target molecules in the beam are dissociated (and, in the case of neutral products, are ionised) between the repeller and extractor electrodes. As the (now ionic) NS is expanding, standard TOF-MS electrodes are used to repel the entire NS down the TOF tube towards the detector. When an atomic (or molecular) fragment ion, photon or electron collides with the detector, the detector fluoresces at the point where the collision occurred, i.e. if ions only arrive at the centre, one would see a bright spot there, if they arrive only at the top, one would see a bright spot there etc.

As a result, when the entire NS is detected (the NS is said to be "pan-

caked" onto the detector) an image is produced which is the two dimensional projection of the entire three dimensional sphere. Fig. 2.4 shows the NS and the two dimensional pancaked image which it produces.

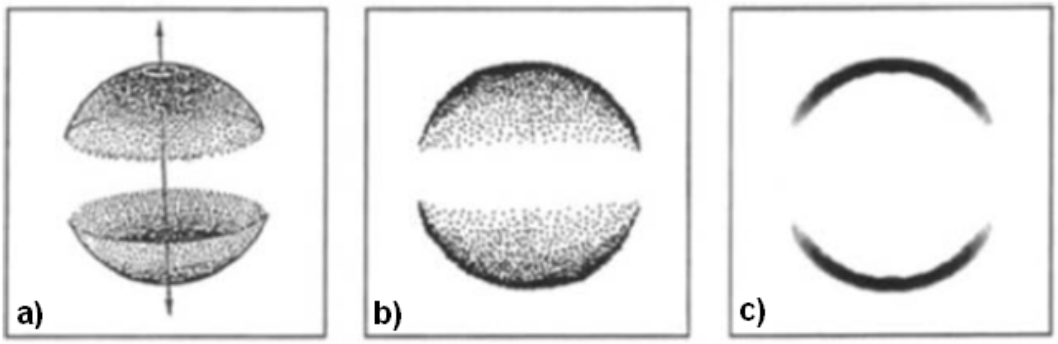

Figure 2.4: (a) Artist's impression of an expanding NS (laser polarisation defined by the arrows). (b) The image produced by the entire NS being pancaked onto a detector. (c) A hypothetical image which shows just the centre two dimensional slice of the NS.[14]

2.4.2 The PFI Image and its Problems

The PFI technique was widely adopted for photodissociation studies soon after its introduction.[40,41] Fig. 2.5 shows the first image produced by PFI, clearly showing the anisotropy of the fragments' recoil. This represented a huge step forward in reaction dynamics: the angular distribution could be immediately determined, at least qualitatively, if the orientation of the electric field vector of the dissociating photons was known. Determining kinetic energy from an image is conceptually straightforward. All the fragments are produced in a fairly well defined area (the intersection region of the laser and molecular beam). This is taken to be the centre of the image. As a result, the radius to the outside of the image is proportional to the distance the fastest fragments have travelled between dissociation and detection, which in turn is proportional to the products' maximum kinetic energy.

There are two main problems with the images produced via the PFI technique. The first is that (as previously mentioned) the entire NS is imaged when

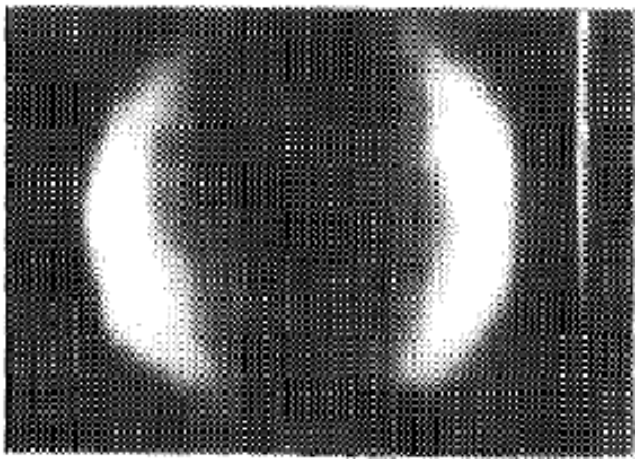

Figure 2.5: The first image produced by the PFI technique.[34] The image is of methyl fragments detected after dissociation of methyl iodide. It clearly shows the parallel nature of the transition producing the dissociation (E is aligned horizontally).

only the centre slice is needed. This is a problem because imaging the entire NS can obscure information. If multiple reaction channels operate, then the result is a set of concentric NSs produced by fragments with different kinetic energies. By imaging the entire NS, information about the slower fragments can potentially be obscured. Fig. 2.6 shows an image of NO fragments from NO_2 dissociation at $\sim$226 nm with just the centre slice detected. The two bright rings correspond to NO fragments from different product channels. If the entire NS was imaged, the two rings would blur together, thereby reducing the information which can be obtained from the image. Furthermore, when analysing a full NS image, only the maximum kinetic energy can be determined as the resolution in insufficient to discern any fine detail. Solutions to this problem are covered in section 2.6. The second problem with PFI is its low resolution.

2.4.3 Poor Resolution in PFI

The image in Fig. 2.5 is quite crude; several factors may contribute to this. One is space charge effects: product fragments must be ionised for detection,

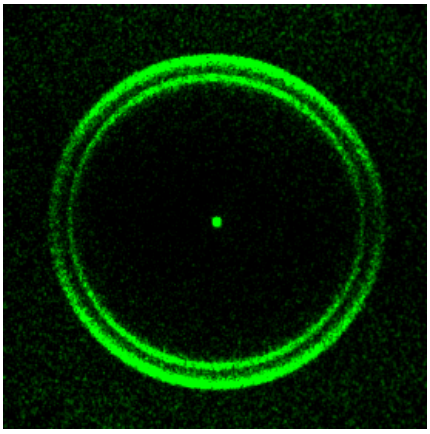

Figure 2.6: Sliced VMI image of the NO fragments from NO_2 dissociation at ∼225 nm, showing rings with similar radii, the discernment of which could be lost if the entire NS is imaged.

and a large number of like-charged particles will repel each other, resulting in a blurred image. For an extreme case, in which the kinetic energy of fragments is low, the result of space charging may be an image which shows the magnitude of Coloumb repulsion between ions overlaid on top of the kinetic energy distributions. As a result, to detect accurate and well-resolved kinetic energies it is essential to minimise the space charge effects. This involves reducing either the partial pressure of the reactant gas within the molecular beam and/or the laser intensity.

In addition, resolution and hence image quality is reduced by both trajectory perturbations due to the grids (the grid lines can clearly be seen superimposed on the PFI methyl image above), and by uncertainty in the birth place of the fragments. I.e. The volume of space in which fragments are produced results in an inherent uncertainty in the initial position of any one fragment, and this uncertainty will be magnified at the detector.

To obtain the highest quality image it is necessary for the dissociation to occur in the smallest possible volume. This can be accomplished, to some degree, by tight focussing of the laser and molecular beams, however this does not fully negate the problem and can be difficult to achieve. Additionally, the grids located in the centre of the electrodes (for the purpose of ensuring

homogeneity of the electrostatic fields) perturb the trajectory of the fragments and reduce the number of ions arriving at the detector.

2.5 Velocity Map Imaging

The volume in which fragments are "born" has a direct effect on the quality of the image. The larger this volume, the greater the spread of arrival positions of equivalent particles and the more blurred the image. In their paper Chandler and Houston commented:

> "*Presently, the main limitation to the spatial resolution of the projection is due to the fact that the molecular beam width is significant on the scale of the image.*"

In 1997 Eppink and Parker refined the PFI technique in two ways.[42] Firstly, they removed the grids in the centre of the electrodes which resulted in the repeller and extractor field regions interpenetrating and essentially functioning as an electrostatic lens. This resulted in a drastic improvement in image quality. Secondly, they varied the potential on the extractor electrode. By tuning the ratio of the repeller and extractor voltages they were able to produce optimum "velocity mapping" conditions. Under these conditions the arrival point of fragments at the detector is a function only of their initial velocity (recoil speed and angle with respect to E), and is independent of their spatial origin. This has the added advantage that larger starting volumes may be used, resulting in lower fragment densities and thus a decrease in space charge effects.

The most obvious way to show that VMI excels PFI in terms of image quality is of course to compare images obtained by each technique. In their initial VMI paper, Eppink and Parker compared images of oxygen fragments from the photodissociation of O_2 obtained with both PFI and VMI. These are shown in Fig. 2.7; the improvement in resolution is obvious.

To increase resolution even further, some groups have amended the standard VMI apparatus. These amendments include the addition of hexapoles to

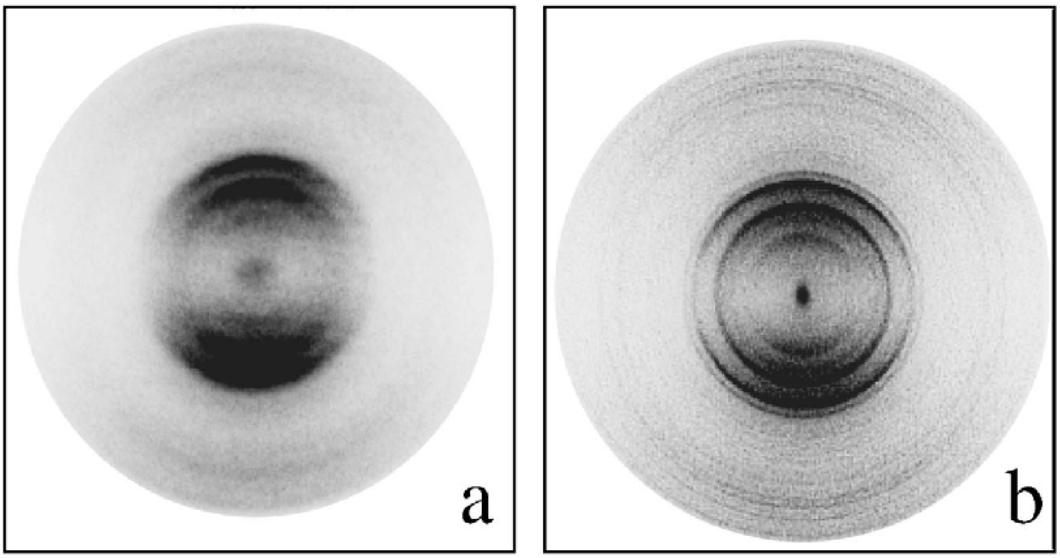

Figure 2.7: Images of oxygen atoms from the dissociation of O_2 produced using a) PFI and b) VMI. The images are of the centre slice of the NS only, and many different concentric rings are visible, each corresponding to a different reaction pathway.[42]

focus the molecular beam and provide state selected reactants, using modified electrodes to align the parent molecules prior to photolysis and the addition of a reflectron to extend the effective TOF region (a technique which had previously been used to improve mass resolution in standard TOF-MS).[43–47]

The above discussion illustrates the purpose of VMI, which is to ensure that fragments with the same kinetic energy arrive at the same position on the detector, regardless of where they were produced. This results in a drastic improvement in resolution and hence the ability to quantify results much more accurately.

2.6 The NS Centre Slice

An image of only the central slice of a NS of photofragments would contain all the information which can be obtained from an imaging experiment, with high resolution (due to VMI focussing conditions) and without anything being obscured by imaging the entire NS. The attainment of an image of the central slice has been the subject of much investigation. In practice, one of two methods is used: mathematical (Abel inversion or forward convolution) or experimental (slicing).

2.6.1 Obtaining the Centre Slice Mathematically

The raw image itself is of little use quantitatively until the centre slice can be obtained from it. The necessity for reconstructing three dimensional images from two dimensional projections was already a widely researched topic in many other fields. In 1968 such reconstructions were used to create a three dimensional density map of the tail of a bacteriophage from electron microscope images and, in engineering, reconstructions were essential for analysing plasmas and flames from jet engines.[48,49] The most widely used reconstruction technique at the advent of PFI was the inverse Abel transform, or some variation thereof, which involves applying a Fourier Transform to the raw image, followed by an inverse Hankel transform.[50–52]

The inverse Abel transform mathematically reconstructs the central two dimensional slice of the NS from the two dimensional projection of the entire three dimensional NS. The oxygen images in Fig. 2.7 were reconstructed from the pancaked NS in this way. Reconstruction techniques are subject to two flaws: they require cylindrical symmetry and the reconstruction adds noise to the image.[53] For cases in which the image does not possess cylindrical symmetry (e.g. in scattering or collisional dynamics experiments) forward convolution techniques can be used, which attempt to recreate the image based

on input parameters about the reaction, however the accuracy of the fit can only be determined by eye.[54]

Despite the problems with mathematical techniques, they are widely used and several variations are now prevalent, including the BASEX and Onion-Peeling techniques.[55,56] An alternative to computational methods known as "slicing", which aims to isolate the central portion of the NS experimentally, has also been widely adopted.

2.6.2 Obtaining the Centre Slice Experimentally - Slicing

Optical and Doppler slicing techniques use the ionisation laser to carry out the "slicing". In "normal" imaging, the dissociation produces a NS, and then the entire NS is ionised and therefore detected, necessitating the reconstruction methods outlined above. It is not possible to produce a two dimensional NS of photofragments, so the experimental strategy is to produce the three dimensional NS, and then selectively detect only the central slice.

In VMI, after photodissociation, the NS is expanding in three dimensions and so when a narrow bandwidth laser is used to ionise the NS, the Doppler effect becomes important. If the laser is tuned to the centre of the Doppler profile for the ionisation, only those fragments flying with no velocity component in the direction of propagation of the laser will be ionised. In order to ionise those fragments travelling towards or away from the laser beam, the laser must be scanned over the wavelength range constituting the transition's Doppler profile. The earliest attempt to experimentally isolate the central slice of the NS was reported in 1991 when Kinugawa and Arikawa took advantage of the Doppler effect and combined it with PFI to create the "Doppler-imaging" technique.[57] While this technique is elegant, it requires that the detector be offset from the TOF axis in order to avoid firing the laser beam directly onto it. Most experiments have the laser beam(s) fired between the repeller and extractor electrodes at 90^0 to the TOF tube. As a result of this common ex-

perimental geometry, a number of other experimental slicing techniques have since been proposed. They can be loosely grouped into two categories: optical and non-optical.

2.6.3 Optical Slicing

Optical slicing involves manipulating the laser beam(s) with a cylindrical lens to form a beam focussed in one dimension (a "sheet" beam) rather than the usual case of a beam focussed in two dimensions by a spherical lens (a "dot" beam).

The earliest optical slicing technique was reported in 1994 by Suzuki and co-workers in which both the dissociation (pump) and ionisation (probe) laser beams were focussed with cylindrical lenses (forming "sheet" beams) in order to selectively ionise only the central slice of the NS.[58] After the advent of VMI much more effort was directed towards developing slicing techniques. The two other common optical techniques are the sheet-dot slicing of Chestakov *et al.* and the dot-dot technique developed by Suits and co-workers.[59,60]

Dot-dot slicing involves using dot beams (focussed with spherical lenses) for dissociation and ionisation. This results in high quality images, but the ionisation laser beam must be swept along the vertical profile of the NS to obtain the full image of the central slice. In sheet-dot slicing, dissociation occurs with a sheet beam and ionisation occurs with a dot beam. The result is that the relatively small ionisation region contains species travelling in all directions because they were born in different positions of the dissociation beam focus. Fig. 2.8 contains diagrams of these three optical slicing methods.

Another variation which could be applied is the more intuitive dot-sheet slicing in which one would dissociate the gas molecules with a dot beam, allow the NS to expand, then ionise using a sheet beam, which results in the central portion of the sphere being preferentially ionised. The goal of optical slicing is to ionise a slice of the NS which is as thin as possible. This is accomplished by

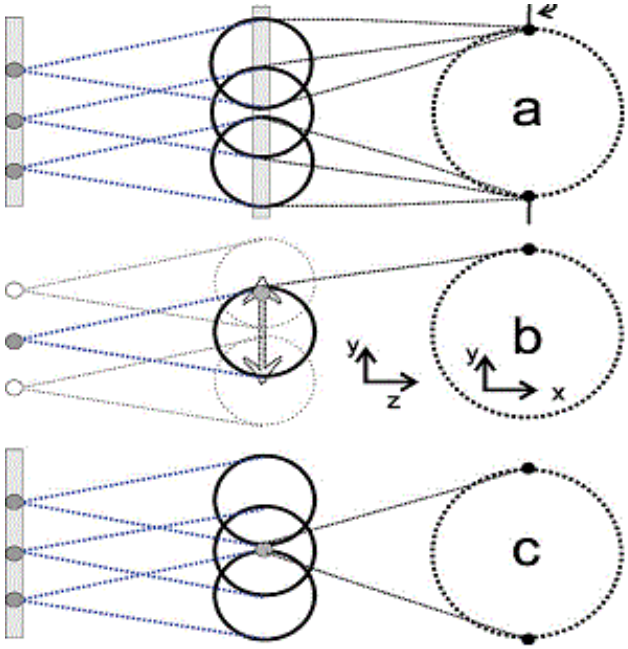

Figure 2.8: Pictorial descriptions of sheet-sheet, dot-dot and sheet-dot slicing.[22]

increasing the time delay between dissociation and ionisation so that the NS is allowed to expand before ionisation, resulting in the thinnest possible slice being ionised. Optical slicing reduces space charge effects (NS are allowed to spread out), but ensuring homogeneity of the sheet beam is a challenge. Several reviews have been published which compare optical slicing methods in more detail.[22,60]

2.6.4 Non-optical slicing

One problem with optical slicing is that it cannot be used in all situations. It only works when there are two separate laser beams, one for dissociation and a second for ionisation. In certain cases (such as the photodissociation of oxygen in the first report of VMI) the same laser beam dissociates the reactant molecules and ionises the product fragments. In other cases the dissociation results in products which are ionic rather than neutral and the fragments are therefore repelled down the TOF tube as soon as they are produced, making optical slicing impossible. Non-optical methods solve this problem by slicing

the NS in a different way.

In TOF-MS experiments the detector is normally biased at the operational voltage at all times in order to detect all masses of fragments. In PFI and VMI the detector remains "turned off" to avoid noise from stray photons and ions other than those being investigated, it is only pulsed on (gated) over the arrival time spread of the NS.

Pulsed-Field Slicing

In non-optical slicing this gating principle is extended. The detector is gated (over as short a time as possible) over just the centre of the NS arrival time, rather than over the arrival of the whole NS. This method had previously been used in PFTS studies.[61] The earliest arriving fragments are not detected, nor are the latest arriving fragments (the "front" and "back" of the NS). The gate ensures that the detector is only functioning when the centre of the NS is arriving. Fig. 2.9 shows this situation. The size of the gate on the MCP (the length of time over which is turned on) determines the thickness of the "slice" which can be detected. The shorter the gate, the thinner the slice and hence the better the quality and resolution of the image. In order to further maximise the effectiveness of this technique, the arrival time spread (δt) of the NS is made as long as possible. There are two methods to accomplish this.

Firstly, the NS itself may be made as large as possible before repelling it with the electrodes, thereby increasing its diameter in the TOF direction and resulting in a large δt. Kitsopoulos and co-workers developed "pulsed-field" slicing based on this principle.[62] Pulsed-field slicing involves dissociating and ionising the reactants between the repeller and extractor electrodes which are held at 0 V. Because the NS of ions is under field-free conditions, it continues to expand unperturbed. After a certain time delay, when the NS has reached a large and diffuse size, the electrodes are pulsed on and the whole NS is repelled down the TOF tube. The large diameter of this NS provides a larger δt than

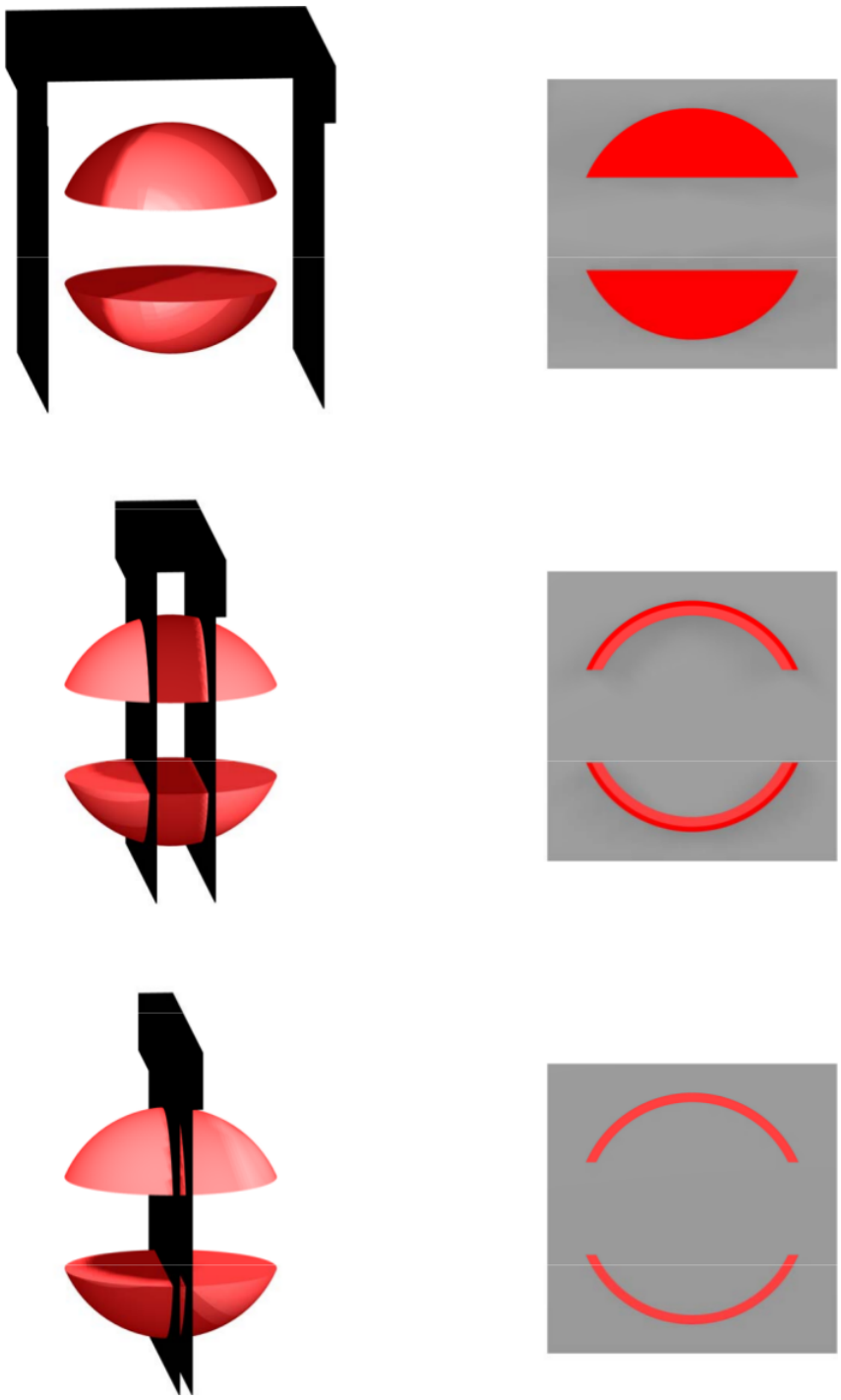

Figure 2.9: A representation of the image produced (right side) by detecting "slices" of varying size from the entire NS (left side).

a small NS, and a thin centre slice is easily cut out by the detector gate.

One problem with pulsed field slicing is that pulsing the electrodes can distort the NS and therefore the image and, additionally, grids are needed in the

electrode holes to ensure homogeneity of the fields, which can cause trajectory perturbations and further distort the image (and therefore while it can be used with PFI, it cannot be used with VMI). A similar approach which can be used in two laser experiments is to maintain the electrodes at positive voltage and just increase the time delay between dissociation and ionisation. This has the same effect as pulsed field slicing, but without distorting the NS. Nevertheless the pulsed-field technique is still used, being the only slicing technique which provides field-free conditions following photodissociation, should these be needed (for reactions which produce ionic products).

dc-Slicing

An alternative non-optical technique termed dc-slicing was devised by Suits and co-workers.[59] This technique makes use of the "turn-around time" (T_{ta}) in order to make the NS as large as possible in the TOF direction. Fragments in the NS travelling forward along the TOF tube after photodissociation are immediately accelerated towards the detector upon ionisation, while those travelling backwards must first be decelerated, resulting in a non-negligible T_{ta} of the NS.

The T_{ta} determines the size of the arrival time spread at the detector: a long T_{ta} results in a large δt. In addition, T_{ta} is only a function of the potential between the repeller and extractor electrodes and is independent of the length of the TOF tube.[59] A high voltage on the electrodes results in a very short T_{ta}, therefore a small NS and hence a small δt.

In order to increase δt, T_{ta} must be made as large as possible. This is achieved by decreasing the voltage on the electrodes. The resulting increase in T_{ta}, and therefore δt, enables a thin slice to be readily cut out of the NS. While dc-slicing is straightforward, there is one significant problem: because the electrodes are at lower voltages the NS takes longer to travel down the TOF tube. This increased flight time has no effect on δt (which depends only

on T_{ta}) but it does mean the photofragments in the NS have more time to expand parallel to the detector. The result is that fragments with high recoil kinetic energy may miss the detector altogether.

Suits and co-workers remedied this problem by adding additional extractor electrodes which served to prevent the NS from expanding parallel to the detector while still allowing low voltages to be used in order to achieve a long δt.

2.6.5 Slicing Considerations

It should be noted that the images produced by slicing are not perfect. The main problem is the imbalance of sensitivity and efficiency between slow and fast fragments. A slice through the centre of concentric NSs will naturally ionise a larger proportion of fragments in small NSs (slow moving products) and a smaller proportion of fragments in large NSs (fast moving products). I.e. Slow moving fragments are detected with higher efficiency. In addition, since slow moving fragments produce NSs with smaller radii, the velocity resolution is lower for small NSs than for large ones. Therefore, before calculating branching ratios from an image, the image must still be deconvoluted. Nonetheless, the images produced after deconvolution or reconstruction are often of higher quality and provide higher resolution and better signal to noise ratios than whole NS pancaked images. Slicing is therefore ubiquitous in, if not synonymous with, imaging techniques.

Chapter 3

Apparatus

3.1 Overview - A Typical VMI Experiment

A typical unimolecular VMI experiment proceeds as follows. A molecular beam is directed along the TOF axis, through a stack of circular electrodes. Molecules pass through the holes in the centre of the electrodes. Between the first and second electrodes the molecules are dissociated to form a Newton Sphere (NS) of expanding fragments. This sphere of photofragments is then ionised. Upon ionisation the fragments are accelerated by the voltages on the electrodes down the TOF tube onto the detector. The fragments' arrival is detected either by the intensity of the current which the fragments produce in the detector as a function of time (a TOF-MS experiment) which is fed to and recorded on an oscilloscope (see Fig. 3.1), or by the production of an image using a detector which is position sensitive (an imaging experiment). The image produced in an imaging experiment is transferred to a PC for analysis. A typical imaging experiment lasts twenty to thirty minutes, producing a final image which is a composite of each image from around 20,000 laser shots.

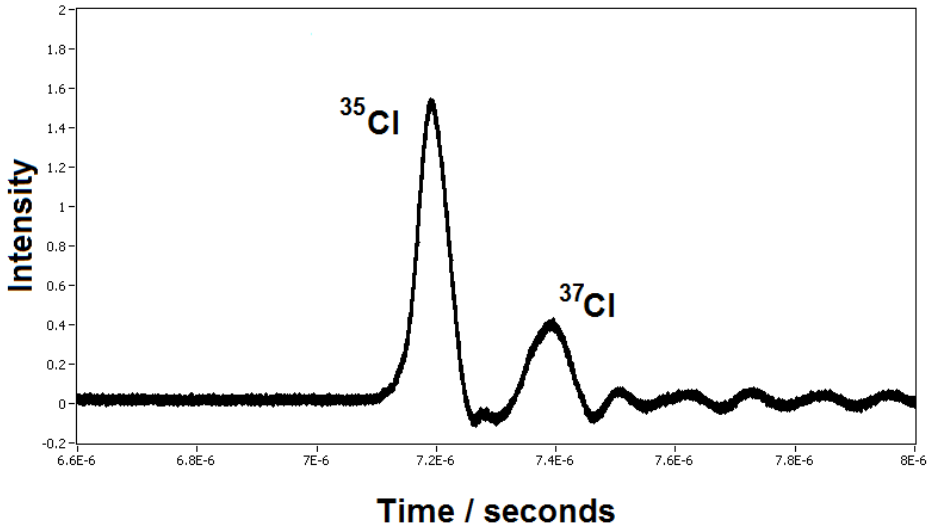

Figure 3.1: A TOF trace of Cl ions from the 351 nm dissociation of Cl_2. The $^{35}Cl^+$ ions arrive before the heavier $^{37}Cl^+$ ions. The relative intensities of the peaks reflect the natural isotope ratios of chlorine. The oscillation of the trace after the arrival of the Cl ions is noise as a result of "ringing", which could not be removed experimentally.

Within the confines of this description, VMI experiments can vary in a number of ways. The molecular beam containing the reactants may use any one of several different inert carriers (He, Ar, N_2). The fragments may be dissociated by a variety of methods, e.g. electrons or photons. In the case of photons, a variety of laser systems may be used, and the dissociation may be a single or multiple photon process. In some cases the fragments produced may be ionic (either positively or negatively charged) meaning the polarity of the voltages applied to the electrodes may be different for different experiments. In some experiments the electrodes remain at ground and are only quickly pulsed to a positive or negative voltage. In the case of neutral fragments different laser systems can be employed for ionisation. Several different types of detector may be used to provide position-sensitivity and to produce images (e.g. delay line anodes, MCPs coupled to phosphor screens etc).

The following description is of the VMI experiments carried out using the

apparatus described here. 2 - 5 % of the reactant molecules are seeded in He and this mixture forms the molecular beam. This beam is directed along the TOF axis through a stack of 12 electrodes which are permanently biased at positive voltages. The photodissociations are all single photon processes and are carried out either with an excimer laser (for two colour experiments) or a YAG-pumped dye laser (for one colour experiments). All the photofragments which are produced are neutral and are ionised using the YAG-pumped dye laser system. Upon ionisation the positive fragments are accelerated by the electrodes and detected using an MCP detector coupled to a phosphor screen to provide position sensitivity. A CCD camera is used to detect the fluorescence. The experiment runs at 20 Hz and is repeated ∼20,000 times in order to produce the final image.

The apparatus consists of six subsystems: vacuum chambers, the molecular beam, the laser systems, the electrodes, the detection system and the control system. The following sections describe each of these systems.

3.2 Vacuum System

3.2.1 The Chamber

Fig. 3.2 shows a diagram of the vacuum chamber, which is ∼1.5 metres in length, and is composed of three sub-chambers. The first houses the molecular beam valve and skimmer (the "molecular beam chamber"). The second, optional, chamber is used to provide enhanced differential pumping (the "buffer" chamber). The third is the "reaction chamber," which contains the electrodes, TOF tube (which gives a ∼0.45 m TOF length between the point of molecular beam/laser intersection and the MCP detector). The TOF tube may be lengthened to 1 m by the insertion of additional chamber sections if required. Fig. 3.3 shows the apparatus as used for the experiments described here, with the shorter (0.45 m) TOF tube and the buffer chamber removed.

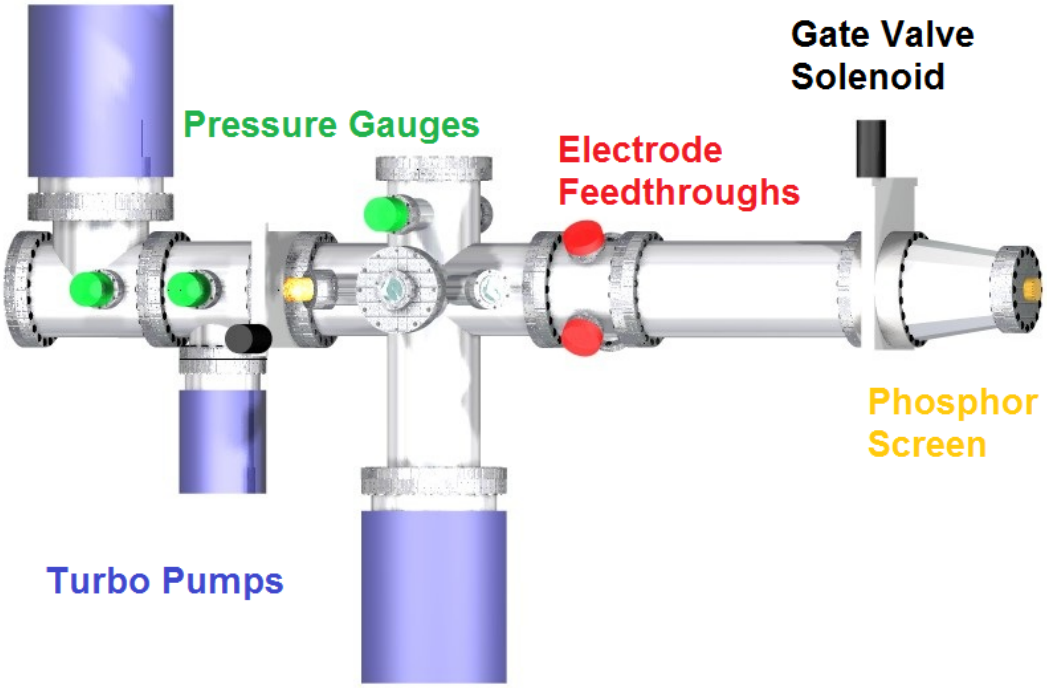

Figure 3.2: The vacuum chambers.

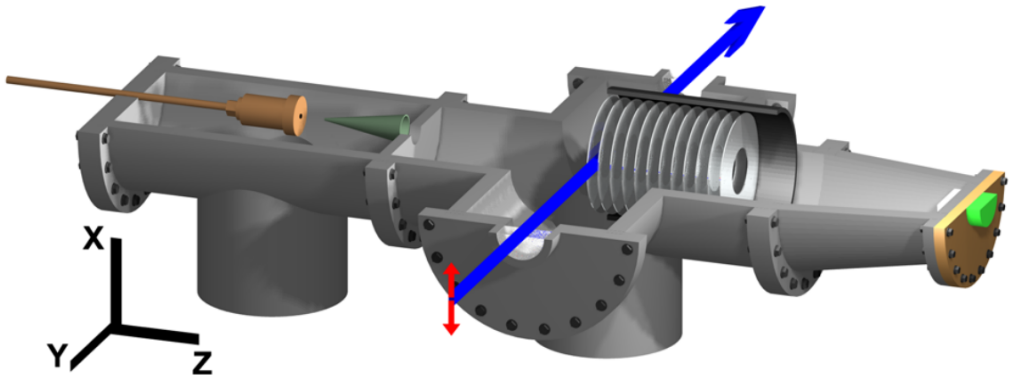

Figure 3.3: A cutaway diagram of the chamber as used for experiments described here. A 0.45 m TOF tube is used, and the buffer chamber is removed.

The vacuum chambers are essentially a stainless steel tube with an inner diameter of ∼18 cm. The molecular beam end of the chamber is closed with an 8″ diameter CF flange containing a 6 mm wide feedthrough for the molecular beam gas line. On either side of this chamber are two 2.75″ CF flanges, one containing an ion gauge, the other with electrical feedthroughs to power the molecular beam valve. The molecular beam and reaction chambers are separated by a ∼1 cm thick plate with a ∼2 cm hole in its centre, onto which the molecular beam and skimmer are mounted.

The reaction chamber consists of three parts: a "cross", a set of feedthroughs and a reducer cone onto which is mounted the detector. The cross consists of six tubes: the 8″ diameter TOF tube, a 6″ diameter tube running horizontally at 90° across the TOF tube, a 2.75″ diameter tube running above and parallel to the 6″ diameter tube, an 8″ diameter tube running vertically through the centre and two 2.75″ diameter tubes running horizontally through the centre at ±45° to the TOF tube.

To the end of the 8″ diameter TOF tube is an 8″ to 6″ reducer cone to which is attached a 6″ CF flange containing the detector. The vertical 8″ diameter tube is closed with an 8″ CF flange at the top and the bottom contains a 10″ CF flange to which is mounted a turbomolecular pump. The 6″ diameter tube

is closed on both ends with 6″ to 2.75″ zero length adapters onto which 2.75″ flanges containing quartz or MgF_2 windows are mounted. The 2.75″ diameter tube running parallel to the 6″ diameter tube is closed at one end and has an ion gauge attached to the other. The two 2.75″ diameter tubes running at 45° through the chamber have 2.75″ quartz windows on each end.

The feedthroughs are mounted on a small section of chamber connected to the cross via an 8″ flange and containing four 2.75″ flanges, two of which are closed. The remaining two flanges contain electrical feedthroughs which provide power to the electrode stack which is mounted inside the cross. Between the feedthroughs and the reducer cone a Lesker 8″ pneumatic gate valve is mounted for the purpose of isolating the MCP detector from the rest of the chamber.

The cross is fixed to the chamber table, while the molecular beam chamber and electrode feedthroughs/detector chamber section are mounted on moveable brackets on a set of rails, allowing them to be unbolted and moved away from the cross for servicing and adjustment purposes.

3.2.2 Vacuum for Gas Phase Studies

It is important in the field of reaction dynamics that gas phase systems be studied in vacuum; in order to determine the energy and angular distribution of products they must be nascent, i.e. they must not undergo a collision with another species between formation and detection as this would alter both their energy and direction of travel. As a result, the mean free path (the distance an atom/molecule can travel before colliding with another), λ, must be as long as possible. λ can be calculated by:[63]

$$\lambda = \frac{kT}{\sqrt{2}\sigma p}$$

σ is the collision cross section of the molecule, here taken to be 0.21 nm^2 for helium. At 298 K and 1×10^{-6} Torr, λ for a helium atom is on the order of 100 m. In order to maintain the interior of the main chamber at pressures below 10^{-6} Torr for gas phase reactions, an evacuation system is used.

3.2.3 Evacuation System

A standard combination of turbomolecular pumps backed up by rotary pumps is used to maintain low pressures within the vacuum chambers. The molecular beam chamber is evacuated by a refurbished Edwards STP-1000C turbomolecular pump and the main chamber is evacuated with an Edwards STP-1003 turbo pump.

Turbomolecular pumps are essential to reach low pressures. They consist of a series of magnetically levitated (to minimise friction and heat) rotary blades rotating at high speeds (35,000 rpm) which can produce pressures as low as 10^{-10} Torr, but they require a backing pump in order to maintain a foreline pressure of $\sim10^{-2}$ Torr or lower.

Two Edwards E2M38 rotary pumps are used for this purpose. In order to avoid the oil which lubricates and seals the rotary pumps flowing up into the chamber, an oil mist filter is present on the inlet ports of these pumps, and each also contains a foreline trap which serves to filter the gas being pumped before it is removed by the building's extraction system.

Both turbo pumps have separate backing rotary pumps. The molecular beam chamber rotary pump is also used to evacuate the gas manifold and gas lines in the lab. At the outlet of each turbomolecular pump is an angle valve (a small gate valve) from KJ Lesker driven by pressurised air, allowing the rotary pumps to be isolated from the turbo pumps when evacuating the gas lines or performing maintenance on the rotary pumps.

In order to monitor the pressure, four pressure gauges are mounted on the apparatus. The molecular beam chamber and reaction chamber are each

monitored by a SRS-NW-F-UHV and an Edwards AIM-X-DN40CF ion gauge (designed for monitoring low pressures) respectively. The forelines of the turbomolecular pumps are monitored by SRS-PG105 Pirani gauges.

3.3 Molecular Beam

A sample of small molecules at standard conditions will typically all be in their ground electronic state and ground vibrational states. The rotational state distribution, however, is generally quite broad, with many rotational states being populated. In addition, the kinetic energy distribution of the molecules will be very broad (with an average speed of $\sim$500 m s^{-1} for N_2) and the molecules travel in all directions. For reaction dynamics experiments, it is desirable that the target molecules are spread over as few quantum states as possible. This is achieved by vastly reducing the temperature of the gas sample, most commonly by using a supersonic expansion, part of which is "siphoned off" to form a molecular beam.[64] As a result of the lower temperatures within the beam, not only are the internal energies of the molecules very well defined, but the kinetic energy distribution is also significantly narrower. Fig. 3.4 shows the rotational state distributions for NO molecules at 300 K and at 10 K (the temperature of the molecular beam here).

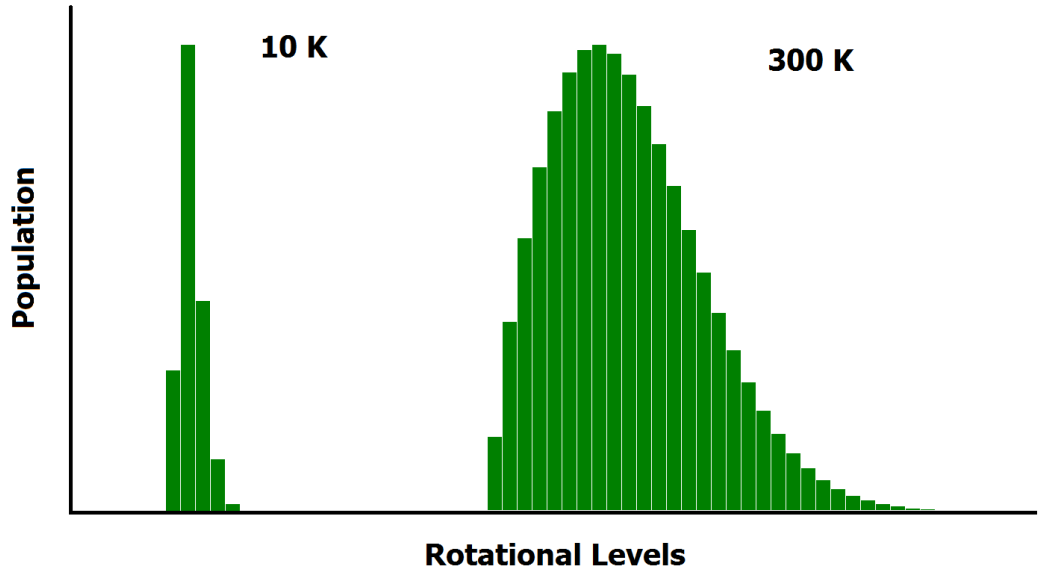

Figure 3.4: The rotational energy distributions of NO molecules at 10 K and 300 K taken from the LIFBASE programme. The leftmost column in each distribution is the ground rotational state. By cooling a sample of gas molecules to low temperatures, the breadth of the rotational state distribution is significantly reduced.

The rotational state distributions of molecules at a given temperature can be determined using the Boltzmann distribution function. For a series of energy levels, E_i (i = 0, 1, 2...), the number of molecules (n_i) in any one energy level, i, can be expressed as:

$$\frac{n_i}{n_0} = \frac{g_i}{g_0} exp(-\frac{E_i - E_0}{k_B T})$$

g_i and g_0 represent the degeneracies of the i^{th} state and the ground state respectively. For a rotational state distribution, the energy of a given rotational level, J, is given by "E_J = BJ(J+1)" and the degeneracy of a given level is "g_J = 2J+1". Therefore, the population of any rotational level at a given

temperature can be calculated using:

$$\frac{n_i}{n_0} = (2J+1)exp(-\frac{BJ(J+1)}{k_BT})$$

The production of a molecular beam involves allowing a gas at high pressure to move through a narrow orifice into a low pressure region. This results in substantial cooling of the internal and kinetic energies of the molecules, and an increase in the average speed of the molecules, all of which now travel in the same direction. Allowing a gas to undergo supersonic expansion converts the internal energies into kinetic energy, and converts the randomly oriented velocities into directed motion. Fig. 3.5 shows the velocity distributions of argon at 300 K (before expansion) and at 10 K (after expansion).[65] The velocity of the argon is much higher and much more well defined in the beam than at standard conditions.

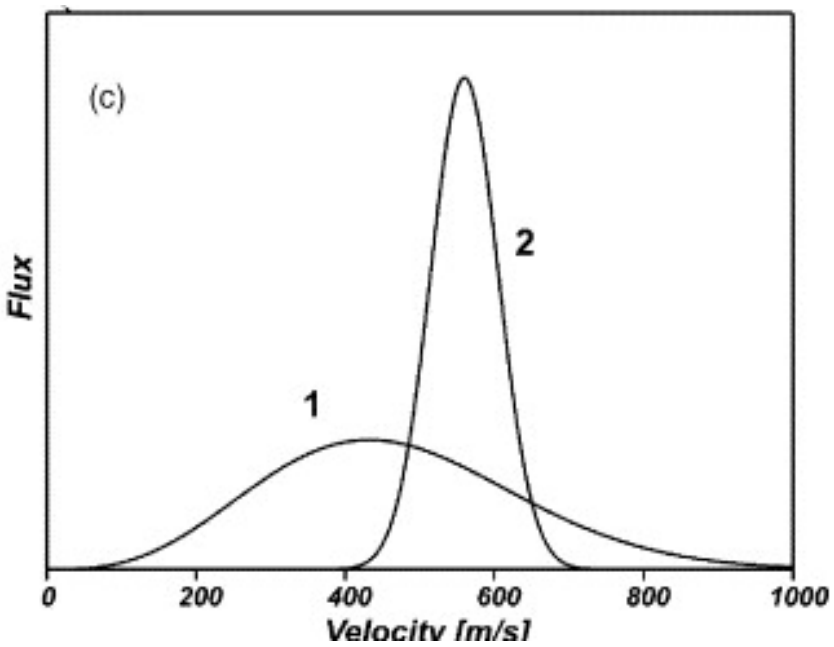

Figure 3.5: Speed distributions of argon gas at 300 K before expansion (1) and at 10 K after a supersonic expansion to form a molecular beam (2).[66]

The velocity distribution of molecules in a sample of gas is dependent on temperature and is given by the Maxwell-Boltzmann distribution, which describes the number of molecules in a gas sample with a given velocity:

$$P(v) = \frac{4}{\sqrt{\pi}\alpha^3} v^2 exp(-\frac{v}{\alpha})^2$$

$$\alpha = \sqrt{\frac{2k_B T}{m}}$$

In a molecular beam, the velocity distribution is described in terms of "flux": the number of molecules with a given velocity travelling through an area per second. The flux is related to the bulk gas distribution above:

$$F(v) = vP(v)$$

$$F(v) \propto v^3 exp(-[\frac{v}{\alpha_s} - S])^2$$

$$\alpha_s = \frac{\alpha}{\sqrt{1 + \frac{\gamma-1}{\gamma} S^2}}$$

S is the speed ratio. For a Maxwell-Boltzmann distribution S = 0. As S increases, the peak velocity of the gas becomes:

$$v_{peak} = \sqrt{\frac{\gamma}{\gamma - 1}} \alpha$$

γ is the ratio of the specific heat capacity at constant pressure to the specific heat capacity at constant volume for the gas in question: $\frac{C_p}{C_v}$. For monatomic, diatomic and polyatomic gases, γ has values of 1.6667, 1.4 and 1.333 respectively.

The translational temperature in the beam can be described by:

$$T_S = \frac{T_0}{1 + \frac{\gamma-1}{\gamma} S^2}$$

T_S and T_0 are the translational temperatures of the beam and source respectively. Higher peak velocities in a molecular beam are thus associated with lower masses (i.e. usually monatomic gases are used to form molecular beams) and higher translation temperatures. The translational temperature is a measure of the width of the distribution, i.e. higher speed ratios are associated with higher beam velocities and thus narrower velocity distributions, i.e. in a molecular beam the molecules undergo substantial translational cooling. Rotational cooling follows a similar pattern, as the speed ratio increases, the rotational temperature within the beam decreases.

Fig. 3.6 shows a schematic of a supersonic expansion. When the gas expands through the hole into the low pressure region, the molecules undergo many collisions with one another. This results in energy transfer between them. As an approximation one can imagine a rotationally excited molecule dropping down to a lower rotational state by transferring the energy to another molecule when they collide. The energy is transferred into kinetic energy of the collision partner. The translationally "excited" molecules produced also collide with one another and exchange energy, which serves to normalise their kinetic energy, resulting in a "cold" kinetic energy distribution. This happens many times while the molecules undergo collisions in the orifice, producing a gas consisting of molecules with high velocity, a narrow velocity distribution, low internal energy and a narrow internal energy distribution. After exiting the collision region, the molecules enter a collision-free zone (the "zone of silence"), in which the internal and kinetic energies are said to be "frozen in". No further collisions and hence no exchange of energy takes place.

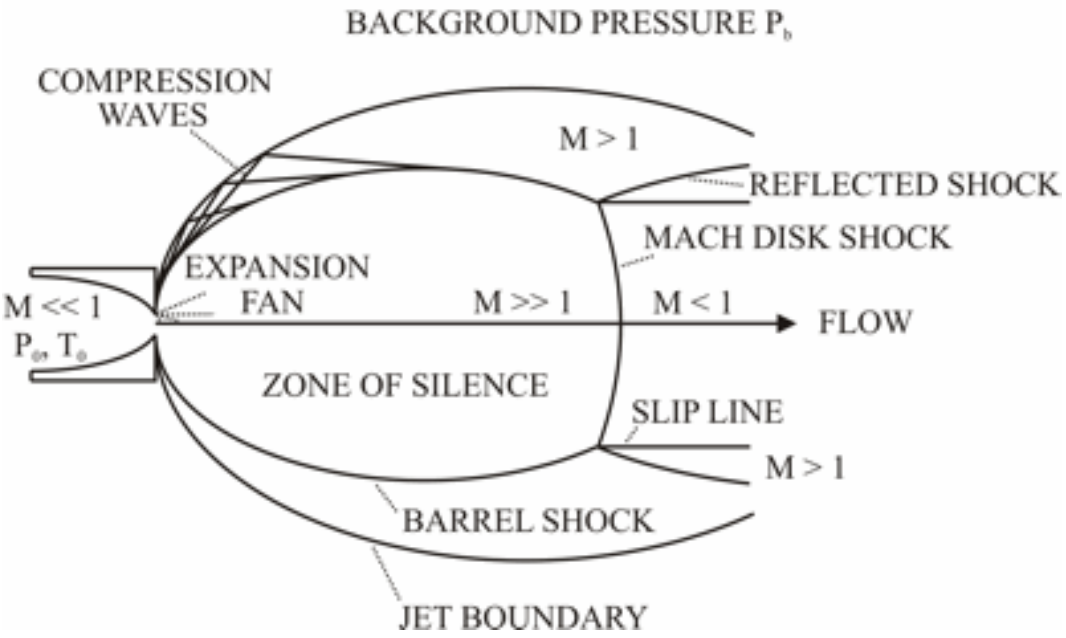

Figure 3.6: A side-view of a supersonic expansion from which a molecular beam can be extracted.[67]

The molecules in a supersonic expansion have their velocities increased well beyond the local speed of sound. Because the molecules are all travelling in the same direction and at supersonic speeds, any disturbance downstream cannot propagate back upstream since the molecules are travelling downstream more quickly than shockwaves from disturbances can travel (at the local speed of sound) back upstream. At the peripheries of the expansion are various shock fronts where the molecules collide and the supersonic expansion is destroyed. In order to make use of the cold molecules they must be separated from the expansion while within the zone of silence, before they reach the shock fronts.

This is achieved by inserting a skimmer (a wafer-thin "cone" of metal) several cm downstream from the orifice. A small solid angle of the expansion is extracted and allowed to continue forward into the chamber. This is the molecular beam, and can be visualised as a cylinder of cold gas molecules

with a small (on the order of mm) diameter and a high density (compared to the surrounding vacuum in the chamber) which travels down the chamber at supersonic speeds.

The gas phase experiments described here all involve the dissociation and ionisation of molecules carried out by intersecting a molecular beam with lasers. A typical gas sample is composed of 2 - 5 % of the target molecule seeded in helium. The mixture is held behind the molecular beam valve (a General Valve with 500 μm diameter orifice) with a stagnation pressure of 1.5 - 2.5 bar. The valve is pulsed using an Iota One pulse driver from Parker, and produces a $\sim$300 μs long gas pulse travelling at $\sim$1000 m s^{-1}. The molecular beam is extracted from the supersonic expansion using a Beam Dynamics skimmer (Model 2, 1.2 mm orifice) placed $\sim$15 mm from the valve's orifice.

Fig. 3.7 shows the apparatus used to produce our molecular beam. The molecular beam valve (1) is mounted onto a brass tube (2) by attaching the tube to the nozzle (3). The brass tube sits within a "birdcage" (4) onto the end of which the skimmer (5) is mounted and held in place by means of a brass cap (6). The distance between the molecular beam nozzle and skimmer can be varied by sliding the brass tube (2) back and forth within the birdcage and then securing it with a set screw. Once assembled, the entire assembly is mounted onto a metal plate which separates the molecular beam and reaction chambers, a hole in which allows the skimmed molecular beam to propagate into the reaction chamber.

Figure 3.7: The molecular beam apparatus. 1 - Molecular beam valve. 2 - Brass tube. 3 - Molecular beam nozzle. 4 - "Birdcage." 5 - Skimmer. 6 - Brass cap.

3.4 Laser Systems

3.4.1 Pump-Probe

A VMI experiment in which two lasers are used (one for dissociation, one for ionisation) is an example of a "pump-probe" technique. Pump-probe experiments originate from flash photolysis, a technique developed by Norrish and Porter in the 1950s and 60s for studying fast unimolecular reactions, for which they won the Nobel prize in 1967 (an early example of the recognition given to reaction dynamics).[5] The technique involves using a short and strong pulse of light from a discharge lamp (located along the side of a tube containing the reactants) to induce photodissociation. A second, broadband lamp filled with a rare gas is flashed at regular intervals in order to record the absorption spectra of the products.

Pump-probe experiments today are conceptually similar to earlier techniques. The main differences are that, rather than being conducted on a sample of equilibrated gas, they are coupled with molecular beams, and instead of lamps they make use of laser technology. The result is the photodissociation of rovibronically cold molecules induced by a pump laser, and then the detection of products in a specific quantum state via fluorescence or ionisation techniques. In addition, because lasers with very short pulse times are now readily available, pump-probe techniques can be applied to the fastest processes in

chemical reaction dynamics.

There are two possibilities regarding the use of lasers in a VMI experiment: one laser system can be used for the dissociation and another for the ionisation. These "two colour" experiments (in which two different wavelengths and hence lasers are used) provide the possibility to use optical slicing techniques. In the case of surface studies two colour experiments are essential. The kinetic energy of the fragments can be measured by studying the signal intensity as a function of the time delay between dissociation and ionisation (a modern pump-probe technique) across the known distance between the two lasers. By measuring both the distance between the beams and the time at which maximum intensity is observed (i.e. the time it takes the fragments to travel from one laser beam to the other) fragment velocities can be determined. Alternatively, the same laser can be used for both dissociation and ionisation. Whether one or two lasers are used largely depends on whether both processes can be induced with photons of the same wavelength. In the case of NO_2 dissociation at 225 nm (see section 5.3), a single laser is sufficient.

3.4.2 REMPI

There are various ways to ionise an atom or molecule, see Fig. 3.8. A single UV photon of high enough energy can be used. This is fraught with problems, however. Firstly, the ionisation of most species would require a single photon of very low wavelength (e.g. 71 nm for a fluorine atom). Producing such photons is not possible with standard laser systems. They can be produced using other methods, but the path of the photons between the source and the chamber must be purged or evacuated since the atmosphere strongly absorbs light of these wavelengths. Finding materials to use for windows also becomes problematic (and expensive). LiF and MgF_2 are among the best available materials for use in the low UV region, but even then are only transparent down to around 120 nm. Additionally, such high energy photons are liable to

ionise every molecule and atom present (reactants and products alike), so all selectivity is lost.

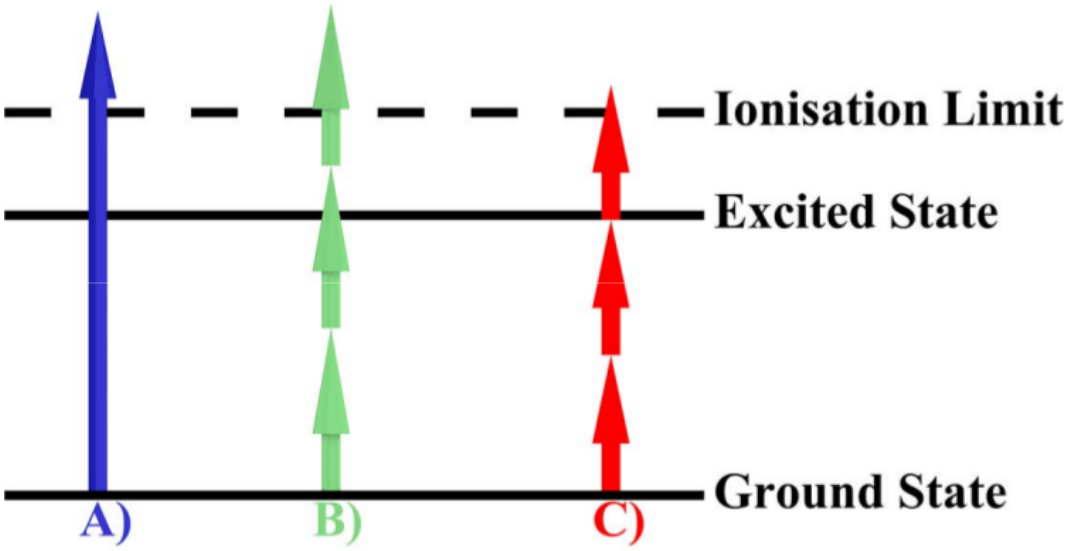

Figure 3.8: Simple depiction of various ionisation schemes. A) One photon ionisation. B) Multi photon ionisation. C) (One colour) 2+1 REMPI.

An alternative is to use multi-photon ionisation (MPI). By increasing the photon densities sufficiently, two photons may be incident on an atom/molecule at the same time. The effect is that the molecule "sees" a single photon whose energy is equal to the sum of the energies of the two photons. This allows a species to be ionised using longer wavelength photons which solves the problems around "normal" ionisation. However, one problem remains. MPI will ionise all products and reactants; it is neither product-specific nor state-selective.

This problem is solved by making use of resonance enhanced multi photon ionisation (REMPI).[68] The probability of a normal MPI occurring can be increased by using a two-step ionisation via an excited intermediate state. The first step involves either a single photon (or multiple photons) promoting the atom/molecule to an excited intermediate state (often a low-lying Rydberg state). A final photon ionises the species from this excited state.

Various REMPI schemes are available and are described by the number of photons involved in the first and second step e.g. 2+1 REMPI (two photons promote the species to the excited intermediate state, then one more photon ionises it). Additionally, different wavelengths can be used for each stage (two colour REMPI) yielding schemes such as 1+1′, 2+1′, 2+2′ etc. REMPI is most commonly performed with a YAG pumped dye laser system due to its narrow bandwidth (the photons produced are all of a well-defined energy, typically with an energy bandwidth between 0.05 and 0.1 cm^{-1}) and its wide wavelength range.

REMPI possesses the added advantage that it can selectively ionise atoms or molecules of a single species which are in a single rovibronic energy level. A photodissociation can produce photofragments with different internal energies, i.e. a number of fragment species may be produced over a range of vibrational or rotational energy levels. Since product fragments produced in different quantum states are produced via different reaction pathways, it is desirable to detect all of these different states and, ideally, the ratios of products within them.

By using a YAG-pumped dye laser system, the bandwidth of the photons is significantly lower than the energy spacings between successive rovibronic levels in small molecules. As a result, the presence of products in different quantum states can be detected, the ratios of products in different states can be quantified and the kinetic energies and angular distributions of each state can also be characterised.

3.4.3 Lasers

Lasers emit light that is coherent (all photons in phase), collimated (all photons propagating in the same direction) and of a narrow bandwidth (a well-defined wavelength).[69,70] The light emitted by lasers originates from transitions between energy levels within the molecules which constitute the "active

medium" in the laser. Energy is pumped into the active medium either through an electronic discharge or optically (with a flash lamp or another laser). This promotes the active medium molecules to an excited state. When they decay back to the ground state, the transitions are accompanied by emission of photons.

In order to ensure the photons produced are amplified, rather than absorbed by the active medium, a population inversion must be created and maintained between the two states (i.e. the upper state must have a higher population than the lower state). In practice, a simple two level system generally does not work: pumping energy into the active medium promotes molecules to the upper state until the populations of both states are equal, known as saturation, and photon absorption and emission then occur at the same rate, i.e. there is no net output of radiation.

A three or four level system must therefore be used, however this results in lower efficiency (ranging from 0.1% for a nitrogen laser to 30% for a diode laser) and also means that the photons being emitted are of lower energy (longer wavelength) than those which were pumped into the system (in the case of optical pumping). The population inversion is maintained for a three level system by rapid depopulation of the lower state by the pumping mechanism. For a four level system, the lower state is depopulated by fast decay to the ground state (followed by pumping to the highest state of the system) and the upper state is kept populated via fast decay from this highest state, shown in Fig. 3.9. Excimer lasers maintain a population inversion in a different way (see below).

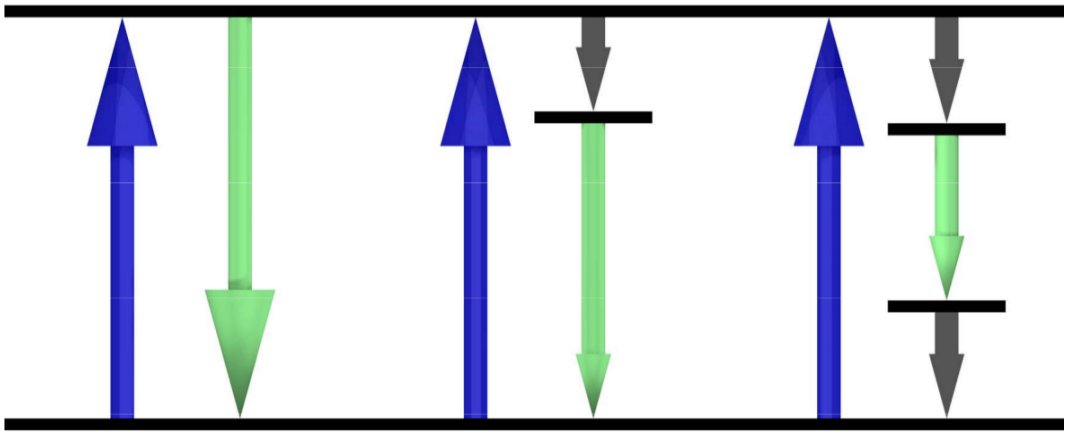

Figure 3.9: Two (left), three (centre) and four (right) level laser systems. Energy is pumped in (blue arrow) and the lasing output (green arrow) can be of the same energy (theoretically) in a two level system, or of a lower energy in a three or four level system, which are necessary to maintain a population inversion.

3.4.4 The Pump Laser

This dissociation of the target molecules is here induced by a standard YAG pumped dye laser system (described below) for one colour experiments and by a Questek Series 2400 excimer laser for two colour experiments. Two level systems cannot maintain a population inversion, however, excimer lasers are the exception to this rule. An excimer is a dimer which is only stable in an electronically excited state, and which dissociates upon relaxation to its ground state. They are produced by mixing a halogen with a rare gas in an inert buffer gas and exciting the mixture using a high voltage discharge. The excited excimers typically persist for several nanoseconds, after which they decay to the dissociative ground state and emit the energy as photons. As there is no stable ground state, excimers intrinsically possess a constant population inversion.

Excimer lasers offer some limited selectivity of wavelength via choice of the excimer complex; wavelengths of 193 nm (ArF), 222 nm (KrCl), 248 nm (KrF), 308 nm (XeCl) and 351 nm (XeF) can be produced. The light emitted by the excimer laser is not polarised, but polarised light can be obtained from an excimer beam.

When a photon strikes a reflective surface, the limiting cases for the alignment of its electric field vector with respect to the surface can be described as either S or P polarised. S polarised light has its electric field vector aligned perpendicular to the normal of the reflective surface and P polarised light has its electric field vector aligned parallel to the surface normal. At a certain angle of incidence, the Brewster angle, the reflection coefficient for P polarised light goes to 0. As a result, when unpolarised light is incident on a reflective surface at the Brewster angle, θ_B, only light which is polarised perpendicularly to the surface normal (S polarised light) is reflected. The Brewster angle depends on the media in which the waves propagate and is defined as:

$$\theta_B = \arctan(\frac{n_2}{n_1})$$

n_1 and n_2 are the refractive indices for the medium in which the photons propagate and the reflective medium respectively. For UV light travelling in air ($n_1 \approx 1$) and reflecting off glass ($n_2 \approx 1.6$) the Brewster angle is $\sim 58^o$. Thus, by reflecting the excimer's output from a glass window aligned at $\sim 58^o$ to the beam, vertically polarised light may be produced. After polarisation, the energy of the excimer beam (at 193 nm) is $\sim$1 mJ. By altering the number and orientations of mirrors, one can select whether the reflected S-polarised light is aligned horizontally or vertically (in the lab frame) as desired. The polarised light is directed through the reaction chamber using additional mirrors and a fused silica plano-convex lens with a focal length of 25 cm.

3.4.5 The Probe Laser

The probe laser (used to ionise the molecules) here is a Radiant Dyes Narrowscan® dye laser pumped by a Continuum Powerlite Nd:YAG Laser.

Nd:YAG Lasers

Nd:YAG lasers involve emission of radiation at 1,064 nm from Nd^{3+} ions (via a four level system) which are held in an yttrium aluminium garnet ($Y_3Al_5O_{12}$) matrix. YAG is used due to its strength and high thermal conductivity. It is pumped optically using two flashlamps. The 1,064 nm output is doubled to 532 nm via second harmonic generation and then converted to 355 nm using third harmonic generation. The 355 nm YAG beam is used to pump the dye laser and has a pulse length of $\sim$7 ns. Fig. 3.10 shows the laser train as set up for the experiments described here.

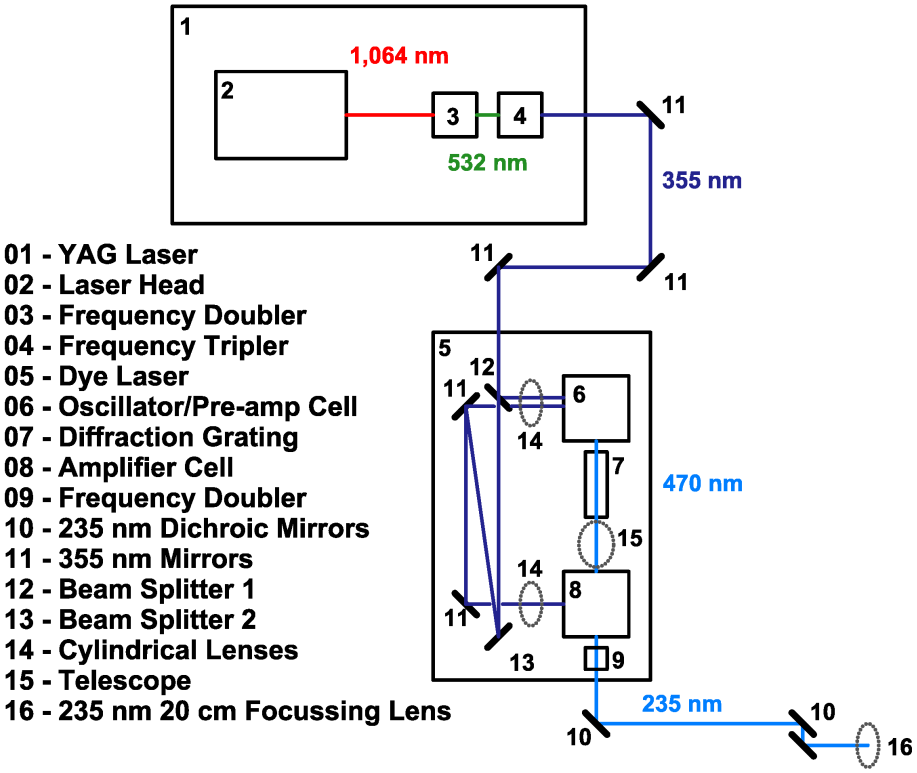

Figure 3.10: The probe laser beam path in the lab. 1,064 nm light is converted to 355 nm. This is directed via mirrors into the dye laser. In the dye laser a beam-splitter sends a small portion (∼10 %) into the oscillator cell. The remainder of the 355 nm light is then divided using mirrors and one more beam-splitter such that a second beam (the pre-amp) containing ∼25 % of the light enters the oscillator cell and the remaining 355 nm enters the amplifier cell. The wavelength light from the oscillator beam is tuned using a diffraction grating (usually to ∼470 nm). After being amplified by the pre-amp beam it passes through a spatial filter telescope, and then through an amplifier cell were the rest of the 355 nm light overlaps to amplify the 470 nm signal. After leaving the amplifier cell, the 470 nm is frequency doubled to 235 nm, before being reflected by several dichroic mirrors, through a focussing lens and into the chamber.

Dye Lasers

The lasing medium in dye lasers is a solution of dye which is circulated through the laser. Dye lasers can provide a wide range of wavelengths by altering the pump radiation wavelength and using appropriate dyes. For a given pump wavelength and a given dye, the dye laser's fundamental output is tuneable over 10 - 20 nm.

The efficiency of the dye laser is determined by the dye, and is usually between 10 % and 20 % with respect to the energy of the pump beam. For the experiments reported here, the dye laser beam is frequency doubled using a BBO crystal, producing horizontally polarised output with 0.5 to 1 mJ pulse energy. This beam is then directed through the chamber in a similar manner to the excimer beam (after optics are used to alter the polarisation such that it lies along the vertical). Prior to entering the chamber, the beam is focussed using a fused silica 1" diameter plane convex lens with a focal length of 20 cm from CVI, .

3.5 The Electrodes

3.5.1 Multiple Electrodes

VMI traditionally uses three electrodes. To achieve improved mass resolution, a longer TOF path is desirable in order to increase the "spreading-out" of fragments with different masses. Additionally, when using dc-slicing, it is beneficial to allow the NS to spread out in space, which allows a thinner centre slice to be obtained. This involves using lower voltages on the electrodes. The result of low voltages on the electrodes and longer TOF distances is that fast fragments recoiling parallel to the plane of the detector surface are likely to spread too far and miss the detector.

In theory this problem could be solved either by using a much larger MCP, which is cost prohibitive, or by using much higher voltages on the electrodes but, depending on the speed of the fragments, the high voltages needed would reduce temporal resolution by decreasing the TOF of the ions and would also reduce the effectiveness of dc-slicing.

Alternatively, additional electrodes can be added in order to extend the time and the region of space in which the ionised fragments are under the influence of the electric fields. This results in much tighter focussing of the NS in the two dimensions parallel to the detector, while still improving temporal resolution and yielding good conditions for dc-slicing. The apparatus described here uses a stack of twelve electrodes. In the present case, dc-slicing is a secondary benefit of using multiple electrodes. The primary benefit is the subsequent increase of the VMI area (see section 5.1).

In standard VMI (using three electrodes, the third of which is always kept at 0 V), the focussing conditions are crucially dependent on the "gradient ratio" between the repeller potential and the extraction potential. The space between the first and second electrode represents the "repeller region" and the space between the second and third electrode represents the "extraction

region".

When using more than three electrodes, both the repeller and extraction regions are spread over multiple electrodes. In the apparatus described here, the repeller region is spread over the first four electrodes and the extraction region is spread over electrodes seven to twelve. Electrodes four to seven constitute the "transition region". As a result, altering the gradient between these regions is more complicated. Appendix A.1 contains more details on how the voltages are calculated for different extraction:repeller ratios.

3.5.2 The Twelve Electrodes

Fig. 3.11 shows the design of the twelve electrode stack used in this apparatus. The electrodes are mounted over insulated ceramic tubes which surround threaded metal rods. The rods are fixed to a hollow cylinder which is mounted onto the feedthrough chamber section. The electrodes are 10 cm in diameter, 1 mm thick and are separated from one another by 9.5 mm thick ceramic spacers.

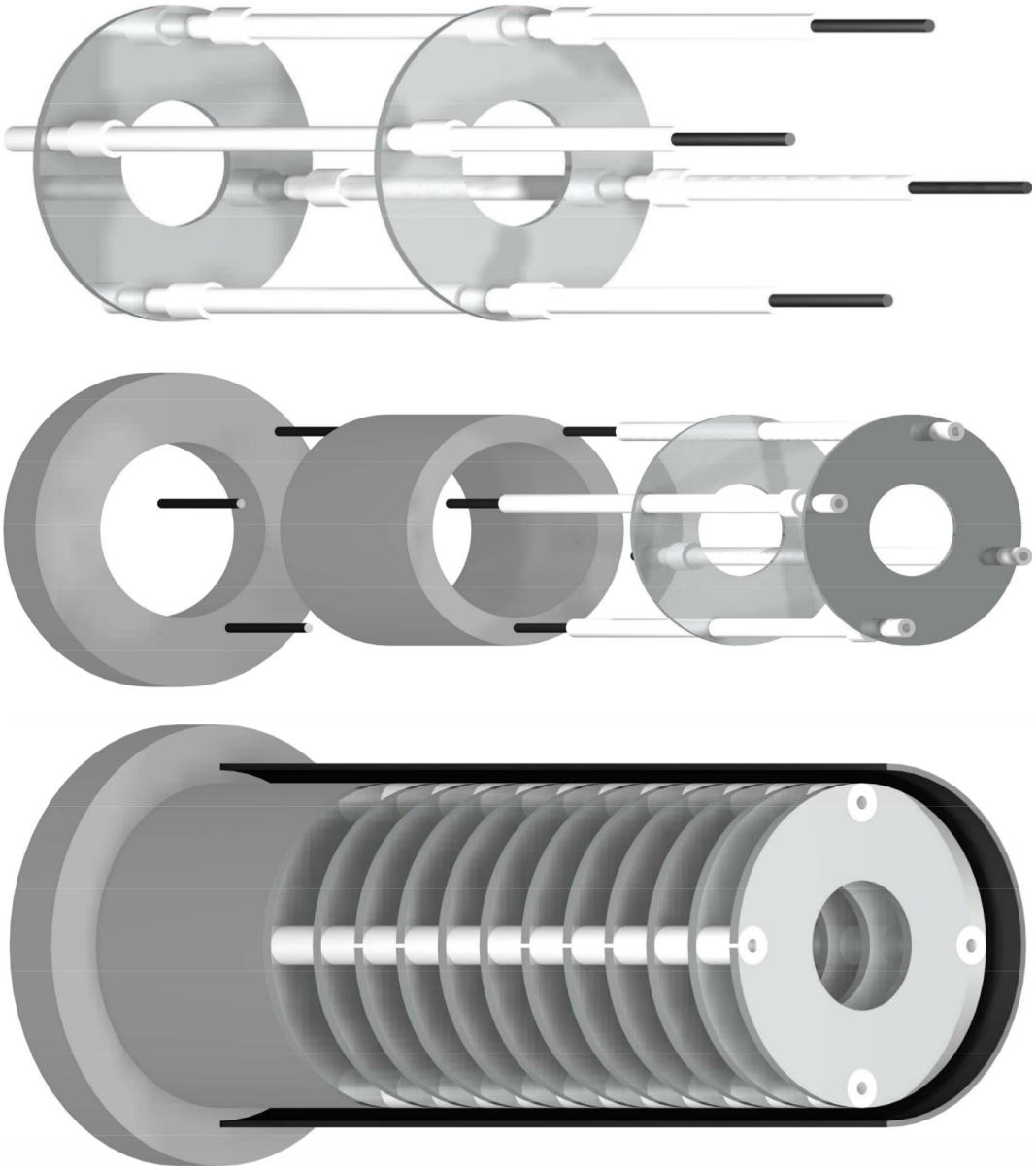

Figure 3.11: The electrodes are mounted over four insulated rods onto a metal cylinder and separated by insulated spacers (top image). The resulting electrode stack is mounted onto a hollow metal cylinder (centre image) which is itself mounted onto the inside of the reaction chamber. A metal shield (half of which is shown in the lower image) is mounted around the electrodes to minimise any interference from external fields.

3.5.3 Powering The Electrodes

Each electrode has a metal pin spot welded to its top, to which insulated copper wire is attached via a barrel connector. The wires are connected via additional barrel connectors to copper pins on the feedthroughs. The ends of the feedthrough pins on the outside of the chamber are connected via SHV cables to a homemade power supply.

The power supply consists of four Applied Kilovolts HP Series precision high voltage 5 kV modules (HP005PPP025). Electrodes one to four run on a single 5000 V power supply, as do electrodes seven to twelve, while electrodes five and six each have a dedicated power supply. Since electrode twelve is always ground, when a voltage is applied to electrode seven, the voltages across each remaining electrode drop by 20 % of the voltage on electrode seven. This is accomplished by a voltage divider within the power supply.

Electrodes one to four are slightly more complicated since the voltage on electrode four is not constant (as it is on electrode twelve): its voltage varies depending on the gradient ratio. As a result, once the gradient ratio is determined and electrode one is set, electrodes two to four are set by varying the resistance inside the power supply. There is of course a limit to the range over which these electrodes can be varied. The optimum extraction:repeller gradient ratio is usually around 2.4.

3.6 Detection

After the reactant molecules in the molecular beam are dissociated, the NS of fragments is ionised and repelled down the TOF tube, under VMI focussing conditions provided by the electrode stack, where they arrive at the detector. Several different methods are available to provide position sensitive detection. In the first report of PFI the detector consisted of a micro channel plate (MCP) detector coupled with a phosphor screen, and a CCD camera connected to a PC via a "frame-grabber" card. This is still the standard for VMI detection.

3.6.1 The MCP

The detector used here is a Burle Photonis 40 mm MCP coupled to a P43 phosphor screen. The MCP detector contains two MCPs, 40 mm in diameter, separated by a thin insulating ring. An MCP is an array of pores (each functioning as a single electron multiplier tube), each of which is tens of microns in diameter with a length:diameter ratio between 40 and 100 (40 here).[71] These pores are parallel and tilted at an angle to the normal of the MCP surface. The two MCPs are arranged in a "dual chevron" configuration, so called because of the relative alignment of the pores in the two plates. Fig. 3.12 shows a simple representation of an MCP.

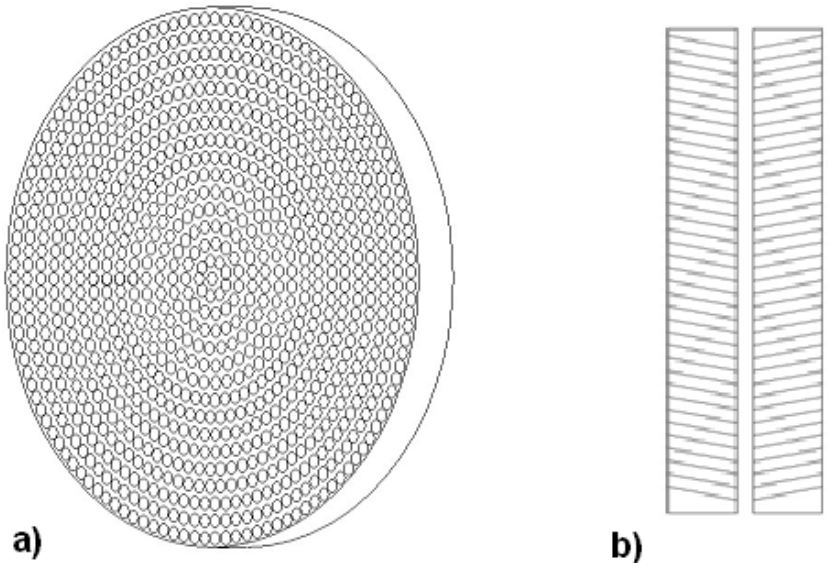

Figure 3.12: a) The front face of an MCP with exaggerated pore size. b) Side view showing the "dual chevron" alignment of adjacent pores within the plates

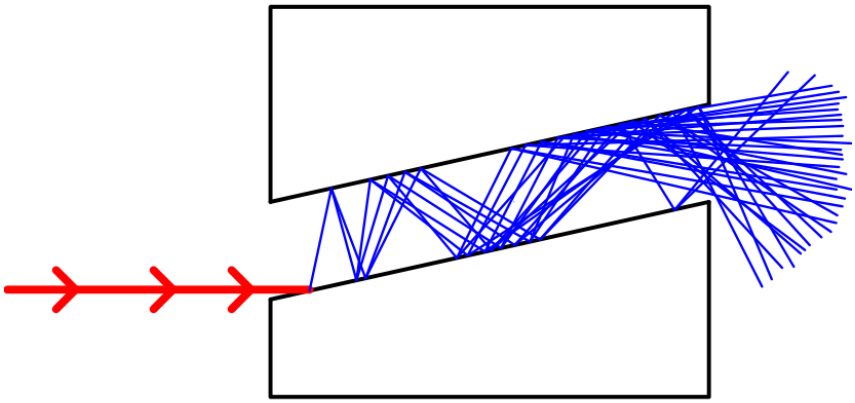

Figure 3.13: Close up side-view of one MCP pore showing the amplification resulting from the induction of a cascade of electrons (blue lines) upon collision of an ion, electron or photon (red line).

The inside of the pores is coated with a material which releases electrons easily when the plate is biased above a certain voltage (∼1500 V). If a photon, electron or ion impinges on one of the pores, electrons are ejected. These electrons travel a short distance down the pore before themselves colliding

with the pore's interior. This is repeated many times until the electrons exit the first MCP and enter an adjacent pore on the second MCP where the process repeats. The resulting cascade of secondary electrons amplifies the signal; one impinging particle ultimately produces on the order of 10^6 electrons. Fig. 3.13 is a simple representation of the amplification process.

MCP detectors traditionally had an integrating anode coupled to the rear of the second plate which measured the electrons exiting the rear of the second plate, thus providing a signal whose intensity corresponded to the number of electrons exiting the plate. In 1987 Chandler and Houston used an MCP detector which had the integrating anode replaced with a phosphor screen. As a result, the electrons exiting the rear of the second MCP collided with the phosphor screen, the point at which they collided then fluoresced.

The time delay between photofragments impinging on the first MCP and the phosphor screen fluorescing is negligible on the timescale of the experiments described here: the screen effectively fluoresces as soon the particles arrive at the first MCP. The length of the fluorescence on the phosphor screen depends on the material used. The half life of the fluoresence on a P43 screen is $\sim$1 ms. A DEI PVX-4140 pulser is used to pulse the MCP. It runs on two SRS-PS32S power supplies. The pulser outputs the lower of the two voltages (which is below the threshold for detection) as a default, and when triggered by a TTL pulse it switches to the higher voltage for as long as the trigger pulse dictates, before dropping back to the lower voltage. Fig. 3.14 shows the pulse generated by the MCP pulser, which has a $\sim$50 ns rise time.

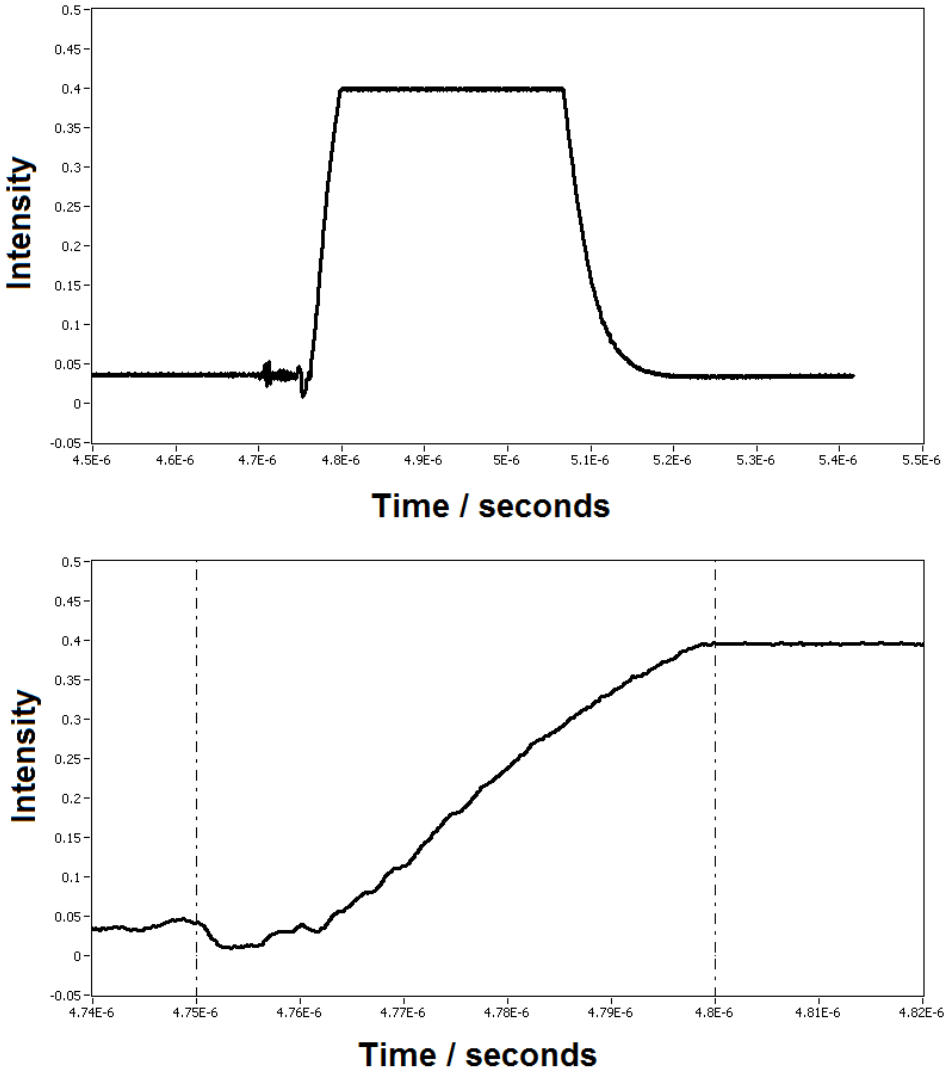

Figure 3.14: The output from the MCP pulser, read from the oscilloscope (upper image). The lower image shows a close up of the rise time of the pulse, which is ∼50 ns.

3.6.2 The CCD

The fluorescence of the phosphor screen is detected using a Foculus L-SV-FO614 CCD camera. The camera is pulsed at the same frequency as the experiment. It is "switched on" when the ions arrive at the MCP. The exposure time can be set to any value, though typically to avoid over-exposure this is in the region of 100 - 400 μs.

Once the CCD has recorded the image, it is transferred via a firewire cable to a National Instruments PCI-8254R frame grabber on the lab PC where the images are composited using custom-written programs to produce the final image, which is typically a composite of ∼20,000 single images.

3.6.3 Resolution

The resolution of an imaging experiment is defined as the ratio between the FWHM of the peak(s) in the kinetic energy distribution extracted from the images, and the total radius of the image. For a system employing an MCP / phosphor screen / CCD detection system, the ultimate resolution is usually limited by the available pixels on the CCD camera. For a 640×480 pixel CCD camera as used here, the limit is a result of the square of 480×480 pixels covering the 40 mm diameter phosphor screen. The ultimate resolution is therefore $\frac{1}{480}$, or ∼0.2 %.

In order to achieve this maximum resolution, the spread of ions of the same velocity must not exceed 0.08 mm (the length covered by a single pixel). This represents the best case, and most studies report a resolution of ∼1 % or so. Fig. 3.15 shows the peak in the radial distribution for a Cl fragment from the photodissociation of Cl_2 at 351 nm. The FWHM of this peak is ∼3.2 pixels, which corresponds to a resolution of ∼1.3 % for an image with a radius of 240 pixels. For the experiments described here this level of resolution is adequate, however techniques do exist which can provide sub-pixel resolution.[72]

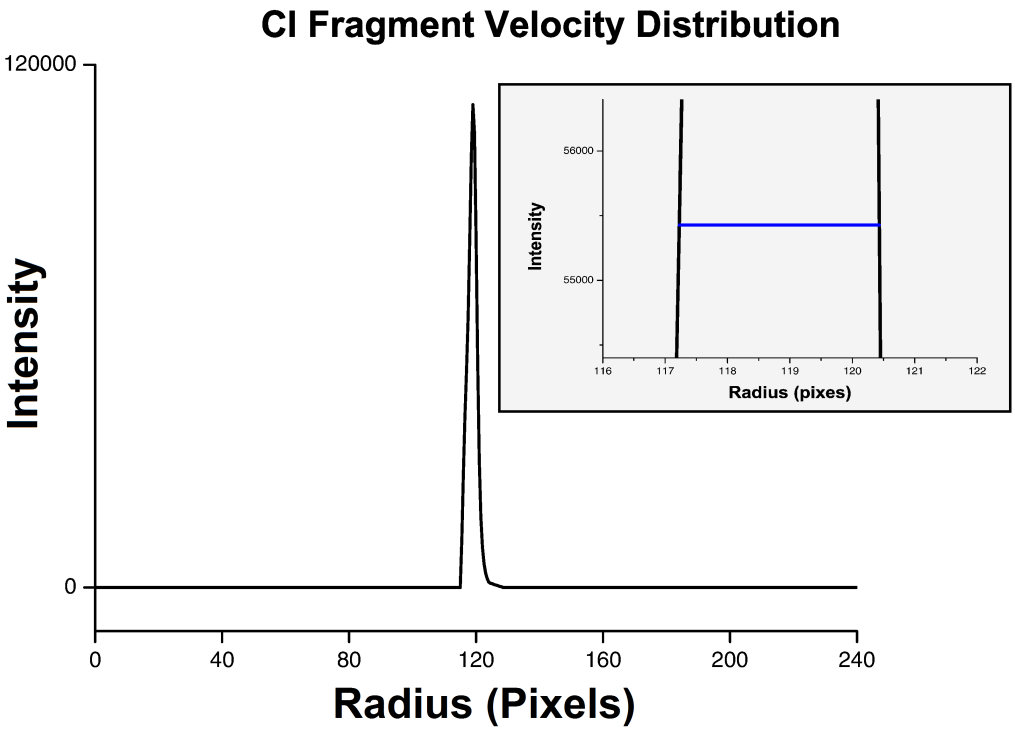

Figure 3.15: The radial distribution of Cl fragments from Cl_2 photodissociation at 351 nm. The distribution shows the intensity of the fragments as a function of the radius of the raw image (in pixels). The total radius of the image is 240 pixels and the FWHM of the peak is ∼3.2 pixels, i.e. a resolution of ∼1.3 %.

3.7 Control

The molecular beam valve and lasers in the experiments described here are pulsed at 20 Hz and the MCP detector is also pulsed when in imaging mode, as is the CCD camera. In addition, various parameters may be altered over the course of, or in between, TOF and imaging experiments. The probe laser may be scanned over a range of wavelengths or the time delay between pulsing the molecular beam and firing the laser may be varied, as may the opening time of the molecular beam, or the time delay between firing the pump and probe lasers. Pulsing the various pieces of equipment, and synchronising them, is accomplished by using two Stanford Research Systems DG-645 digital delay generators and custom-written programs. The acquisition of images and TOF data is accomplished with the CCD camera and oscilloscope respectively, and additional custom-written programs.

3.7.1 The Delay Generators

The SRS delay generators contain four channels each, with each channel continually outputting a TTL (transistor transistor logic) signal voltage. The value of the TTL signal is either 0 V or, while the pulse is applied, 5 V.

τ_S and τ_E (the start and end times of the pulse respectively) can be set to any value within the range of the timebase. At 20 Hz this is between 0 ms and 50 ms. In addition, τ_S and τ_E can either be set with respect to the start of each cycle (time 0, concurrent with the probe laser firing), or with respect to a τ value on any other channel. Fig. 3.16 shows the TTL pulse timings for an imaging experiment on this apparatus, and Fig. 3.17 shows a pulse from a delay generator channel.

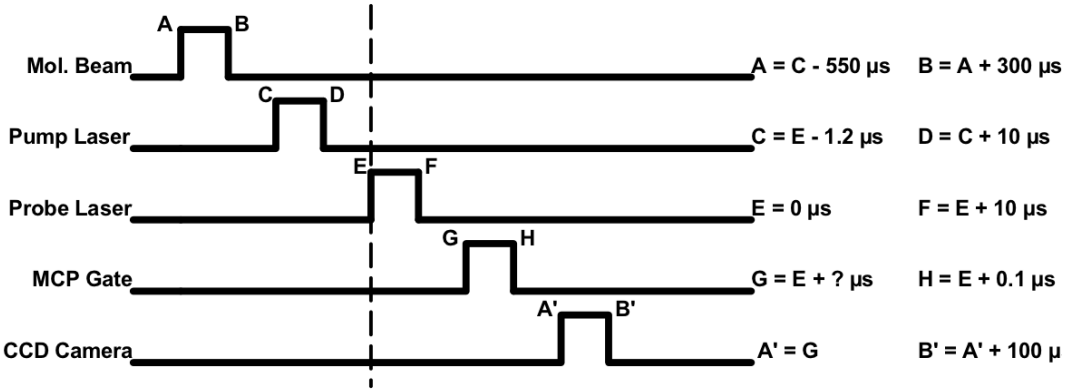

Figure 3.16: The delay generators output up to eight TTL pulses which are used to synchronise the various pieces of the apparatus. The timings for a typical VMI experiment are shown. The MCP gate (G) position varies depending on the mass/charge ratio of the fragment and the voltages on the electrodes.

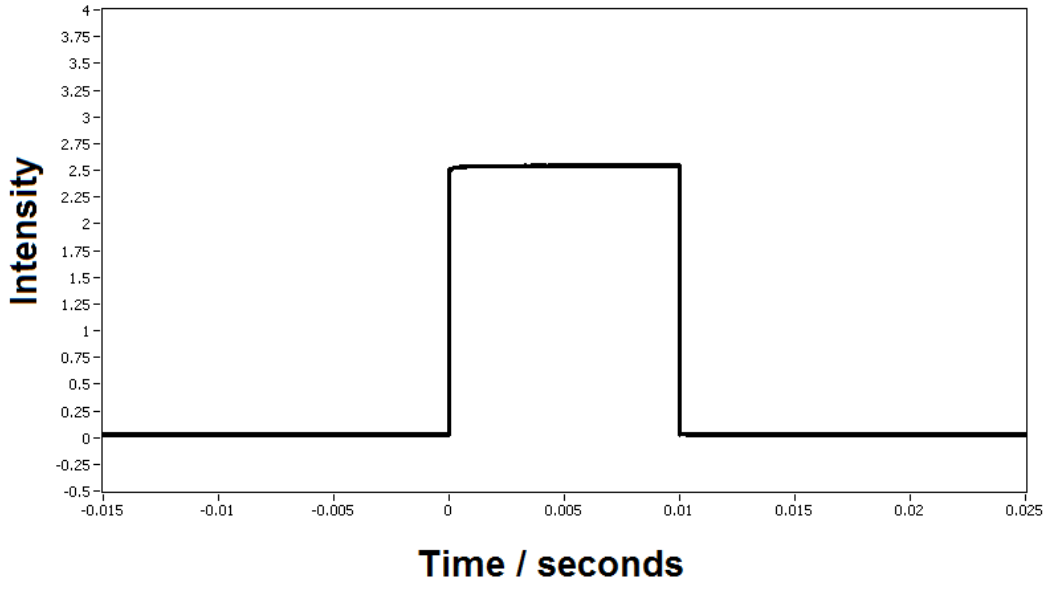

Figure 3.17: A 10 ms pulse from a delay generator channel showing the switch from 0 V to 5 V, read from the oscilloscope.

3.7.2 The Oscilloscope

The oscilloscope receives three signal inputs. The first is from the detector, from which the detector's signal is read out in real time. The second is the TTL signal used to pulse the probe laser, which serves to define the "start" time of the oscilloscope trace: each time the probe laser is fired the oscilloscope

begins a new trace. The molecular beam is fired with a negative time delay (relative to the probe laser) and the MCP is pulsed on at a positive time delay to detect the ions produced. The TOF of particles is easily determined. They start to fly down the TOF tube when the probe laser is fired (time zero on the scope trace) and their arrival time at the detector can be read straight off. Thirdly, the MCP pulser signal is fed into the scope and displayed alongside the TOF trace, this provides visual feedback of the position of the MCP gate thus enabling it to be more easily positioned over the centre of the NS's arrival time.

3.7.3 The PC

While all of the equipment can be controlled manually by using the delay generators, data acquisition requires the use of a PC. The PC contains four connections to the apparatus. It is connected to the delay generators by means of a GPIB cable which allows the trigger pulses for the kit to be varied remotely. It is connected to the oscilloscope with a standard ethernet cable which allows the TOF trace to be read by the PC. The probe laser is controlled by the PC using a serial RS232 connection, allowing the wavelength to be altered or a scan over a range of wavelengths to be carried out. Finally, the CCD camera is connected via a firewire cable so that the images may be read in real time, stored in the PC and composited into a final image.

3.7.4 LabVIEW

Accomplishing the above tasks (amending the trigger pulses, varying the wavelength, reading traces from the scope and processing images) required custom programs to be written. The programs were created using the LabVIEW development environment from National Instruments.[73] LabVIEW is a suite for writing computer programs, with a highly extensive library containing drivers and sub-programs which can perform a wide variety of tasks and interface

with almost any piece of equipment. LabVIEW programs are written in its own programming language, called "G". This is a graphical language: rather than writing the commands via standard ASCII characters in a text document, each function exists as an icon. Several programs have been created to carry out various tasks with the apparatus.

Wavelength Scans - REMPI-TOF Spectra

A program was created which reads TOF data from the scope while varying the wavelength of the probe laser. A National Instruments DAQmx is used in order to count each experimental cycle. The start and end wavelengths of the scan are defined, as is the step size (interval between successive wavelengths) and the number of shots to be averaged at each step.

The program begins by setting up a two dimensional array: one column for the values of the wavelengths scanned, and another for the integrated signal intensity detected at that wavelength. The laser is then moved to the starting wavelength. The program integrates the area under the peak in the TOF trace on the oscilloscope for each laser shot. After integrating the signal from the specified number of shots, the integrated intensity values are averaged and added to the array. The laser is then moved to the next wavelength value and the process is repeated. The number of reaction cycles is counted by wiring one of the delay generator channels to a National Instruments DAQmx, which counts the number of TTL pulses sent to the molecular beam pulser (i.e. counts the number of reaction cycles). When completed, the array is saved to a text file, which can then be analysed.

Producing Images

Imaging is accomplished with another custom-written program which functions as follows. The number of images to be obtained is defined. The first image is read from the CCD camera via the frame grabber and stored in a buffer

(temporary) file. The second image is then read in the same manner but rather than being stored directly, the first image is called from the buffer, the two images are added together, the buffer file is emptied, this new composite is stored there and the process repeats. The start and end wavelengths are defined, the interval size is fixed as 0.02 cm^{-1} (defined by the probe laser's bandwidth) and an equal number of images are collected at each wavelength interval to ensure full imaging of the molecules travelling in all directions. This is due to the Doppler Effect: if the Doppler profile of the transition is not fully scanned then the image produced will be biased, i.e. it will have higher intensity in certain areas of the image.

Once the desired number of images have been acquired (again accomplished by using the DAQmx to count the number of reaction cycles) the final composite image is stored as a TIFF file and can then be analysed. After implementing this imaging program on this apparatus, a copy of it was provided to the Signorell group who now use it for their imaging experiments.[74]

Chapter 4

Gas Phase VMI - Photodissociation of Chloroform

4.1 Chloroform Background

Chloroform ($CHCl_3$) is a common organic solvent.[75] Deuterated chloroform ($CDCl_3$) in particular is widely used as a solvent for NMR spectroscopy.[76] $CHCl_3$ was also used to replace ether as an anaesthetic in the 1800's, however after its toxicity was discovered it fell out of use for this purpose. Additionally, it is industrially relevant as it is used to produce polytetrafluoroethylene (PTFE).[77] In atmospheric chemistry, the Cl radicals produced from the photodissociation of $CHCl_3$ have the potential to contribute to the depletion of ozone:[78,79]

$$CHCl_3 + h\nu \rightarrow CHCl_2 + Cl$$

$$Cl + O_3 \rightarrow ClO + O_3$$

$$ClO + O_3 \rightarrow Cl + 2O_2$$

In more fundamental terms, chloroform is one of the simplest examples of the class of alkyl halide molecules. Previous studies on alkyl halides have used molecules similar to chloroform, such as chloromethane, in order to draw conclusions about the various potential energy surfaces of a number of different quantum states of alkyl halides.[80] In general, alklyl halides are found to be generally similar in the arrangement of their low-lying potential energy surfaces (see below).

However, in the case of the breaking of the C-Cl bond in small alkyl halides, chloroform represents an increase in complexity when compared with a simple molecule like chloromethane. In chloromethane, the single C-Cl bond which is broken lies along the main C_3 symmetry axis of the molecule, while in chloroform, the C-Cl bond (of which there are three) being broken lies at an angle of $\sim 109.5^{\circ}$ to the symmetry axis, which has consequences for the dynamics of C-Cl dissociation (see below).

Finally, previours studies on chloroform have yielded a wide variety of results. Branching ratios and parameters have been reported by a number of

groups, which display notable variation. Since these studies were carried out before the advent of VMI, it can be considered worthwhile to revisit chloroform using VMI in order to disentangle the, up to now, confused picture of its dissociation dynamics.

4.1.1 $CHCl_3$ Dissociation Pathways

The dissociation dynamics of chloroform and similar compounds have previously been studied by a variety of methods.[81–88] Experiments at various wavelengths have been used to probe the Q ← N transitions (see section 4.1.2) and several features about the dissociation have been determined. Throughout this wavelength region, several dissociation processes have been observed:

$$CHCl_3 + h\nu \rightarrow CHCl_2 + Cl$$
$$CHCl_3 + h\nu \rightarrow CHCl_2 + h\nu \rightarrow CCl_2 + H$$
$$CHCl_3 + h\nu \rightarrow CHCl_2 + h\nu \rightarrow CCl + HCl$$
$$CHCl_3 + 2h\nu \rightarrow CH$$

The production of the H atom is through a secondary photodissociation process.[86] The production of HCl is energetically more favourable than the production of Cl but, as in the production of H, a secondary photodissociation is required.[82] The formation of CH occurs at 193 nm, but this is a two photon process.[87] Therefore, for single-photon Q ← N electronic transitions, and in the absence of secondary photodissociation processes, the favoured reaction pathway for chloroform dissociation results in the breaking of a C-Cl bond.

4.1.2 The $CHCl_3$ Q Band Surfaces

The lowest energy electronic transition in the alkyl halides is broad and centred around 175 nm, and results from transitions between the (ground) "N state" and the "Q band".[80,85] This transition is the result of an electron being

promoted from a non-bonding π orbital on the halide atom to an antibonding (σ^*) orbital on the carbon-halide bond. Mulliken was the first to describe the energy surfaces comprising the Q band of alkyl halides.[80] A total of five surfaces constitute the band, and these are labelled: $^3Q_1$, $^1Q_1$, $^3Q_0{}^+$, $^3Q_0{}^-$ and $^1Q_2$. Transitions to $^3Q_0{}^-$ and $^1Q_2$ are dipole forbidden and so these two states may be neglected when discussing photodissociations via the Q band.

The ground state, N, has A_1 symmetry. Of the excited states, $^3Q_0{}^+$ has A_1 symmetry and $^3Q_1$ and $^1Q_1$ have E symmetry. The two lower states ($^3Q_1$ and $^1Q_1$) correlate with ground state Cl atoms ($^2P_{3/2}$) and the uppermost state ($^3Q_0{}^+$) correlates with spin-orbit excited Cl* ($^2P_{1/2}$). Finally, there is the potential for curve crossing between the $^1Q_1$ and the $^3Q_0{}^+$ states. The PESs of the N and Q states are shown in Fig. 4.1.

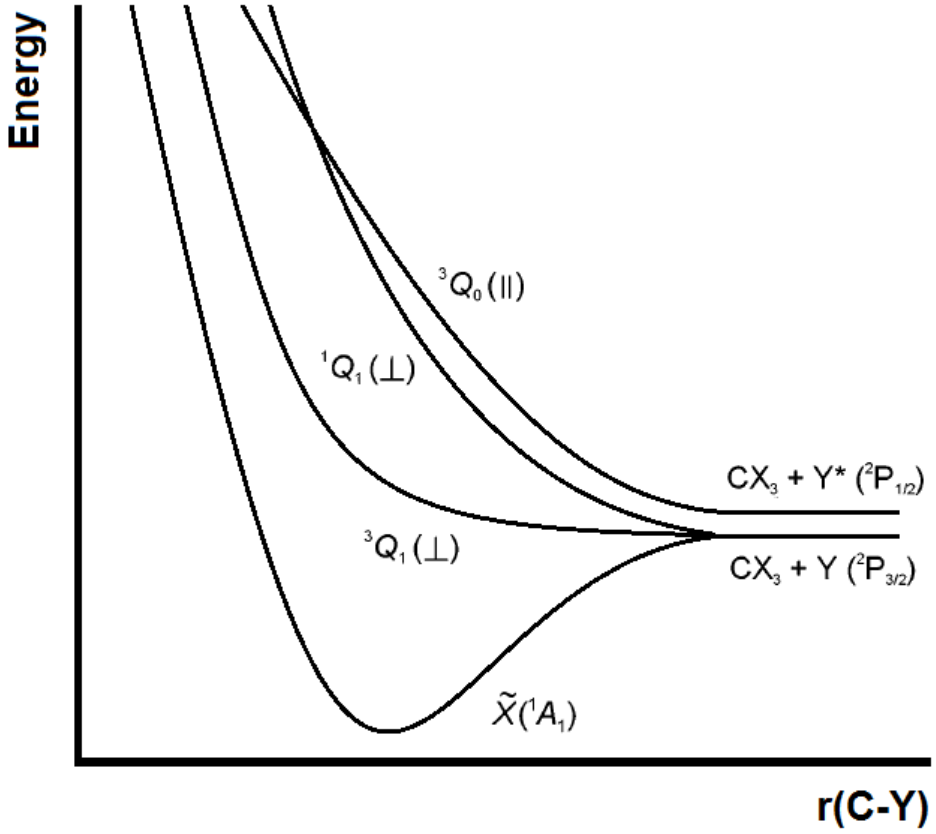

Figure 4.1: The PESs constituting the N state and Q band of CH_3Cl.[88] These states are analogous for chloroform, and have been shown to be applicable to alkyl-halides in general.[80] The lower two excited states ($^3Q_1$ and $^1Q_1$) correlate to ground state Cl products, and are of different symmetry than the ground state and therefore transitions to these will have perpendicular character. The uppermost state ($^3Q_0{}^+$) correlates with spin-orbit excited Cl* products and has the same symmetry as the ground state. Transitions to this state will have parallel character. In addition, the $^1Q_1$ and $^3Q_0{}^+$ states can undergo curve crossing.

4.1.3 Previous Experimental Results

The results from previous studies of $CHCl_3$ dissociation via the Q band display notable variation. The kinetic energy of the Cl fragments was measured by Huber and co-workers using PTFS. They reported that a high proportion of the available energy after dissociation (43 %) was channelled into translation. At 193 nm, they measured a kinetic energy of 0.94 eV for Cl fragments, but did not distinguish between Cl and Cl*.[81] Matsumi *et al.* measured the kinetic energy of Cl at 193 nm using Doppler-resolved REMPI spectroscopy, and reported an

average kinetic energy of 0.54 eV for Cl fragments.

The branching ratio ([Cl*]/[Cl]) from 193 nm $CHCl_3$ dissociation has been measured by several groups with values of 0.25, 0.32 and 0.43 having been reported.[82–84] These branching ratios, while not hugely consistent, point to the involvement of multiple excited states in the Q band dissociation of chloroform. Dissociation via a single PES will result in fragments all produced in the same quantum state. The presence of both Cl and Cl* fragments must result from excitation to, and dissociation on, at least two different excited state surfaces, or excitation to a single excited state surface, followed by curve crossing to another excited state which correlates with a different internal state of the products.

The above-mentioned PTFS study reported an isotropic distribution of Cl fragments ($\beta \approx 0$), which was attributed to the presence and involvement of at least two repulsive states, in agreement with the conclusions reached by other groups from their measurement of branching ratios. Other β parameters have been reported for chloroform dissociation at similar wavelengths, but these have been for two-photon dissociation processes.[85,86]

4.1.4 $CHCl_3$ β Parameters

Suits and co-workers investigated CH_3Cl at 193 nm using velocity map imaging, and reported β parameters of -0.46 and -0.74 for Cl and Cl* respectively. However, while chloroform is very similar to CH_3Cl in terms of structure and dynamics (the same Q band energy surfaces are involved in the dissociation and the C-Cl bond breaks in a similar fashion), there is one important difference between the two molecules. The C-Cl bond being broken lies along the main C_{3V} symmetry axis in CH_3Cl, while in $CHCl_3$, it lies at $\sim 109.5^{o}$ to the symmetry axis (which lies along the C-H bond in chloroform). As a result, the β parameters obtained for CH_3Cl cannot be compared to those for $CHCl_3$, and the limiting cases for the β parameters for chloroform dissociation are not

2 and -1 as they are for simple diatomics, or for CH_3Cl.

For a polyatomic molecule the β parameter can be expressed as:

$$\beta = 2P_2(\cos(\chi))$$
$$P_2(\cos(\chi)) = \frac{1}{2}(3\cos^2\chi - 1)$$

P_2 is the second order Legendre polynomial and $\chi = \pi - \alpha$ with α being the angle between the transition dipole moment and the recoil vector (here the C-Cl bond). In the case of chloroform, χ takes a value of $\sim 70.5^{\circ}$. Using this value in the above equation yields limiting cases for β of $\frac{1}{3}$ for a purely perpendicular transition, and $-\frac{2}{3}$ for a purely parallel transition.[83]

4.2 Chloroform Experimental

4.2.1 Calibration

Kinetic Energy Calibration

Fig. 4.2 shows an image of ground state Cl fragments which were ionised with a 2+1 REMPI scheme at ∼235 nm after being produced by dissociation of Cl_2 at ∼351 nm. Also shown is the intensity of the image as a function of the radius in pixels (the raw velocity distribution obtained from the image). The kinetic energy of the Cl fragments is known to be 0.51 eV and, using a voltage of 2.5 kV on the repeller electrode and a gradient ratio of 2.4, the fragments here produce a ring with a radius of 119 pixels. Velocity map imaging produces an image whose radius is directly proportional to the square root of the kinetic energy. Thus, the image radius can be converted from pixels to kinetic energy:

$$\mathrm{E}_{Kin} = (0.006 \times \mathrm{pixels})^2$$

This relationship holds for fragments of any mass and kinetic energy, provided the experimental parameters are maintained (i.e. 2.5 kV on the repeller electrode and a gradient ratio of 2.4, the same voltage on the MCP detector etc).

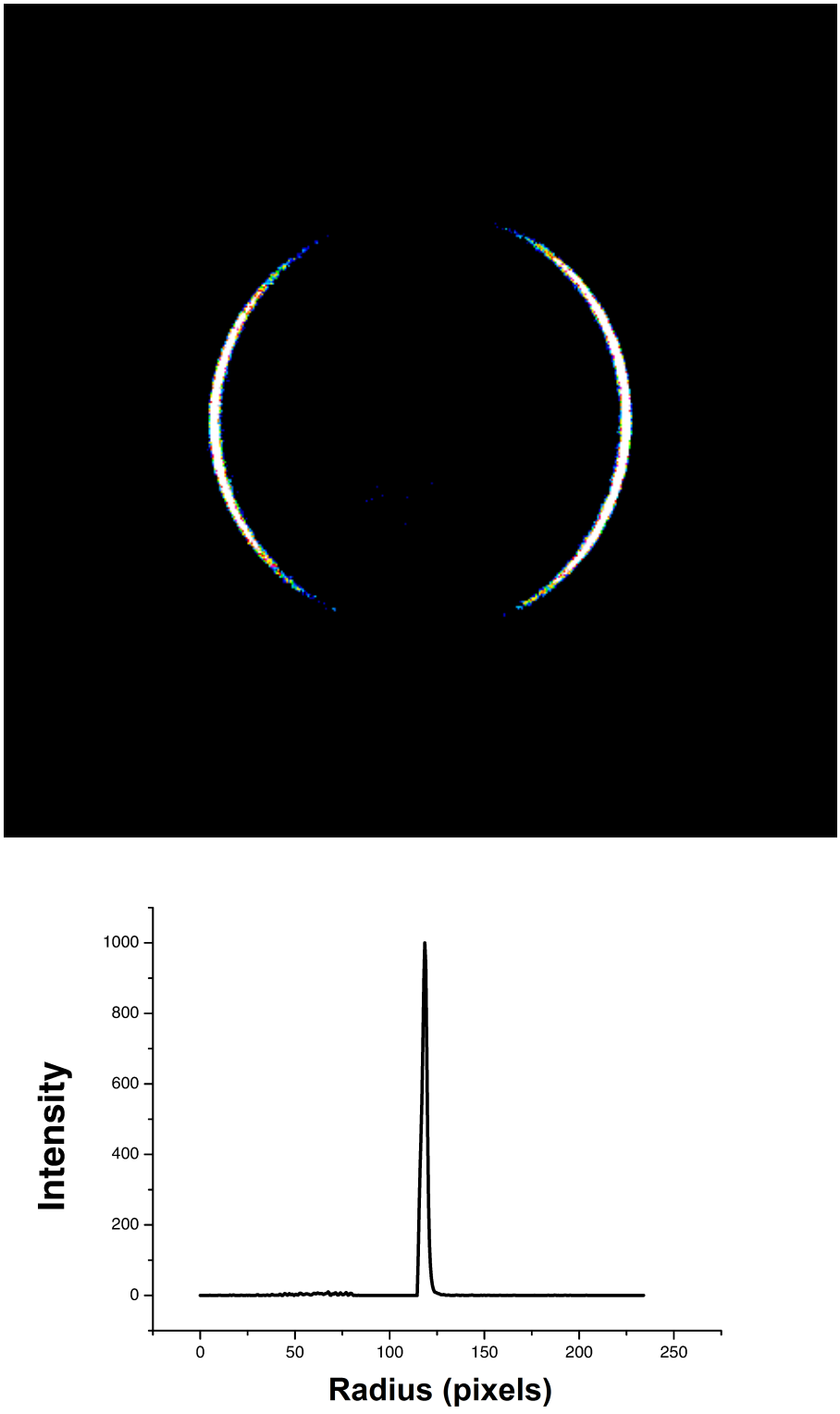

Figure 4.2: The raw VMI image of ground state Cl fragments produced from the 351 nm photodissociation of Cl_2 and ionised using a 2+1 REMPI scheme (top). The raw velocity distribution obtained from the image (bottom).

Branching Ratio Calibration

Ground state Cl ($^2P_{3/2}$) and spin orbit excited Cl* ($^2P_{1/2}$) fragments from 351 nm Cl_2 dissociation were used to calibrate the apparatus for branching ratio measurements. Both fragments were ionised using a 2+1 REMPI scheme. The Cl fragments underwent two photon excitation to the $^2P_{3/2}$ level (~85,442 cm^{-1} above the ground $^2P_{3/2}$ state), and the Cl* fragments were ionised via the $^2P_{1/2}$ level (~84,362 cm^{-1} above the Cl* $^2P_{1/2}$ state).[89]

The areas under the peaks in the Cl REMPI spectrum obtained after dissociation of Cl_2 at 351 nm were integrated for each fragment, and the ratio of their intensities was calculated to be 0.005. Fig. 4.3 shows the REMPI spectrum of the Cl and Cl* fragment peaks from chloroform dissociation at 193 nm. It is possible to correct for errors stemming from detection efficiency (different line strengths etc) by using a value of 0.016 for [Cl*]/[Cl] at 351 nm Cl_2 dissociation (obtained from the literature).[90] This yields a conversion factor of 3.125, which must be applied to the results obtained here for [Cl*]/[Cl].

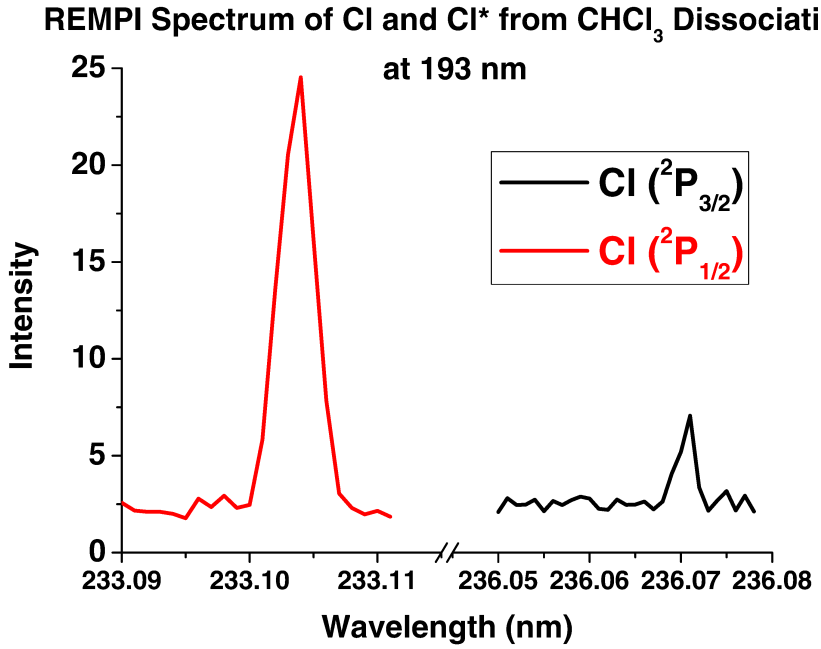

Figure 4.3: REMPI spectrum showing the peaks for Cl (red) and Cl* (black) fragments.

As with the imaging experiments, by maintaining the experimental conditions for chloroform dissociation and probing the Cl fragments using the same REMPI scheme as above, the branching ratio conversion factor can be reliably applied to extract the branching ratio of the Cl and Cl* fragments from $CHCl_3$ photodissociation.

4.2.2 Chloroform Experiments

A mixture of ∼4 % $CHCl_3$ seeded in He was used to form a molecular beam ∼300 μs long. The molecular beam was directed along the TOF axis of the VMI spectrometer, passing through a 2 mm hole in the centre of the repeller electrode. Between the first and second electrodes the molecular beam was intersected by the pump laser beam.

For one colour experiments this was a vertically polarised 235 nm beam produced using the 3rd harmonic of a Continuum Powerlite 8020 Nd:YAG laser to pump a Radiant Dyes Narrowscan dye laser containing Coumarin 480 dye whose output was frequency doubled to yield photons of ∼235 nm. The beam was focussed using a spherical convex lens with 25 cm focal length.

For two colour experiments a 193 nm pump laser beam was produced using a Questek Series 2400 Excimer laser. The ∼30 mJ output of the excimer laser was polarised using a quartz window mounted at the Brewster angle (see section 3.4.4) to yield a vertically polarised beam with ∼0.8 mJ pulse energy which was focussed using a convex lens with a focal length of 20 cm.

After dissociation, the 235 nm dye laser beam was used to ionise the Cl fragments using a 2+1 REMPI scheme. Ground state Cl were ionised via the excited $^2P_{3/2}$ state at a wavelength of ∼233.01 nm and excited state Cl* fragments were ionised via the $^2P_{1/2}$ state at a wavelength of ∼236.07 nm (see Fig. 4.3). The ionised Cl fragments were accelerated using an electrode stack containing twelve electrodes, with the first (repeller) electrode biased at 2.5 kV, and with a gradient ratio of 2.4 between the extraction and repeller

regions.

The MCP detector was gated for ∼80 ns over the centre of the Cl^+ NSs to produce VMI images. The resulting fluorescence on the P43 phosphor screen was captured with a Foculus CCD camera with an exposure time of ∼200 μs. The final images were composites of the images produced from ∼15,000 laser shots and the β parameters and kinetic energies were extracted from the raw images using BASEX.[55] From the radius of the images, the kinetic energies of the fragments were determined using the relationship derived from the previously described 351 nm Cl_2 calibration.

The branching ratio measurements were carried out under the same conditions as the imaging experiments, with the detector functioning in continuous mode, and the areas under the peaks corresponding to Cl and Cl* were integrated. The relative intensities were used to determine the ratio between Cl* and Cl, which provided branching ratio values after correction using the previously determined conversion factor of 3.125.

4.3 Results

Fig. 4.4 shows the VMI images of ground state Cl fragments produced from the photodissociation of chloroform at 193 nm and 235 nm, along with the velocity distributions obtained from the images.

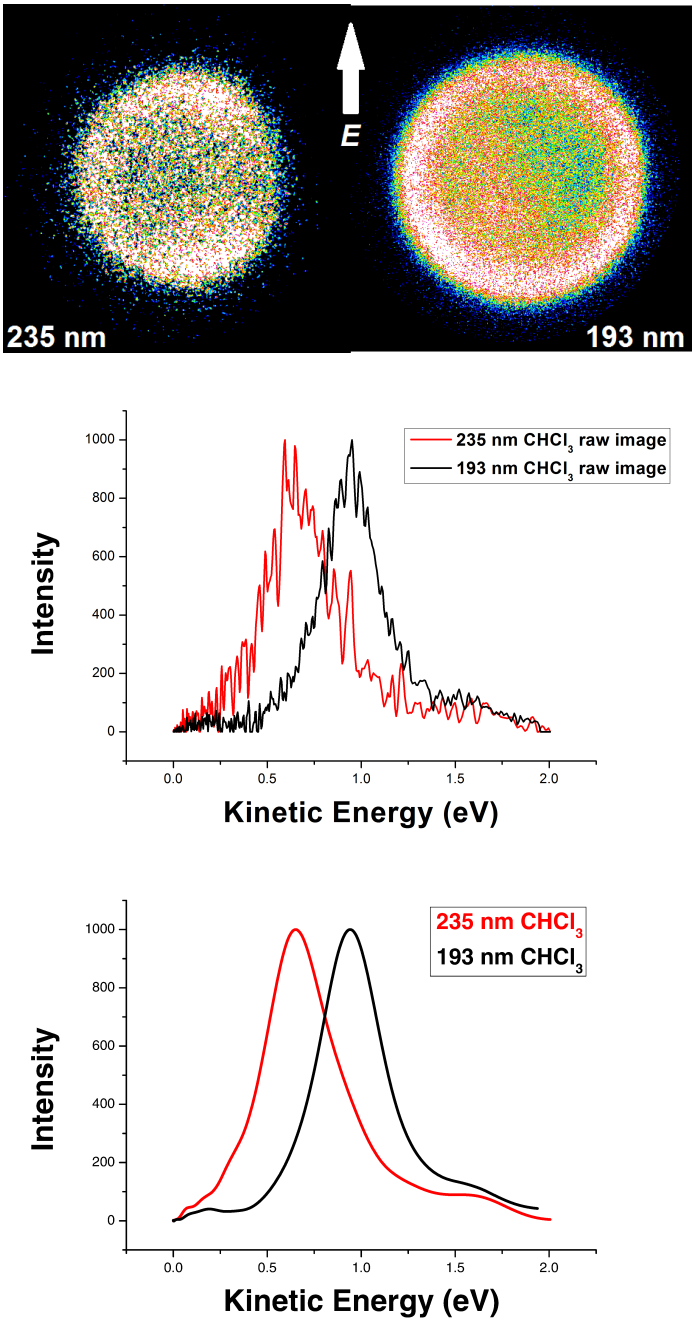

Figure 4.4: VMI images of ground state Cl fragments produced from dissociation of $CHCl_3$ at 235 and 193 nm with vertical laser polarisation. Also shown are the kinetic energy distributions of both fragments, obtained by extracting an intensity versus radius distribution in BASEX, and converting the radius in pixels to kinetic energy in eV via calibration with the 351 nm dissociation of Cl_2. The distributions in the centre are from the raw data, those on the bottom have been smoothed using a FFT.

Table 4.1 summarises the information obtained from the imaging and branching ratio experiments on $CHCl_3$ at both photodissociation wavelengths.

	193 nm		**235 nm**	
	Cl ($^2P_{3/2}$)	**Cl* ($^2P_{1/2}$)**	**Cl ($^2P_{3/2}$)**	**Cl* ($^2P_{1/2}$)**
β **Parameter**	-0.05	0.3	0.2	0.3
<E_{Kin}> (eV)	0.94		0.65	
Branching Ratio ([Cl*]/[Cl])	1		0.3	

Table 4.1: $CHCl_3$ Results Table

4.4 Discussion

The kinetic energy distributions of the Cl and Cl* fragments are broad and peak at ∼0.65 eV and ∼0.94 eV for photodissociation at 235 nm and 193 nm respectively. The Cl* fragments have kinetic energies approximately 0.08 eV lower than Cl fragments, which is consistent with the energy difference due to spin-orbit excitation. These values are comparable with those reported by Huber and co-workers, but are higher than those measured by Matsumi *et al.*[81,83] The products observed can be attributed to single photon dissociation as a second set of rings corresponding to two-photon excitation was not observed.

The β parameters for both fragments at both wavelengths are shown in Table 4.1. It can be seen that the ground state Cl fragments produced by 193 nm dissociation have an isotropic angular distribution, while the other fragments have β parameters close to $\frac{1}{3}$, which indicates their production via perpendicular excitation of the parent $CHCl_3$ molecule. The β parameter for

ground state Cl fragments at 193 nm is indicative of an isotropic distribution of photofragments. This could be as a result of several processes. Transition saturation can produce an isotropic distribution, however, the laser energy was mantained at a sufficiently low level to avoid saturation during all reactions. The absence of isotropy for excited state Cl* at 193 nm with the same laser energy serves to confirm the absence of saturation for ground state Cl. In principle, saturation can also be the result of a fast rotation of the parent molecule between excitation and dissociation. This is most probable in the case of a secondary photodissociation process, which has already been ruled out. In addition, given the similarity of the various states involved, it seems unlikely that a fast rotation could produce isotropy in pathway but not others.

The branching ratios ([Cl*]/[Cl]) at both wavelengths have been measured, and are found to be 1 for 193 nm dissociation, and 0.3 for 235 nm dissociation, indicating enhanced Cl* production at higher photon energies.

The above results imply the involvement of multiple excited states in the Q band in the near threshold dissociation of $CHCl_3$.

At 193 nm, [Cl*]/[Cl] is 1 and the β parameter for Cl* is 0.3. This implies dissociation via a perpendicular transition, which must result from the ground N state being excited to the $^1Q_1$ state. $\beta = 0.3$ may also indicate excitation to $^3Q_1$, however both $^1Q_1$ and $^3Q_1$ correlate with ground state Cl atoms, and only the $^1Q_1$ can cross with the $^3{Q_0}^+$ state which correlates with excited Cl*. Consequently, it seems probable that the production of Cl* from 193 nm dissociation of $CHCl_3$ results predominantly from excitation to $^1Q_1$, followed by curve crossing to $^3{Q_0}^+$.

The ground state Cl fragments from 193 nm dissociation have an isotropic distribution. In principle this can be attributed to two factors. The dissociation for this channel could occur on a time scale longer than a rotational period of the molecule. Alternatively, the Cl fragments may be produced via two different excitation processes, one parallel and one perpendicular which, when

imaged concurrently (and assuming approximately equal numbers of fragments produced via both pathways) result in the isotropic distribution. The fact that the other fragments produced here exhibit fairly anisotropic distribution would suggest that the latter explanation of the Cl isotropic angular distribution at 193 nm is most probable. The β parameter of 0 is most likely the result of the product fragments being produced via two (or possibly three) reaction pathways. The $CHCl_3$ being excited to the $^3Q_0^+$ state, and then crossing to the $^1Q_1$ state should result in Cl fragments with $\beta = -\frac{2}{3}$. Along with this, Cl fragments with $\beta = \frac{1}{3}$ can be produced by excitation to $^1Q_1$ followed by direct dissociation on this surface, with the combination of both processes yielding an isotropic distribution of Cl fragments. There may also be a contribution from excitation and direct dissociation on the $^3Q_1$ surface, but this cannot be distinguished from direct dissociation via $^1Q_1$.

It is interesting to note that, for 193 nm dissociation, it appears that the vast majority of excitations to $^3Q_0^+$ are followed by curve-crossing to $^1Q_1$. i.e. there does not appear to be any direct dissociation process on $^3Q_0^+$ to produce Cl*, rather, the Cl* products seem to result from a process involving curve-crossing (from $^1Q_1$ to $^3Q_0^+$). The Cl fragments, on the other hand, appear to result from a combination of direct dissociation on $^1Q_1$ (and possibly $^3Q_1$) and dissociation involving curve crossing in the opposite direction to that which produces Cl* (i.e. as well as direct dissociation, Cl is produced via crossing from $^3Q_0^+$ to $^1Q_1$).

A branching ratio of 1, and a β parameter of $\sim$0.3 for Cl* fragments seem to imply that, at 193 nm, around half of the parent $CHCl_3$ molecules are promoted to $^1Q_1$, after which they undergo curve crossing to the $^3Q_0^+$ surface. Of the remaining molecules, it could be proposed that around half are excited to $^1Q_1$ (and/or $^3Q_1$) where they directly dissociate, and around half to $^3Q_0^+$ were they undergo curve crossing to $^1Q_1$, which would explain the isotropic angular distribution of Cl fragments.

At 235 nm, due to the photon energy being ∼1.15 eV lower, the $^3Q_0^+$ surface appears to be less accessible. This is deduced from the β parameter of 0.2 for Cl fragments at 235 nm. When compared with the β parameter of 0 at 193 nm, it is clear that the 235 nm dissociation results in Cl fragments with an angular distribution indicative of an initial excitation with much more perpendicular character, i.e. reduced parallel character. Since only excitations to $^3Q_0^+$ produce Cl with recoil velocities indicative of a parallel excitation, it can be surmised that the increased perpendicularity implied by the Cl fragment angular distributions at 235 nm is a result of fewer excitations to the $^3Q_0^+$ state.

Furthermore, for vertical transitions from the ground state, the $^3Q_0^+$ and $^1Q_1$ curves have been determined to be relatively close together (see Fig. 4.1). Assuming that $^3Q_1$ has minimal or no involvement (as has been assumed in previous studies), then it is probable that the ratio of Cl* products (produced via $^3Q_0^+$ crossing to $^1Q_1$) and Cl products (produced via $^1Q_1$ crossing to $^3Q_0^+$ and also via direct dissociation on $^1Q_1$) should remain fairly similar to that observed at 193 nm.[83] i.e. the branching ratio at 235 nm should be comparable with that at 193 nm, with the only difference being a reduction in the absolute populations of both states due to reduced excitation to the $^1Q_1$ and $^3Q_0^+$ levels.

However, at 235 nm, the value of [Cl*]/[Cl] is not similar to that at 193 nm, but is markedly lower. Such a reduction cannot be reasonably explained without considering the $^3Q_1$ state. At longer wavelengths, $^3Q_1$ becomes increasingly accessible, and it correlates only with ground state Cl products whose angular distribution should point to their being produced via a perpendicular excitation. Therefore, if this state is involved in dissociation at longer wavelengths, the results should differ from those at 193 nm in two ways. Firstly, a reduced branching ratio should be observed due to the increased excitation to $^3Q_1$ and decreased excitation to $^1Q_1$ (and therefore $^3Q_0^+$). i.e. at longer wavelengths

Cl is produced via $^3Q_1$ at the expense of Cl* produced via $^1Q_1$ crossing to $^3Q_0{}^+$. Secondly, of the ground state Cl fragments produced, there will be a reduction in those whose angular distribution indicate a parallel transition (i.e. fewer Cl produced via $^3Q_0{}^+$ crossing to $^1Q_1$) and a concomitant increase of Cl fragments with angular distributions indicative of a perpendicular transition (i.e. more Cl produced via direct dissociation on $^3Q_1$). The result of this will be a β parameter, at decreased photon energies, which is more perpendicular in character.

As the dissociation wavelength is increased, there is a reduction in the [Cl*]/[Cl] branching ratio, and the β parameter for the Cl fragments changes from 0 (an isotropic distribution) to 0.2 (i.e. increased perpendicular character of the angular distribution). These results confirm the role of the $^3Q_1$ state in the near threshold dissociation of chloroform via the Q band.

A summary of the reaction pathways is provided in Table 4.2.

Product Fragment	**Reaction Pathway**	β **(predicted)**	**Proportion (at 193 nm)**
Cl*	$^1Q_1$ **crossing to** $^3Q_0{}^+$	$\sim\frac{1}{3}$	**~50 %**
Cl	$^3Q_0{}^+$ **crossing to** $^1Q_1$	$\sim -\frac{2}{3}$	**~25 %**
Cl	**Direct on** $^1Q_1$	$\sim\frac{1}{3}$	**~0 - ~25 %**
Cl	**Direct on** $^3Q_1$	$\sim\frac{1}{3}$	**~0 - ~25 %**

Table 4.2: $CHCl_3$ Reaction Pathways

4.5 Conclusion

The newly-constructed VMI apparatus was calibrated for velocity measurements and branching ratio measurements of Cl*/Cl using the well known one-photon dissociation of Cl_2. Subsequently, the one-photon dissociation of chloroform, $CHCl_3$, via excitation to the lowest lying excited electronic states, the "Q Band", was studied using photon wavelengths of 193 nm and 235 nm. Kinetic energy distributions, β parameters and branching ratios were calculated at both wavelengths for the ground state ($^2P_{3/2}$) and spin-orbit excited state ($^2P_{1/2}$) atomic chlorine photofragments.

The kinetic energies of the chlorine fragments were determined to be 0.94 eV and 0.65 eV for dissociation at 193 nm and 235 nm respectively. The ground state and excitated fragments were found to have a kinetic energy difference of $\sim$0.08 eV in both cases, consistent with the energy difference between ground state and spin-orbit excited state Cl atoms. Branching ratios of 1 and 0.3 were obtained for 193 nm and 235 nm dissociation respectively, and beta parameters for both product quantum states at both dissociation wavelengths were determined.

From the results, several features were apparent. The $^3Q_1$ state has been shown to be increasingly involved in the dissociation at longer wavelengths: at 235 nm the pathway involving excitation to this state accounts for half of the products. The measurement of these branching ratios, and of the β parameters, allowed a tentative quantitative assignment of the proportion of Cl products resulting from a number of reaction pathways, of which four were identified.

Certain of these results agreed with previously reported values, of kinetic energies for example, and not with others, thus helping to clarify the dissociation mechanisms of chloroform, which have previously been contested as a result of a difference in reported values. Most striking is the elucidation of significant involvement of the $^3Q_1$ surface, in contrast to previous studies which

assumed minimal or no involvement of this state.

Chapter 5

Surface VMI

5.1 From Gases to Surfaces - Validating VMI Over Larger Areas

5.1.1 Surface VMI

Since it was introduced in 1997, the vast majority of VMI studies have focussed on gas phase systems. Gas phase photodissociations are ideal candidates for VMI studies due to the fact that VMI measures the velocities of fragments along the two dimensions parallel to the detector. The angular distributions of photofragments from gas phase photodissociations (induced by linearly polarised light) possess cylindrical symmetry about the electric field polarisation vector of the dissociating photons. As a result, the full three dimensional velocity distribution can be determined by measuring the velocity components along the dimension defined by the photon's electric field vector, and along one of the other two dimensions. In addition, the region of space in which fragments can be detected under VMI focussing conditions, while small, is large enough to reliably detect gaseous photodissociation products, as they are all produced and ionised within the relatively small confines of the intersection of the laser and the molecular beam.

Over the last few years, there has been a move towards adapting the VMI technique to enable the study of surfaces. The first surface VMI study reported by Wodtke and co-workers studied the laser desorption of Br atoms from a KBr crystal.[38] More recently, the Nesbitt group have investigated scattering from surfaces, including the scattering of a molecular beam containing HCl from a self assembled monolayer from which they obtained the kinetic energies of the scattered particles along the two axes parallel to the surface.[91] Other groups have constructed (or are constructing) surface VMI spectrometers. The White group use a VMI surface apparatus to study degradation on TiO_2 surfaces, and the Vallance group are developing a "spatial map imaging" technique to

study biological molecules at surfaces.[92,93]

Prior to the development of VMI, various groups had carried out imaging studies (essentially using the PFI technique) in order to determine the velocity distributions of various surface processes. Jacobs and co-workers developed an MCP/phosphor screen/CCD detection system adapted to study scattering from surfaces. Their first report of the detector involved characterising the TOF distribution of an ion beam containing NO^+.[94] Mull *et al.* used a similar apparatus to study NO fragments desorbed from oxide surfaces by UV light, and Winograd and co-workers carried out experiments to detect the velocity distributions of Rh ions ablated from an Rh surface, and alkali metals desorbed from RbI and KI single crystals using He^+ and Ar^+ ion bombardment.[39,95,96]

In a gas phase photodissociation, due to the cylindrical symmetry of the photofragments' angular distribution, the full three dimensional distribution can be obtained by detecting the velocity components in just in two dimensions: along the axis parallel to the electric field of the photon (the Y axis, or the axis of cylindrical symmetry), and along either of the X or Z axes. As a result, VMI can be used to obtain the full three dimensional velocity distribution of the fragments, which is extracted from the two dimensional projection of the velocities in the two dimensions (X and Y axes) parallel to the detector. For a surface reaction, however, in order to obtain the full three dimensional velocity distribution, all three velocity components must be measured individually (see Fig. 5.1).

In a surface VMI experiment, the two velocity components parallel to the surface (along the X and Y axes) are obtained directly from the VMI image. Because VMI detects the velocity components only in the plane parallel to the detector, the third velocity component in a surface experiment, that along the surface normal (Z axis), cannot be obtained from a single VMI image. In order to obtain the full three dimensional velocity distribution of fragments desorbed from a surface, the Z axis velocity must be obtained separately.

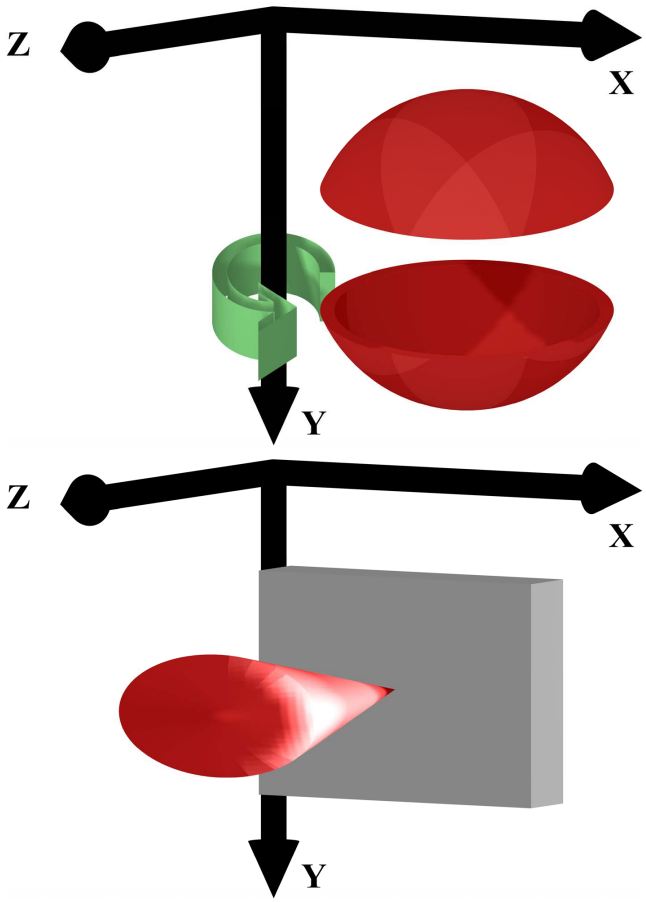

Figure 5.1: In gas phase dissociations the photofragments' angular distribution possesses cylindrical symmetry about the polarisation of the electric field of the photon (the Y axis here). Surface desorptions can possess three distinct velocity components, all of which must be determined separately.

This velocity component can be obtained using time of flight methods. One method is to focus the probe laser at a known distance above the surface. The time taken for the fragments to fly from the surface to the focus of the ionisation laser is measured by recording the intensity of the signal produced by the fragments at different time delays between dissociation and ionisation. Knowing the distance and the time taken, the average velocity of the fragments in this dimension (i.e. the velocity of fragments which produce maximum intensity in the TOF trace) can be calculated. A similar time of flight method which makes use of imaging may also be used. Multiple VMI images could be obtained by varying the time at which ionisation of the fragments take place. This would produce a series of images detecting fragments travelling with dif-

ferent velocities along the Z axis: the fastest fragments would be imaged with the shortest time delay between dissociation and ionisation. With increasing time delays, slower moving fragments would be progressively detected and imaged. The result would be akin to a stop-motion video showing the fragments passing through a plane above the surface at any given time after dissociation.

It is important to realise that, for either the "standard" time of flight or the imaging time of flight experiments just described, the accuracy of the detected Z axis velocity component is strongly dependent on the length of the "start time". In other words, if product fragments are produced (either through a molecular beam colliding with the surface, or surface species being desorbed with a laser) during a period of time which is of similar magnitude as the time of flight of the fragments between the surface and the ionisation beam, the Z axis velocity can be detected. However, if the dissociations occur over a time scale much longer than the products' time of flight, the velocity cannot be reliably measured.

For example, in the surface VMI paper by Wodtke and co-workers, the velocity of Br atoms leaving a KBr surface was investigated.[38] It was found that the slowest Br fragments (i.e. those with the longest time of flight) had a velocity of $\sim$500 m s^{-1} along the surface normal, and the time of flight distance was 1.2 mm, hence their time of flight was $\sim$2 μs. In order to reliably measure this TOF, the fragments must be desorbed from the surface over a time scale on the order of microseconds or shorter. If the fragments are desorbed over a longer time scale, it cannot be known for certain when any particular fragment was desorbed, hence the fragments' velocity cannot be determined since their actual time of flight is not known.

To ensure a well defined dissociation event very short pulsed molecular beams could be used. However, achieving molecular beam pulses at the microsecond timescale is difficult. Recently, molecular beam systems with short pulses have been developed, but even these very short beams have a length of

$\sim$20 μs.[97,98] Therefore, VMI studies which investigate bimolecular processes at surfaces using molecular beams with pulse lengths on the order of hundreds of microseconds, such as that published by Nesbitt and co-workers, are limited in that they can only determine the velocity components in two dimensions.

Unimolecular reactions, however, can be induced using laser pulses with much shorter temporal bandwidths. The gas phase experiments described here involve dissociating molecules using either a YAG-pumped dye laser system with a bandwidth of $\sim$7 ns, or an excimer laser with a bandwidth tens of nanoseconds long. This represents a well-defined dissociation event, which, if applied to surfaces, will allow accurate recording of the aforementioned Z axis TOF profiles. At present, therefore, only by coupling VMI with TOF measurements (either standard TOF or by time resolved imaging as described above), and by initiating the surface reaction using lasers, can the full three dimensional velocity distribution of fragments from surface reactions be obtained.

5.1.2 Laser Geometries for Surface Studies

Because the fragments which are desorbed from the surface travel at a range of angles with respect to the surface normal, the goal is to configure the lasers such that fragments travelling at different angles are all detected, and that fragments travelling at a particular angle are not preferentially detected over others. When carrying out laser induced desorption studies on surfaces there are several options for laser geometry to achieve detection which is representative of the fragments' entire velocity distribution.

The laser geometry most commonly used for two colour gas phase experiments is termed "dot-dot." Both the dissociation and ionisation laser beams are focussed to small dots using spherical lenses. This geometry cannot be used for surface studies. If a "dot" dissociation laser is used, the fragments are created at a well defined point on the surface, and then fly off over a range of

angles. A "dot" ionisation laser focussed above the surface will therefore ionise only a small subset of these particles: those travelling along the line connecting the foci of the two lasers. The fragments flying at other angles will not be ionised and therefore will not be detected. This geometry could in principle be used, provided the ionisation beam is swept along an axis parallel to the surface, so that by ionising fragments at different positions, all fragments will ultimately be detected. However, this entails an increase in experimental complexity and potential sources of error due to the need to move the ionisation laser beam.

Extending this idea, one arrives at the "dot-sheet" geometry. In this case, the ionisation beam is focussed with a cylindrical lens to form a sheet which runs parallel to the surface. By ionising all fragments passing through this sheet, there is no need to move the laser beam in space, and this geometry ensures that fragments travelling at a range of angles will be detected. This geometry will, in the future, be employed for surface desorption studies carried out on the apparatus which is described here.

Alternatively, the fragments may be desorbed from a large area of the surface using a broad, unfocussed beam and then ionised using a spherically focussed beam (the "sheet-dot geometry" as used by the Wodtke group in their KBr experiment).[38] Using sheet-dot or dot-sheet geometry should yield the same results, although the dot-sheet geometry is more intuitive. Fig. 5.2 shows a representation of these two cases.

For surface desorption studies, either optical configuration is efficacious. However, for a bimolecular (scattering) reaction at a surface, a "dot" ionisation beam is ineffective. In such a case, the scattered fragments do not necessarily possess symmetry about the surface normal. As a result, ionising the fragments using a dot beam will provide incomplete results. In such cases it is essential to ionise fragments over a large area. This experimental consideration is true of purely gaseous bimolecular studies using crossed molecular beams, as well

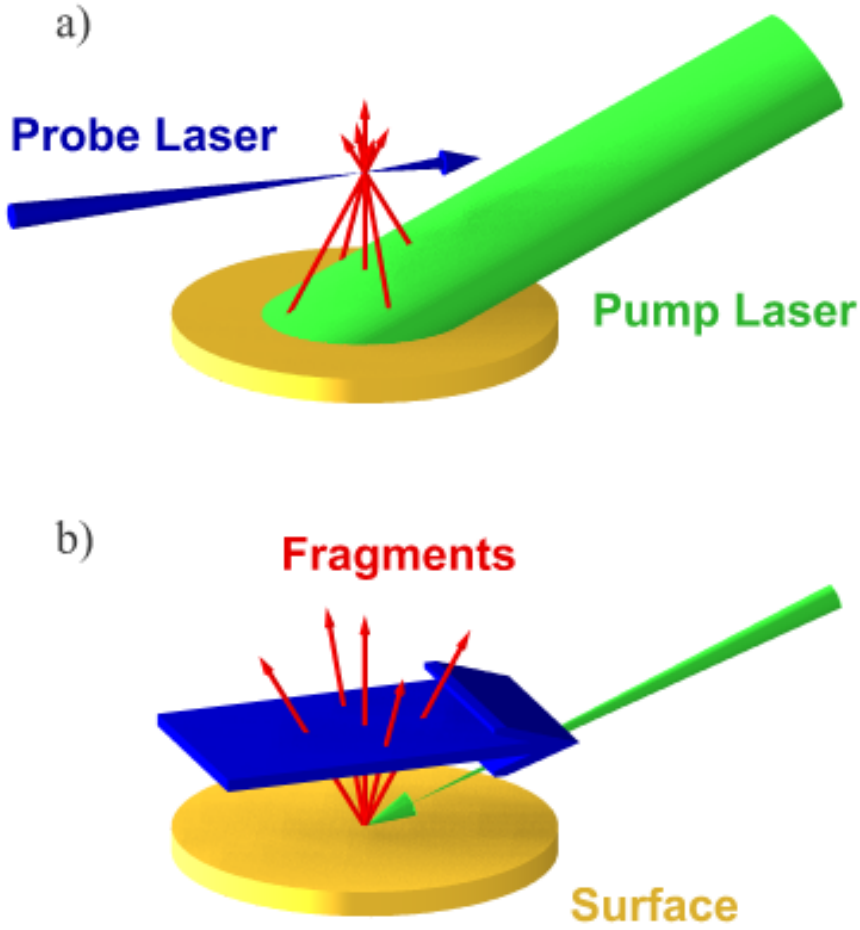

Figure 5.2: Representations of a) sheet-dot and b) dot-sheet surface optical geometries.

as when directing a molecular beam at a surface. In both cases, product fragments are scattered into a large area and, also, the angles into which the products are scattered is not usually known beforehand. As a result, the ionisation beam must cover a large area of space in order to ensure all scattered fragments are ionised and thus detected. In practice this involves focussing the ionisation beam with a cylindrical lens to form a sheet beam, or else using a dot beam which is swept over the area to be probed. The sheet-dot geometry (without sweeping the ionisation beam in space) works only for unimolecular surface reactions because of the fact that, for a surface desorption, the angular distribution of fragments possesses two mirror symmetry axes along the two dimensions which are detected using VMI.

The fact that the dot-sheet geometry is more intuitive is one reason to use it. The other reason is that it is the only option when studying scattering from surfaces, as explained above. While the current work describes preparation for surface desorption studies only, by employing the dot-sheet geometry at this stage (and carrying out the characterisation which is necessary due to the reasons explained in the following section), the option to study scattering at a future date is available.

5.1.3 The VMI Area

When describing surface dynamics reactions, the direction of travel of the fragments can be described by a spherical coordinate system. Here, the polar angle (θ) is the angle at which the fragments travel relative to the surface normal (Z axis), and the azimuthal angle (ϕ) is the angle at which they travel relative to the vertical (Y) axis. When probing fragments from surfaces, it is desirable to detect fragments travelling with ϕ from 0 to $\pm 180^{o}$ and with θ from 0^{o} to ideally $\pm 90^{o}$. Experimentally, fragments travelling at all values of ϕ for a given value of θ can be detected using surface VMI. However, the range of θ values which can be detected is dependent upon the size of the ionisation laser sheet, and its distance from the surface. While detecting fragments travelling at angles of $\pm 90^{o}$ is the ideal, in practice one must settle for detection over a lower range of angles than this. Fragments detected with θ from 0^{o} to $\pm 45^{o}$ represent a reasonable subsection of the products, though of course the higher the solid angle which can be subtended by the ionisation sheet, the better.

In order to detect over the range $\theta = 45^{o}$ to $\theta = -45^{o}$, the probe laser sheet needs to cover an area which is twice as wide as the distance between the surface and the sheet. In addition, since TOF profiles are most accurately produced when the distance between the surface and the probe laser is as large as possible, there is a necessary trade off between moving as far as possible from the surface to obtain good TOF profiles, and maintaining the probe sheet

close to the surface in order to minimise the required size of the probe sheet. A distance of 5 mm between the probe beam and the surface represents a reasonable compromise, as it is a large enough distance to obtain good TOF profiles. A laser sheet of 10 mm wide is thus needed.

The sheet beam is obtained by expanding the pump laser beam in two dimensions using a spherical concave lens until it is of the desired width, and then using a spherical convex lens to stop the divergence. This wide beam is then focussed in one dimension using a cylindrical convex lens to form the laser sheet.

Having established an optical geometry for obtaining both TOF profiles and VMI images, one significant problem is apparent. It has already been mentioned that the elegance of VMI lies in the fact that VMI focussing conditions create a region of space (the "VMI area") and that fragments which are ionised within this VMI area will be mapped to a point on the detector which is dependent only on their velocity and which is independent of their initial position; thus resolving the problem of low resolution inherent in images as a result of uncertainty in the fragments' "birthplaces". However, using a standard, three electrode VMI apparatus, this VMI area is typically on the order of one to two mm wide. This is more than sufficient for gas phase photodissociation studies, in which all fragments are ionised in a region defined by the intersection of the probe laser with the molecular beam, which is typically less than two mm wide. When attempting to produce images from fragments which are produced by surface scattering or crossed molecular beam studies, or in surface desorption studies using a dot-sheet geometry, the fragments are ionised over a much larger area: a 10 mm wide area in the case of the work planned here.

All fragments ionised outside the VMI area will be mapped to the detector, but not under VMI conditions, which will result in loss of resolution and images of lower quality than those which would be produced if all fragments were

mapped under perfect VMI conditions. It is therefore necessary to increase the VMI area to a size which is commensurate with the desired dimensions of the probe laser sheet.

5.1.4 Weak Extraction

When the various gas phase slicing techniques were discussed earlier, the non-optical dc-slicing method was described. This involves using additional electrodes to allow lower voltages to be applied to them, which allows the NS to expand along the Z axis, while still maintaining a tight focussing of it along the X and Y axes. Soon after the introduction of dc-slicing, an additional benefit was discovered. By using more electrodes, the potential gradient across successive electrodes is decreased. This results in what is called "weak extraction". The more electrodes used, the weaker the extraction conditions which are set up. As the "strength" of the extraction decreases, the size of the VMI area increases. Because of this, the groups of Kopin Liu and Xueming Yang have constructed VMI spectrometers containing twenty nine and thirty one electrodes respectively, which they use for studying crossed molecular beam systems.[35,36]

As a VMI area of 10 mm wide is required for the planned surface desorption studies here, a key part of the work involved designing the electrode system such that the intricacy of a thirty electrode stack was avoided, while increasing the VMI area beyond that obtained using a three electrode stack. A design consisting of twelve electrodes, already described in section 3.5, was chosen.

5.1.5 Characterising the VMI Area

While using many electrodes is an established method for increasing the VMI area, the increase in the area has not been investigated. Yang's group reported a usable VMI area 25 mm wide when using thirty one electrodes. The dimensions of their VMI area were inferred quite simply by ionising fragments

over this length and reporting no visible loss of resolution. In the case of surface desorption studies, it was felt necessary to characterise of the VMI area produced by the twelve electrodes, before further adapting the apparatus for surface studies.

The characterisation involved carrying out simulations with the goal of determining whether using additional electrodes could provide VMI conditions over a larger area when compared with a three electrode apparatus, and then to experimentally determine the size of the VMI region produced by the additional electrodes.

5.2 The VMI Area - Simulations

5.2.1 SIMION®

SIMION® is a software package used for setting up a computational model of an apparatus, calculating the electric fields which the apparatus produces, and then determining the trajectories of charged particles moving through the fields.[99,100]

In SIMION®, a two dimensional array of points corresponding to the XZ plane was defined and the array was then defined as having cylindrical symmetry (about the Z axis). Each point was initialised to 0 V. The array points corresponding to electrodes were then defined. The array was refined (the program solves the Laplace equation for each point in the array: essentially the electrostatic potential is defined algebraically for each array point in terms of its proximity to the user-defined electrodes). Each defined electrode can be assigned a voltage, user-defined particles (defined by position, kinetic energy, mass and charge) can be produced and their trajectories through the array can be visualised.

5.2.2 VMI Area Simulations

A comparison of the achievable resolution between a three electrode and a twelve electrode configuration was investigated. Identical arrays were created for each case, the only difference being the number of electrodes present. An identical set of particles was used for each simulation. These were defined to mimic NO fragments from NO_2 photodissociation at ~226 nm (see section 5.3). Five particles were produced below the axis and five above it. For the three electrode simulation the particles were produced ±1 mm from the horizontal axis; for the twelve electrode simulation they were produced ±7.5 mm from the horizontal.

In each of the sets of particles (above and below the axis), one particle had

initial velocity vertically upwards, one vertically downwards, one horizontally along the TOF tube, and one particle each with velocity $\pm 45^{o}$ to the horizontal axis. Fig. 5.3 shows the initial trajectories of the particles, the black arrows showing the initial velocities of particles above the axis, and the red arrows those below it. The particles in each set (above and below) are numbered; particles with the same number have identical initial velocities. The arrival positions of the particles at the detector under VMI focussing conditions is also shown. Particles with the same initial velocities arrive at the same position on the detector, regardless of whether they were produced above or below the TOF axis.

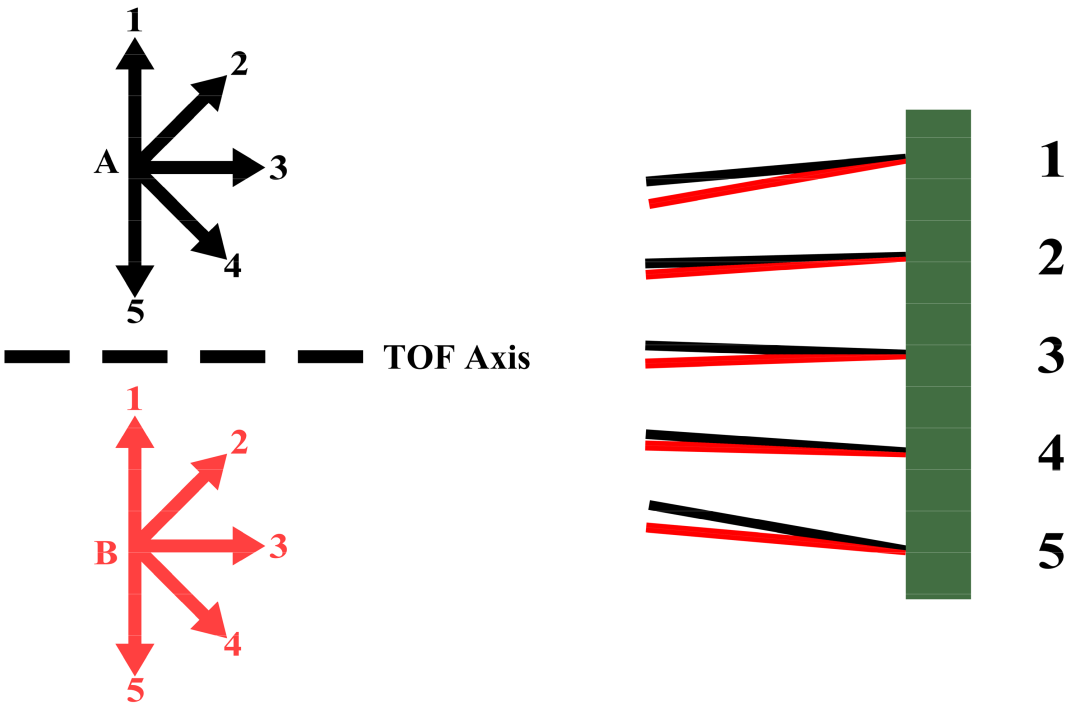

Figure 5.3: The initial velocities of the particles in the SIMION® simulations. Also shown are the arrival positions of each pair of particles (under VMI conditions) at the detector (side view).

For the twelve electrode simulation, the particles were "flown" through the electric fields with the repeller electrode biased at 1000 V. The three electrode

simulation required a higher repeller voltage (1500 V) due to the fact that, with only three electrodes, the ions spread too far parallel to the detector, and so miss it. The higher voltage decreases the time taken for them to arrive at the detector, and hence also reduces their spread parallel to it.

5.3 The VMI Area - Experimental Validation

In order to ensure that the full three dimensional velocity distribution can be determined for the fragments desorbed from surfaces, it is necessary to ionise them with a sheet at least 10 mm wide, focussed 5 mm above the surface. In order to ensure that the full power of VMI is exploited, the VMI conditions must remain valid over at least this 10 mm wide area. Simulations can be carried out to investigate, at least qualitatively, whether an experimental configuration using more than three electrodes provides VMI conditions over larger areas than a configuration with three electrodes. It is, however, essential to ensure that this apparatus can provide VMI conditions over at least 10 mm. This must be determined by experiment.

To validate the spatial extent of the VMI focussing conditions, photofragment products were created at varying distances from the central TOF (Z) axis. The products were produced at different positions along the Y axis in order to determine the distance from the Z axis at which the VMI conditions break down. Due to the cylindrical symmetry of the electrode stack about the TOF axis, this distance is the same for both X and Y axes. The fragments produced at each different position were imaged, and the images compared.

The dimensions of the VMI area can be determined from the images, since images from fragments created within the VMI area should be identical. Specifically, it is necessary to define what characteristics of the image must remain consistent throughout the entire VMI region. There are three key properties. Firstly, the radius of the rings (i.e. the kinetic energy obtained from each image) must not differ from one position to the next. Secondly, the resolution of the images (the thickness of the rings, or the FWHM of the velocity distribution peaks) must not differ either. Finally, the absolute position of the images must be the same for images taken at all positions. The limit of the VMI area can be defined as the distance from the centre, beyond which, detecting photofragments results in images which demonstrate a reduction in resolution,

a change in image radius, or a change in image position.

5.3.1 Apparatus

In order to confirm the size of the VMI area produced using twelve electrodes, the repeller electrode was slightly modified. It was necessary that reactant molecules in the molecular beam could be dissociated and ionised at various positions away from the central TOF axis. The modified experimental setup is shown in Fig. 5.4

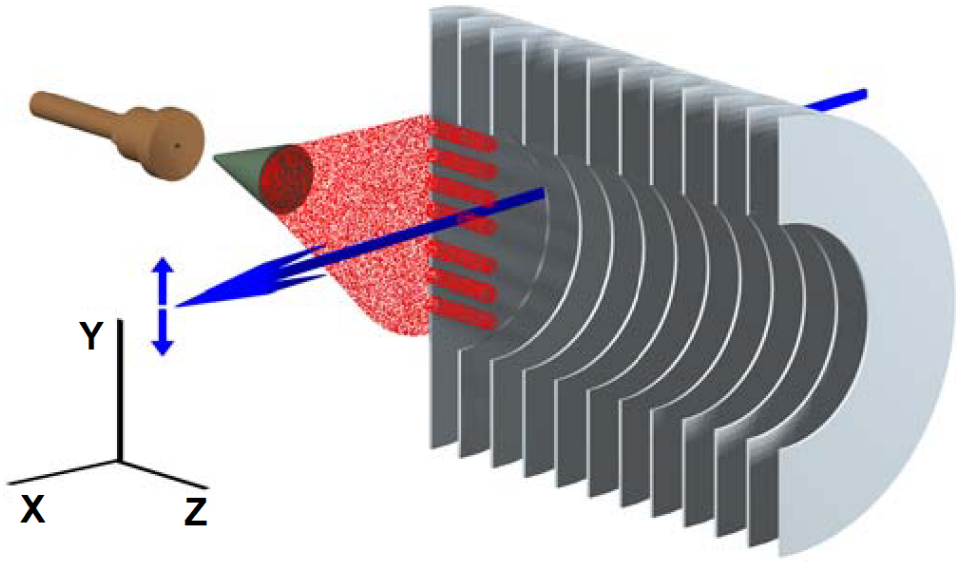

Figure 5.4: The experimental setup for the validation of the VMI area. A repeller electrode containing multiple holes allows the molecular beam to enter the interaction region at various distances from the centre. The laser beam can be moved vertically to selectively intersect one molecular beam at a time.

The standard repeller electrode was replaced with a modified electrode containing 1.5 mm diameter holes along the vertical (Y) axis at 1, 3, 5 and 7 mm above the TOF axis and 2, 4 and 6 mm below it. Because the molecular beam and skimmer were mounted ∼25 cm behind the repeller, the beam had expanded sufficiently upon reaching the electrode that each of the repeller holes was able to accept the beam. The result was that within the interaction region (between electrodes one and two) seven separate molecular beams were present

at varying distances from the central TOF axis. The laser beam entered the chamber via mirrors and lenses mounted on a vertical translation stage which allowed the laser beam to be moved in the vertical direction.

5.3.2 Experimental

The well known NO_2 photodissociation at ∼225 nm was used to characterise the VMI area. This was due to the increased simplicity of a one-colour experiment, the good quality of the NO image (Fig. 5.5) and the ease of detection of the slow moving NO fragments produced.

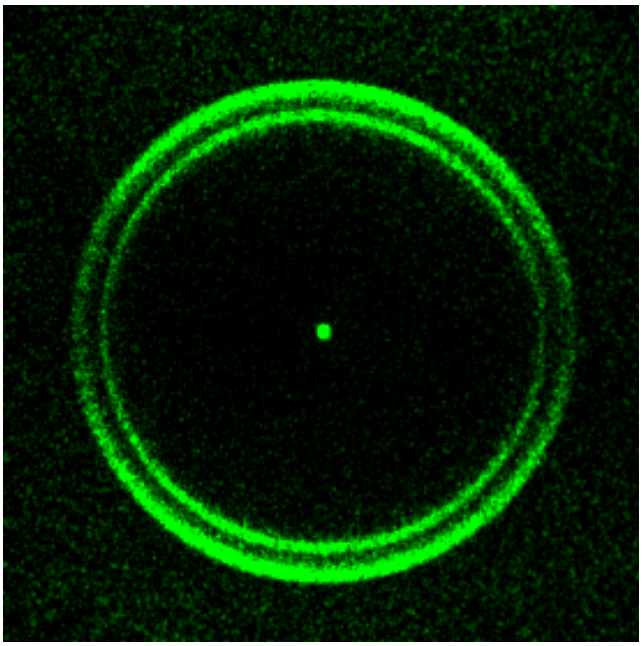

Figure 5.5: VMI image of NO fragments from NO_2 dissociation at ∼225 nm.

A molecular beam consisting of ∼2 % NO_2 and ∼2 % O_2 seeded in He was produced using the apparatus described in section 3.3. The third harmonic of an Nd:YAG laser (355 nm) was used to pump a dye laser containing Coumarin 450, producing ∼450 nm light which was doubled using a BBO crystal to produce ∼225 nm photons with a pulse energy of ∼0.5 mJ.

After passing through the modified repeller electrode, one of the seven resulting molecular beams was intersected with the ∼225 nm wavelength laser

beam. The NO_2 molecules were dissociated to form NO + O, after which the NO ($^2\Pi_\Omega$) fragments were ionised by the same laser beam, using a 1+1 REMPI scheme via the (0,0) X $\leftarrow$ A band (as shown in Fig. 5.6), and were subsequently imaged. VMI images were produced for each of the seven molecular beams, and the experiment was then repeated once more for each molecular beam.

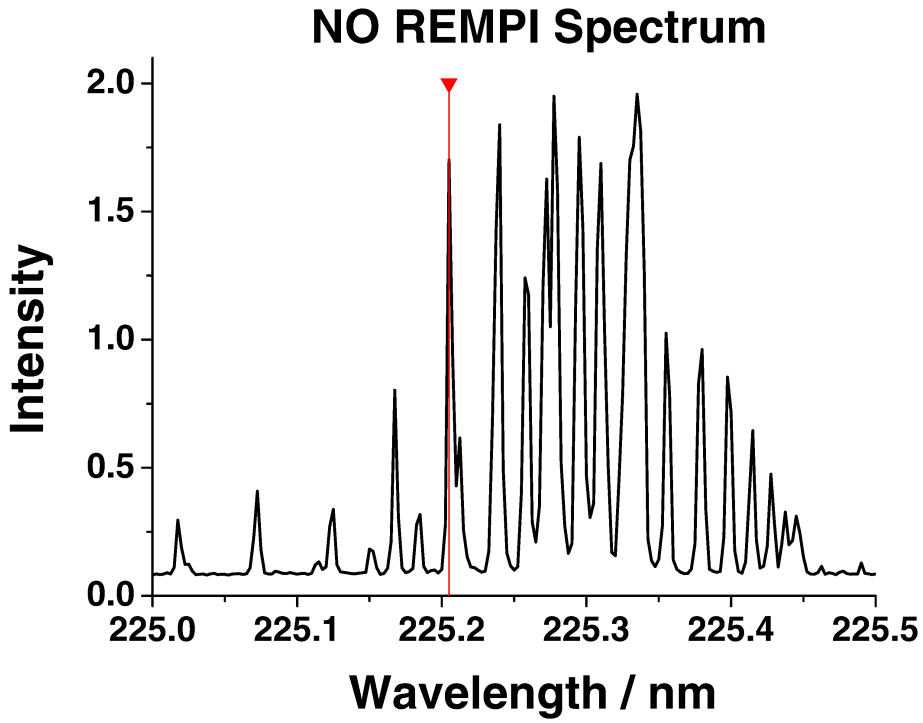

Figure 5.6: REMPI spectrum of NO. The red line indicates which absorption line in the spectrum was probed in order to obtain the image in Fig. 5.5.

5.4 Results and Discussion

5.4.1 Simulation Results

The results from the simulations comparing twelve with three electrode systems are shown in Fig. 5.7. A side-view of the SIMION® array used to approximate the reaction chamber is shown in a), with the twelve electrodes on the left and the MCP detector (surrounded by a green box) on the right. The black and red lines correspond to the trajectories of NO particles with ∼0.1 eV kinetic energy produced above and below the centre axis respectively. Images b) and c) are close ups of the detector showing the arrival positions of the particles with initial horizontal velocity (blue box) and with initial velocity vertically downwards (orange box) using three electrodes. Image d) is as for b) and c) but for a twelve electrode simulation. The green boxes are a side view of the MCP detector, showing the arrival positions of each of the five pairs of particles, each of the pair having the same initial velocity. The blue and orange boxes show a close up of the arrival position of the particles travelling horizontally (particle pair 3 in Fig. 5.3) and those travelling vertically downwards (particle pair 5 in Fig. 5.3) respectively.

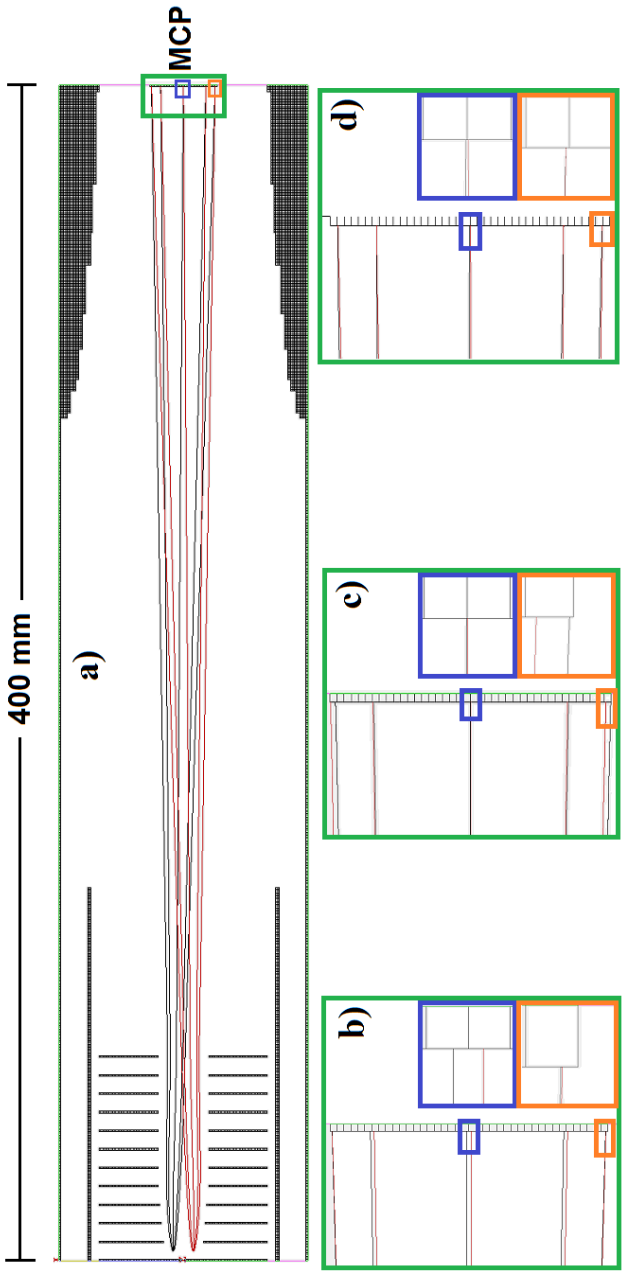

Figure 5.7: Image a) - The results from SIMION® simulations, shown as a side-view of the "chamber". The black lines represent the trajectories of each of a set of five particles created above the centre axis with one travelling upwards, one downwards, one forwards and one each at $\pm 25^{o}$. The red lines show the same, but for particles produced below the axis. Images b) and c) - Close-ups of the detector (green box) and of the arrival of particles at the detector when only three electrodes are used. The arrival positions shown correspond to particles travelling vertically downwards initially (orange box) and those travelling horizontally (blue box). In each case two particles are shown arriving: one which was created above the axis (black line) and one below it (red line). Image d) - As for images b and c) but using twelve electrodes.

5.4.2 Experimental Results

Fig. 5.8 shows the top left quadrants of images of NO fragments taken from each of the seven molecular beam positions, along with the speed distribution of the NO fragments showing the peaks corresponding to the two rings in the NO image.

Fig. 5.9 shows the relationship between the distance from the central horizontal axis of the electrodes, and the three features of the images which were chosen for analysis: a) the image position; b) the radius of the rings; c) the resolution of the images.

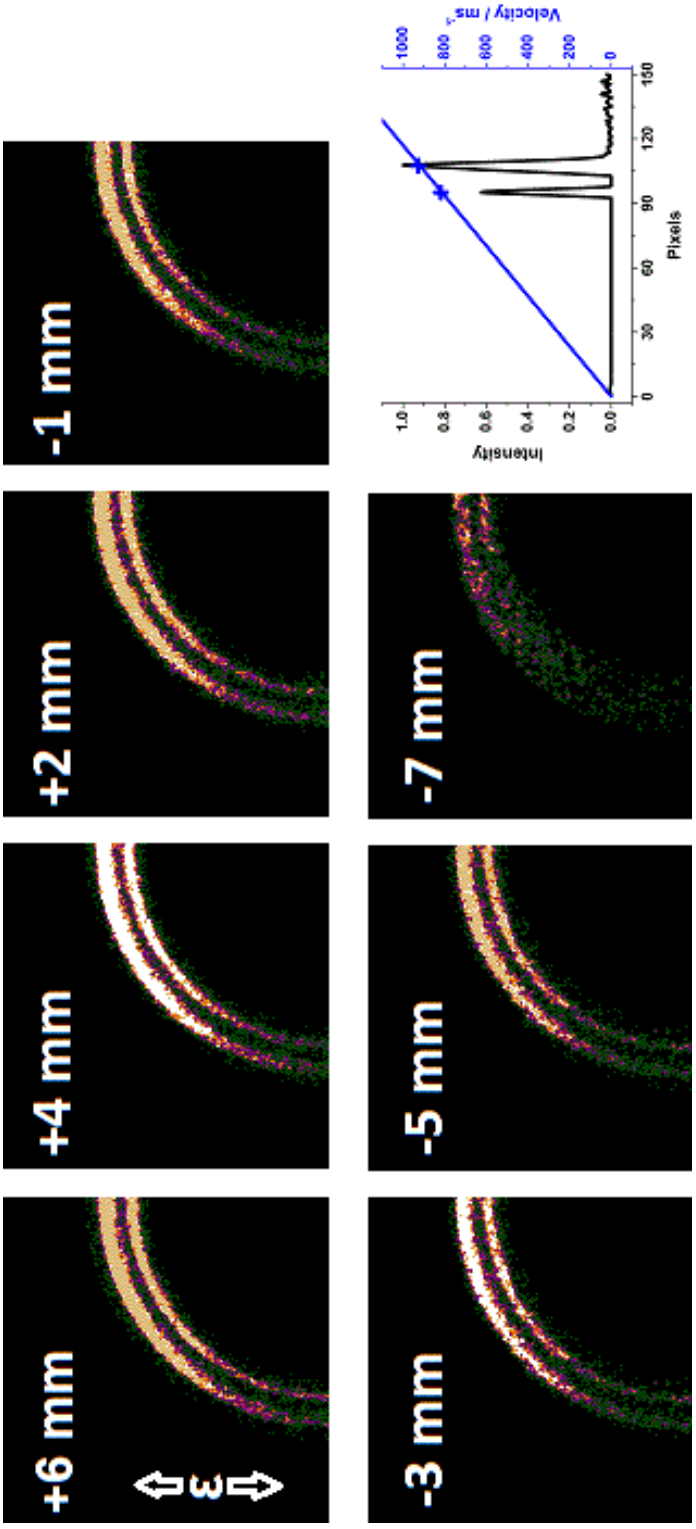

Figure 5.8: Close up of the upper left quadrant of NO fragments from NO_2 dissociation at ∼225 nm at different distances from the central TOF axis and the velocity distribution showing the peaks corresponding to the two rings in the images.

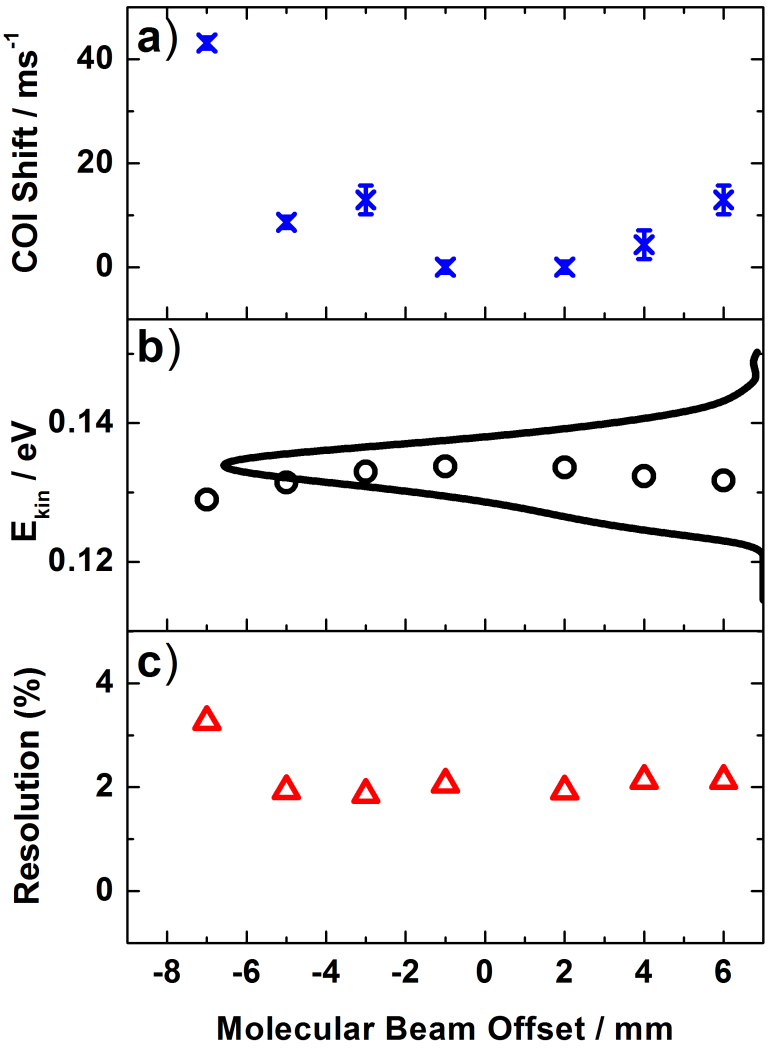

Figure 5.9: a) The absolute position of the Centre of Inversion of each image. b) The maximum kinetic energy derived from each image for the outer ring in Fig 5.5, also showing the full kinetic energy distribution peak for this ring on the right side Y axis (extracted from the NO image obtained at 1 mm off the central TOF axis). c) The resolution of the images (FWHM of the peaks in the velocity distribution obtained therefrom divided by the radius of the detector).

5.4.3 Discussion

Three vs Twelve Electrodes, Increased VMI Area

In Fig. 5.7, several features are apparent. By comparing the arrival positions of the fragments in the blue and orange squares in b) and c) it can be seen that when using three electrodes there is a trade in resolution between fragments with a large velocity component along the vertical axis, and those with no velocity (or low velocity) along the vertical. Either set of particles can be imaged with good resolution, but not at the same time. The voltages on the electrodes required to image fragments with large vertical velocity components, b), must be changed to image fragments with low vertical velocity components, c). This problem is negated with the use of twelve electrodes: all velocity components are mapped with comparable resolution at the same time.

It is evident that the resolution achievable with three electrodes can vary from poor to good (from $\sim$2 % to $\sim$8 % determined from the simulations) and that the best resolution across all velocities in any single experiment will be somewhere between the two, while for twelve electrodes the resolution is consistently good at $<$2 % for all fragments. Slicing can aid in resolving this problem for a three electrode system, since by detecting only the centre slice of the NS, fragments with velocity components along the vertical are preferentially detected over those with velocity components along the horizontal. Optical slicing is only applicable to reactions which produce neutral fragments however. Therefore, when studying reactions which produce ionic fragments, only pulsed field or dc-slicing can provide the best possible resolution.

In addition, and more important for this work, the use of multiple electrodes results in the VMI focussing conditions extending over a larger area. It should be emphasised that in the twelve electrode simulation above, the particles were created 15 mm apart, while in the three electrode simulation they were only 2 mm apart. The reason for comparing particles 2 mm apart

with particles 15 mm apart using three and twelve electrodes respectively, is simply to demonstrate the increased VMI area when using twelve vs three electrodes. For reaction dynamics experiments in which fragments are detected over a larger region of space (gas phase or surface scattering studies or surface desorption experiments) this enhanced area is essential to obtain a true VMI image.

Defining VMI

With twelve electrodes the VMI area is shown to be ∼15 mm wide in simulations. This is larger than the 10 mm required here, and therefore gives a good indication that a twelve electrode apparatus should provide an adequately large VMI area. The actual size of the VMI area has been experimentally verified, from the results shown in Figs. 5.8 and 5.9. An initial visual inspection confirms that the images are of consistent quality up to 6 mm above and at least 5 mm below the central axis. By 7 mm off axis, the VMI conditions have clearly broken down and the image is of poor quality. To analyse the images more quantitatively, three characteristics were chosen: the position of the images; the kinetic energy obtained for the fragments, and the resolution of the images. The consistency of each of these features in the images (or lack of) confirms the presence (or absence) of VMI focussing conditions. Fig. 5.9 displays results showing that using a twelve electrode system produces VMI conditions to ∼6 mm either side of the central TOF axis. The position of the rings (a), the radius (b) and the resolution (c) of the NO images remain consistent across the 12 mm diameter, and by 7 mm off-centre have deteriorated. This deterioration is most noticeable in the change of the position of the image's centre of inversion (COI) for the image obtained 7 mm off centre.

A VMI image is one which is produced by all fragments being mapped to the same point on the detector, regardless of their initial position, and dependent only upon their initial velocities. In actual fact, fragments are not

mapped to a singularity, rather, a VMI image is one in which the spread of the fragments' arrival positions is minimised. As a result, when comparing the images produced at different positions, the possibility existed that there would be a gradual but constant change in the images' three characteristics as the point at which the fragments were ionised was located increasingly far from the central TOF axis. Therefore, without an absolute quantitative definition of what is and what is not a VMI image, a potential problem was anticipated, namely that a line must be drawn at some arbitrary point for each characteristic in order define what was and what was not a result of VMI focussing conditions.

However, upon analysis of the images, one particularly interesting feature becomes apparent. The VMI area seems quite well defined in space. Fragments with the same velocity which are ionised within the VMI area are mapped to the same position on the detector, producing images whose centres overlap, which have the same radius, and whose rings are equally well resolved. Up to 6 mm away from the central axis, consistent images can be produced. However, moving just 1 mm (at most) further away, the absolute position of the image produced and the resolution of the image both change noticeably. This is an important consideration for experiments which require a larger VMI area.

If the quality (position, radius, resolution) of VMI images changed predictably and constantly with distance from the central axis, then a compromise could be drawn between the dimensions over which the fragments are ionised, and the quality of the image obtained. E.g. If, for every 1 mm off the axis, the resolution of the image produced was reduced by 50 %, and the resolution of an image produced by fragments ionised on the central axis was $\sim$1 %, then the minimum desired resolution could be determined, and the area over which fragments are to be ionised could be defined: 1 % resolution could be obtained on the centre axis only, 2 % by ionising from $\pm$1 mm, 4 % by ionising from $\pm$2 mm and so on.

The reality is that VMI conditions prevail over a certain radius from the central axis. Within this area, all fragments which are ionised will produce a VMI image. This is beneficial, since over some finite distance there is no compromise between the area over which fragments are ionised, and the quality of the images they produce. However, once the ionisation area exceeds the VMI area, an immediate drop in image quality will be realised. Therefore, in order to obtain VMI images over larger areas, the size of this VMI area must be known, and the methods by which it can be increased can then be applied if required.

Increasing the VMI Area

There are several strategies to increase the VMI area beyond that which is produced with a standard three electrode configuration, two of which involve enhancing weak extraction, i.e. reducing the voltage gradient across the electrodes. The first is simply to reduce the voltages on the electrodes as much as possible. e.g. for a three electrode configuration with 1000 V on the repeller and a gradient ratio of 2.33 (see Appendix A.1) the voltage drop between electrodes one and two is $\sim$300 V cm^{-1} and produces a VMI area $\sim$2 mm wide. Using 500 V on the repeller instead, the voltage drop is reduced to 150 V per electrode and a larger VMI area would be produced (although 150 V cm^{-1} is not quite weak extraction and therefore any increase in VMI area would be minimal).

The second method is to use multiple electrodes. Comparing different cases with the same voltage on the repeller electrode is instructive. A standard three electrode configuration typically produces a 1-2 mm wide VMI area and has a potential gradient of $\sim$300 V cm^{-1} between the repeller and extractor electrodes. For the experiments described here using twelve electrodes, 1000 V on the repeller and a gradient ratio of 2.4, the potential gradient over electrodes one to four (the repeller region) is $\sim$50 V cm^{-1} and produces a VMI area

~12 mm wide. Kopin Liu's group reported a VMI area ~25 mm wide using twenty nine electrodes which gave a potential gradient across electrodes in the repeller region of ~21 V cm^{-1}.[35] Thus it can be seen that there is a direct correlation between the number of electrodes used (and hence the potential gradient across the repeller region) and the size of the VMI area. Thus, by using as many electrodes as possible and keeping the voltage on the repeller electrode as low as possible, the maximum VMI area can be produced.

There is one final (potential) method for producing an increased VMI area, which is very simple. The VMI area in our apparatus is ~12 mm wide and is produced by electrodes ~10 cm wide, spaced ~1 cm apart. Additionally, the SIMION® simulations indicated a 15 mm wide VMI area produced by twelve electrodes. However, in the case of the simulations, the scale of the array is relative. The absolute size of the electrodes is not important, rather their relative sizes and spacings are considered. Therefore, for the apparatus here, creating a twelve electrode stack with electrodes ~20 cm wide and spaced ~2 cm apart could feasibly produce a VMI area ~24 mm wide. However, this would entail a larger vacuum chamber and therefore an increased volume to evacuate, which in turn implies increased cost and possibly complexity. Nonetheless, it would seem to be a potential alternative to constructing a thirty electrode stack.

Implications for Surface VMI

With the 12 mm wide VMI area produced using a twelve electrode stack, a 12 mm wide probe laser focussed as a sheet 5 mm above the surface will allow fragments travelling over an angle of ~100° to be detected. This provides more than the minimum 90° required. There are several benefits of having such a large VMI areas with which to work.

By ionising fragments over a larger area, the effect of space charging is lowered. As the ionised fragments are further apart, the blurring associated

with many charged particles being close together is somewhat mitigated.

Assuming a solid angle of ∼100° is sufficient, the point of laser focus can remain in the same position for both imaging and TOF experiments, since a 5 mm TOF distance is sufficient to obtain good Z axis velocity resolution. This allows full three dimensional velocity distributions for surface reaction to be obtained without the need to rearrange the optical geometry.

Additionally, should a solid angle of >100° be needed, an angle of up to ∼152° can be subtended by moving the laser focus to ∼1.5 mm above the surface. This is the distance at which the probe laser was focussed above the surface in the KBr surface desorption VMI experiment mentioned above.[38]

5.5 Other Surface VMI Considerations

Studying the dynamics of surface processes with VMI involves some additional complexity when compared with the gas phase.

For gas phase studies, the pressure inside the chamber must be maintained below 10^{-6} Torr in order to create collisionless conditions (i.e. to ensure nascent products). When studying surfaces the pressure must be significantly lower in order to maintain the cleanliness of the surface on the time scale of a typical experiment. This consideration is not limited to VMI or just reaction dynamics studies, but is a general feature of surface experiments.

Secondly, and specific to surface VMI, the electrode stack must be modified in order to incorporate the surface which is to be studied.

5.5.1 Vacuum for Surfaces

When working with surfaces, it is imperative that the surface remain free of impurities. Between experiments, surfaces can be cleaned by removing any adsorbed impurities by thermally desorbing them, or with the use of an ion gun. However, once clean, the surface must remain so until the experiment is complete. In general, it is desirable that a clean surface not become saturated by surrounding gas phase molecules for a time period of several hours.

In order to achieve this, the number of potential adsorbents (i.e. gas molecules near the surface) must be reduced, which is accomplished by working under ultra-high vacuum (UHV) conditions, typically 10^{-10} Torr or lower.

The reason such low pressures are needed can be illustrated using kinetic gas theory.[101,102] The surface is assumed to possess a number of potential binding sites to which any impinging gas molecule will adsorb upon collision (if a sticking coefficient of unity is assumed, i.e. the "worst case scenario."). By calculating the number of collisions and dividing this by the number of available binding sites, the length of time it takes for the surface to become saturated

with a monolayer of impurities can be calculated for different pressures.

The molecular flux (number of molecules passing through a given area in a given time) can be expressed as:

$$F = \frac{1}{4}nc \tag{5.1}$$

The molecular gas density, n (molecules m^{-3}), is simply derived from the ideal gas equation:

$$n = \frac{p}{kT} \tag{5.2}$$

The mean molecular speed, c ($m\,s^{-1}$), is obtained by integrating the Maxwell-Boltzmann distribution for gas velocities to give:

$$c = \sqrt{\frac{8kT}{m\pi}} \tag{5.3}$$

p is the pressure in Pascals, k is the Boltzmann constant, T is the temperature in Kelvin and m is the molecular mass in kg. By combing equations 5.1, 5.2 and 5.3, the molecular impingement rate (the number of molecules striking a given area in a given time), I, can be derived:

$$I = \frac{p}{\sqrt{(2\pi mkT)}} \tag{5.4}$$

I is in units of molecules m^{-2} s^{-1}. By assuming a temperature of 300 K, a molecular mass of 28 amu (corresponding to N_2 molecules) and 10^{19} binding sites per m^{-2} of surface, I (and hence the time taken for saturation to occur) can be calculated for various pressures. The results of these calculations are shown in Table 5.1.

In order to ensure that a surface remains free of impurities on the timescale of surface experiments, the pressure within the vacuum chamber must be held below 10^{-9} Torr. Using turbomolecular pumps (as described in section 3.2) typ-

Pressure (Torr)	**Impingement Rate (molecules m^{-2} s^{-1})**	**Time to Saturation (seconds)**
760	3×10^{26}	3.3×10^{-8}
1	3.9×10^{23}	2.6×10^{-5}
1×10^{-3}	3.9×10^{20}	1.5×10^{-2}
1×10^{-6}	3.9×10^{17}	15
1×10^{-9}	3.9×10^{-4}	15,000

Table 5.1: Surface Saturation Times at Different Pressures

ically reduces pressure to $\sim10^{-8}$ Torr. In order to achieve the further reduction in pressure required for surfaces, it is necessary to "bake" the chamber. This involves heating the chamber to $\sim200\ ^{o}$C over a period of one to two days, thereby gradually desorbing impurities from the interior chamber walls, and also removing impurities which are embedded within pores in the chamber, such as CO, the presence of which is a result of the welding process used during construction of the chamber. The need to bake the chamber (and the time it takes) represents a major increase in experimental complexity for surface studies.

5.5.2 The Surface VMI Apparatus

In order to carry out surface dynamics studies using VMI, the electrode stack must be modified in order to introduce the surface. The primary modification made to the apparatus involved amending the repeller electrode. The

"standard" electrode contains a 2 mm wide hole in its centre, which accepts the molecular beam travelling along the TOF axis in a unimolecular photodissociation study, such as those on chloroform described earlier. This repeller electrode is modified by increasing the size of the central hole to ∼20 mm.

The surface is then introduced to the electrode stack from behind the repeller. A surface mount was constructed based on a standard design which allows heating and cooling of the surface.[103] A manipulator was mounted onto the top of the main chamber via translation stages, thus allowing linear movement along the horizontal TOF and vertical directions, and rotation about the vertical axis of the manipulator. Horizontal and vertical here refer to the axes in the lab frame. The tube of the manipulator is hollow, allowing liquid nitrogen to be used in order to cool the surface. Therefore, all of the connections between the manipulator tube and the surface have been constructed from thermally conductive materials. Sapphire disks are used between the tube and the "arms", which are copper rods to which copper wires are attached. Sapphire is thermally conductive but electrically insulating, and this ensures that heat can be transferred between the tube and the copper (and hence the surface), and vice versa, while preventing the conduction of electricity from the copper arms back to the tube when a current is applied to the arms. Current is applied in order to heat the tungsten wires which hold the surface onto the manipulator's arms. These wires in turn heat the surface for the purposes of desorbing impurities. The surface itself is a gold, Au(110), single crystal. Finally, wires for a thermocouple are attached to the surface in order to monitor its temperature. The design of the surface mount is shown in Figs. 5.10 and 5.11.

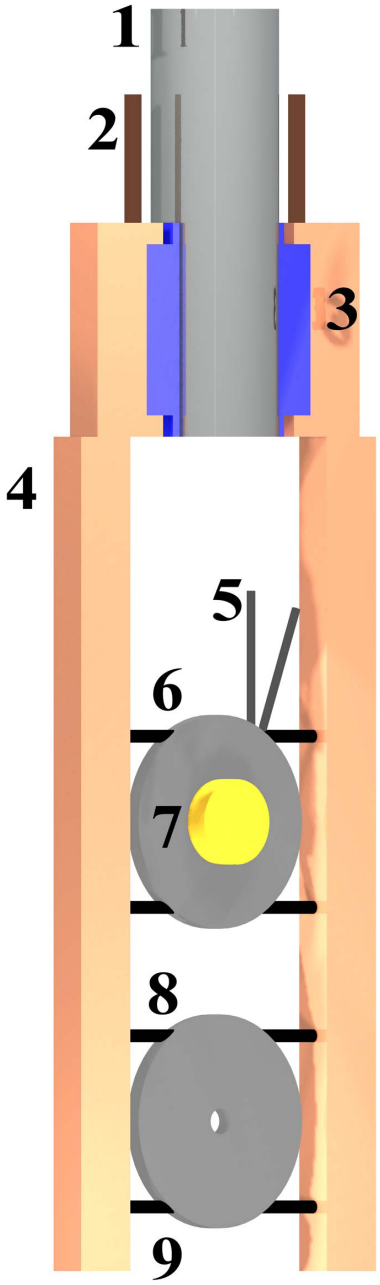

Figure 5.10: 1 - Hollow metal tube which can be filled with liquid nitrogen in order to cool the surface; 2 - Copper wires for resistively heating the surface; 3 - Sapphire discs to electrically insulate (1) while allowing thermal conductivity between (1) and (4); 4 - Copper "arms" to which the surface is attached; 5 - Thermocouple connections; 6 - Metal plate onto which (7) is mounted; 7 - The surface: an Au(110) single crystal; 8 - Tungsten wires used to attach (7) and (9) onto (6); 9 - A metal plate similar to (6) but with a 2 mm hole in its centre.

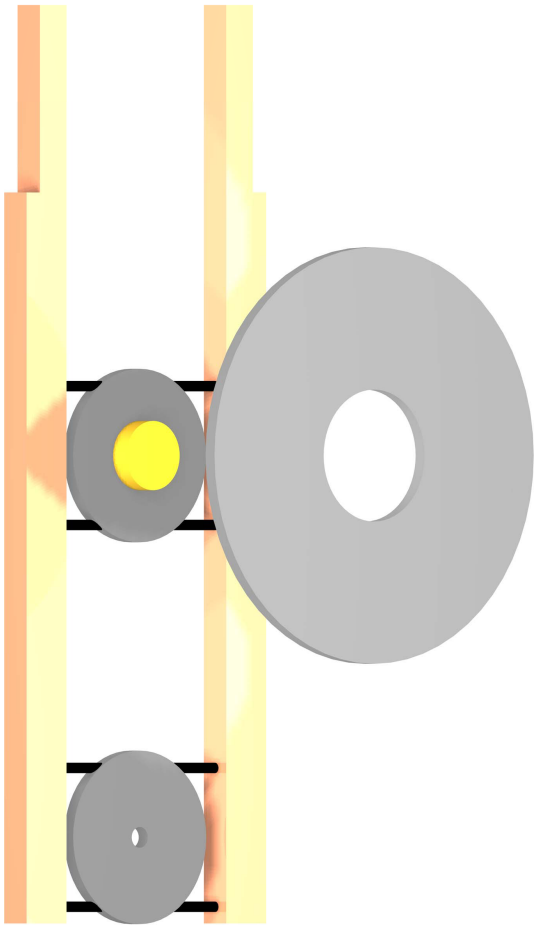

Figure 5.11: Either (6) or (9) from Fig. 5.10 can be introduced to the hole in modified repeller plate, thus allowing either surface studies or gas phase studies (e.g. for VMI image calibration) to be carried out without the need to open the chamber or modify the electrode stack between experiments.

Chapter 6

Conclusion

A typical VMI spectrometer makes use of three electrodes to produce the required VMI focussing conditions, which prevail over an area 1-2 mm in diameter. Such conditions do not suffice for reaction dynamics studies at surfaces, nor for bi-molecular collisional dynamics studies. In both cases product fragments must be detected over a larger region of space than for an archetypal VMI gas phase photodissociation experiment.

To overcome this problem, the area over which the VMI focussing conditions prevail must be increased, and this is known to be possible using "weak extraction" conditions: a moderate reduction in the voltage between successive focussing electrodes. This is achieved by replacing the usual three electrode stack with a stack containing multiple electrodes. Research groups studying crossed molecular beams have created stacks with up to thirty-one electrodes in order to realise sufficiently weak extraction for their purposes. However, no formal or systematic investigation has been carried out to determine the relationship between weak extraction conditions and the VMI area.

The goal of the present work was to construct a VMI spectrometer, capable of weak extraction, to be used for surface desorption experiments. Upon construction, functionality of the spectrometer was confirmed by studying a gas phase photodissociation reaction. This was followed by simulations and experimental work in order to verify the existence of an increased VMI area, and to quantify the size of the VMI area created by using a twelve electrode stack. Having established the presence of a VMI area which was of adequate dimensions, the spectrometer was modified by introducing a surface into the electrode stack in preparation for surface desorption experiments.

The near threshold dissociation of chloroform, $CHCl_3$, via Q←N electronic transitions was investigated using the newly constructed VMI spectrometer. Kinetic energies, β parameters and branching ratios of the ground state Cl and spin-orbit excited state Cl* products were determined for dissociation at 193 nm and 235 nm. It was found that the three optically accessible states within

the Q band are all involved in the dissociation process, with the lowest excited state, $^3Q_1$, being increasingly important at lower photon energies. This is in contrast to previous work on near threshold chloroform dissociation, which has generally assumed minimal involvement from the $^3Q_1$ state. In addition, for 193 nm dissociation, the proportions of products being produced via the four observed reaction pathways (two of which were seen to involve curve crossing, from $^1Q_1$ to $^3{Q_0}^+$, and vice versa, in the Franck-Condon region) has been proposed.

In preparation for modifying the spectrometer, a gas phase investigation was carried out to confirm experimentally that the twelve electrode stack resulted in a VMI area ∼6 - ∼7 times wider than that resulting from a three electrode stack, as indicated by simulations. NO_2 molecules within a number of molecular beams travelling along the spectrometer (essentially parallel to one another) at various distances from the central TOF axis were dissociated, and VMI images resulting from fragments detected at the various molecular beam positions were obtained. These images were analysed in terms of three characteristics which were selected to constitute a reliable measure of the quality of the VMI focussing conditions. A VMI area ∼12 mm wide was confirmed, which will allow the detection of fragments desorbed from a surface over an angular range of $\pm 50^{\circ}$ (which can be increased to $\pm 75^{\circ}$ if required) relative to the surface normal. The actual VMI area is slightly lower than the 15 mm wide area predicted by simulations, but nonetheless is larger than the 10 mm wide VMI area which is the minimum that was required here. These experiments represent the first systematic study and experimental validation of the VMI area.

This work has important implications for any studies which use VMI to detect kinetic energy distributions of product fragments detected over a large area. These include scattering studies using a molecular beam and a surface, or two crossed molecular beams, and surface desorption experiments (specifi-

cally those which employ the dot-sheet optical geometry). It has been shown that a standard, three electrode, VMI spectrometer is not suitable for such investigations, since the discrepancy between the VMI area and the area over which fragments are detected will result in a marked drop in image quality and hence in resolution, potentially even in accuracy.

There are certain limitations with the aforementioned work. While the large increase in VMI area resulting from the use of weak extraction has for the first time been experimentally demonstrated, the quantification of the size of the VMI area is only valid for the VMI spectrometer described here. Moreover, the potential factors influencing weak extraction, and thus the size of the VMI area, were not isolated. This creates the potential for future study to develop a more rigorous and more widely applicable formulation of the relationship between the size of the VMI area and the factors which influence its size.

A more rigorous study should involve simulations and experiments like those described here, but carried out multiple times to test different variables. For example, by repeating the NO_2 study using different reactant molecules (and thus fragments with different kinetic energies) one could vary the voltage on the repeller electrode and investigate the correlation between absolute voltage and the size of the VMI area. In a similar way, the experiments could be performed with the product molecule and repeller voltage remaining constant, and the partitioning of the repeller and extraction regions changing. Here, electrodes one to four constituted the repeller region, four to seven the transition region and seven to twelve the extraction region. Varying the number of electrodes over which these regions extend and testing the size of the VMI area could serve to determine the optimal ratio between the length of the repeller and extraction regions in a multiple electrode spectrometer. Finally, the effect of the number of electrodes involved could be investigated. It is interesting to note that a three electrode spectrometer produces a VMI area $\sim$2 mm wide, the twelve electrode apparatus here produces a VMI area $\sim$12 mm wide, and a

twenty-nine electrode configuration produces a VMI area ∼25 mm wide. This seems to suggest an almost linear relationship between the number of electrodes and the dimensions over which the VMI focussing conditions extend, which could be investigated in order to determine at what number of electrodes (if any) a point of diminishing returns in terms of VMI area is reached, thus determining an upper limit for the utility of weak extraction in increasing the VMI area.

Having verified the VMI area and adapted the spectrometer for surfaces, future work will investigate surface desorption processes. For example, gas-phase molecules colliding with a surface can undergo a variety of reactions. These can be split into two categories: impulsive scattering and trapping desorption. Impulsive scattering involves the molecules colliding with the surface with and travelling away from it with minimal interaction. Alternatively, the molecule may interact with the suface and remain there for some time. Using the apparatus described here, the nature of the gas-surface collision can be determined since the molecules' directions of travel after leaving the surface will depend on the nature of their interaction with it. This direction along the two axes parallel to the surface could be determined using VMI. Additionally, the internal and kinetic energies of the molecules will also vary depending on the surface interaction, and these can be resolved using the narrow-bandwidth lasers as a probe source.

Molecules already on a surface with surfaces can undergo a range of processes. They may be attached to the surface either by strong chemical bonds (physisorption) or weaker intermolecular interactions (physisorption, i.e. van der Waals interactions). For a molecule attached to the surface, when the interactions anchoring it to the surface are removed (by excitation of the molecule by a laser beam for instance), the molecules can either immediately travel away from the surface using the excess energy which remains following excitation and bond breaking, or they may move around on the surface, losing some of

this excess energy to the surface by exciting the surface molecules in various ways. As with bimolecular studies, the nature of the processes in which the molecule partakes after dissociation will have an affect on both its internal energy and kinetic energy (including direction of travel). In both cases, the internal energy distributions of the molecules can be resolved using narrow-bandwidth lasers, and the kinetic energy can be accurately determined using VMI and TOF methods.

Consequently, with the current apparatus having been constructed, calibrated and optimised, and having the VMI area well-defined and characterised, future use of the apparatus for studying surface reactions is potentially hugely broad: it may be applied to metal, semiconductor or "soft" organic surfaces. For example, more complex molecules such as self assembled monolayers (e.g. thiols adsorbed on gold) would seem to be highly amenable to study using this surface VMI apparatus. A variety of thiols can be produced, resulting in surface adsorbed molecules which can be used as analogues of various other compounds. This can allow conclusions to be drawn about the behaviour of such molecules at interfaces by using monolayer proxies (e.g. a thiol terminated with a -CCl_3 group could be used to approximate PVC).

For such surface studies, the apparatus can be used to study either the interactions of gas phase molecules which impinge upon the surface, or to investigate molecules which are already adsorbed to the surface, and the processes which they undero after excitation. In addition, the energy "pump" source could be anything which is feasible: lasers, electrons (low or high energy), high energy photons etc. For any surface, adsorbent and pump source, the dynamics in question can be more fully investigated due to the ability to alter the temperature of the surface.

The VMI spectrometer whose construction and characterisation has been outlined in this document can be (and has been) used to successfully study gas phase photodissociation reactions. In addition, it has been amended so

that it can now also be applied to studies of surface desorption dynamics. The weak extraction conditions produced by the twelve electrode stack allow the detection of fragments over a much larger area than that provided by a standard VMI spectrometer. The first experimental validation of this increase of the VMI area has herein been reported. In the future it will be possible for a wide variety of dissociative processes at surfaces, induced by a variety of means, to be investigated using this spectrometer, and it should also be possible to apply it to the study of scattering from surfaces, should this be desired. As a result, the apparatus and experiments here described have general implications for VMI studies in which products are detected over larger areas, and also pave the way for future experimental studies of a wide variety of interfaces and dissociation processes.

Appendix A

Appendices

A.1 Electrode Gradient Ratios

The apparatus uses a twelve electrode stack. The voltage is reduced linearly between electrode one and electrode four to form the repeller region. The voltage between electrode seven and electrode twelve is also reduced linearly, forming the extraction region. It is the ratio of the voltage gradient over electrodes seven to twelve, to the gradient over electrodes one to four, which must be tuned in order to achieve VMI focussing conditions. The change in voltage between electrodes four and five, five and six, and six and seven is gradually increased in order to ensure a smooth transition between repeller and extraction gradients.

Electrode one is biased at a known voltage (R), and the voltages on electrodes two to four are reduced linearly. The difference between one and two, two and three etc is the repeller region gradient, denoted A. The voltages on electrodes seven to twelve are also reduced linearly, the reduction in this region being the extraction region gradient, denoted E. The ratio of the regions ($\frac{E}{A}$), denoted Z, is the crucial factor in obtaining good VMI focussing conditions. E.g. For $Z = 2$, the drop in voltage between electrodes seven and eight, eight and nine etc is double that between one and two, two and three etc.

Additionally, electrodes five and six comprise the "transition region" and need to provide a gradually increasing gradient. The voltage difference between electrodes four and five needs to be slightly higher than that between three and four, that between five and six needs to be slightly higher again, between six and seven slightly higher again and between seven and eight it should be E. This is accomplished by adding integer multiples of a transition factor (X) to the value of A, i.e. $A + X$ on electrode five; $A + 2X$ on electrode six etc. This is repeated as far as electrode eight, after which the gradient is kept constant.

The above can be summarised as:

Electrode	Voltage	Cumulative Total of Drops in Voltage
1	R	-
2	electrode 01 - (A)	A
3	electrode 02 - (A)	$2A$
4	electrode 03 - (A)	$3A$
5	electrode 04 - $(A + X)$	$4A + X$
6	electrode 05 - $(A + 2X)$	$5A + 3X$
7	electrode 06 - $(A + 3X)$	$6A + 6X$
8	electrode 07 - $(A + 4X)$	$7A + 10X$
9	electrode 08 - $(A + 4X)$	$8A + 14X$
10	electrode 09 - $(A + 4X)$	$9A + 18X$
11	electrode 10 - $(A + 4X)$	$10A + 22X$
12	electrode 11 - $(A + 4X)$	$11A + 26X$

As electrode twelve is ground, R is equal to the total drop in voltage over the electrodes:

$$R = 11A + 26X \tag{A.1}$$

The extraction gradient is equal to $A + 4X$, the repeller gradient is equal to A. Therefore:

$$Z = \frac{(A + 4X)}{A} \tag{A.2}$$

Rearranging equation A.2:

$$X = \frac{(A.Z - A)}{4} \tag{A.3}$$

Substituting A.3 into A.1:

$$11A + 26(\frac{A.Z - A}{4}) = R \tag{A.4}$$

Expanding and rearranging A.4:

$$A = \frac{4R}{(26Z + 18)} \tag{A.5}$$

In a VMI experiment, one wishes to specify the value of R and then tune the value of Z in order to optimise the focussing conditions.

This is achieved by specifying R and then, for a given value of Z, using equation A.5 to work out A. A and Z can then be used to work out X using equation A.3. Having specified R and Z, and worked out A and X the voltage on each electrode can be assigned as above (e.g. electrode eight is assigned the voltage on electrode seven - $(A + 4X)$). For the experiments described here, a simple spreadsheet was created based on the above equations which allowed the voltage on each electrode to be calculated immediately for any given value of R and any given value of Z.

A.2 Validating VMI Paper

REVIEW OF SCIENTIFIC INSTRUMENTS **84**, 044101 (2013)

Validation of velocity map imaging conditions over larger areas

Mike Reid[1,2,3] and Sven P. K. Koehler[1,2,3,a)]
[1]*School of Chemistry, The University of Manchester, M13 9PL Manchester, United Kingdom*
[2]*Photon Science Institute, The University of Manchester, M13 9PL Manchester, United Kingdom*
[3]*Dalton Cumbrian Facility, The University of Manchester, Moor Row, CA24 3HA Whitehaven, United Kingdom*

(Received 21 January 2013; accepted 17 March 2013; published online 5 April 2013)

We have established through simulations and experiments the area over which Velocity Map Imaging (VMI) conditions prevail. We designed a VMI setup in which we can vary the ionization position perpendicular to the center axis of the time-of-flight spectrometer. We show that weak extraction conditions are far superior over standard three-plate setups if the aim is to increase the ionization volume without distorting VMI conditions. This is important for a number of crossed molecular beam experiments that already utilize weak extraction conditions, but to a greater extent for surface studies where fragments are desorbed or scattered off a surface in all directions. Our results on the dissociation of NO_2 at 226 nm show that ionization of the fragments can occur up to ± 5.5 mm away from the center axis of the time-of-flight spectrometer without affecting resolution or arrival position.
 [http://dx.doi.org/10.1063/1.4798646]

I. INTRODUCTION

Over the last 15+ years, Velocity Map Imaging (VMI) has become one of the most extensively used techniques in the area of gas-phase reaction dynamics.[1–3] It is employed in photodissociation studies,[4] photoelectron imaging,[5,6] and cluster experiments to name a few.[7] VMI has evolved from ion imaging techniques developed in the mid-1980s whose aim it was to simultaneously record kinetic energy and angular distributions of product fragments.[8] In a typical photodissociation experiment, the molecule of interest is dissociated, typically using laser radiation, and one (or multiple) fragment(s) are ionized, often in a REMPI (resonance-enhanced multi-photon ionization) scheme. These fragments, which travel with essentially the same velocity as their parent fragments due to the negligible mass of the ejected photoelectron, are accelerated within a set of ion optics towards a position-sensitive detector. From the fragments' arrival position, information about their kinetic energy and angular distributions can be gained.

The major breakthrough stemming from the advent of VMI is the increased velocity resolution; by omitting the grids that were used in the ion optics until then, a "lensing" effect is achieved.[1] The increased resolution manifests itself in the fact that the position where the ions are created (the cross section of the molecular beam and the ionization laser) no longer affects the arrival position on the detector. However, this cross section is most often only a small cylinder created typically by a focused laser beam of tens or hundreds μm diameter intersecting a molecular beam of a couple of mm diameter. "Standard" VMI ion optics using a repeller, extractor, and ground plate can easily velocity map all fragments ionized in this small cylinder.

More refined ion optics arrangements have been devised with various aims in mind. The addition of extra electrodes can improve resolution, magnify the image, and allows the ion cloud to be stretched in the time-of-flight (TOF) direction which opens up the possibility of slicing.[9–11] Recording only the central portion of the ion cloud supersedes the need for an error-prone Abel transformation of the raw image.[12] Weak extraction conditions (for electron imaging from anionic species) have also been reported in order to maintain low fields in the interaction region to avoid deflecting the ion beam.[13]

Most relevant to the present paper, weak extraction conditions for ion imaging have been devised by Liu and co-workers[14] and Yang and co-workers[15] for crossed-molecular beam studies, and are also used by Reisler and co-workers[16] and Powis and co-workers,[17] amongst others. In crossed-molecular beam experiments, fragments may potentially scatter in all directions and hence may have to be ionized in a large volume. Ion optic designs consisting of between 20 and 30 electrodes have been constructed, and in addition to the fact that these can conveniently be used to slice the ion cloud, it has been found that these weak extraction conditions increase the area (where area is a slice parallel to the repeller plate) over which VMI conditions prevail.[14,15] While a shift in ionization position *along* the TOF axis still changes imaging conditions (though to smaller extent) as already reported in the first VMI paper,[1] shifts in the two dimensions perpendicular to the TOF axis do not seem to significantly change results in these multi-plate setups. The closely spaced electrodes are typically divided into three parts with the first few electrodes ensuring weak field conditions, and the last electrodes supplying the strong fields necessary to image the ions onto the detector, with a few intermediate electrodes to ensure a smooth transition between the two regions.

We set out to optimize weak extraction conditions for surface VMI studies. Some early reports that use VMI for surface desorption and scattering studies have emerged from various laboratories over the last three years.[18–22] It is evident that neutral fragments desorbed from or scattered off a surface can fly in all directions of the hemisphere above the surface. In contrast to surface studies using rotatable mass-spectrometers, surface VMI can record these fragments

a)sven.koehler@manchester.ac.uk

flying in all directions simultaneously, but only if all fragments covering the whole angular distribution are ionized. To make this point clearer: If fragments originate only from a very small spot on the surface and are ionized by a point-source a few mm above the surface directly in front of the originating spot on the surface, then only those fragments flying normal to the surface are being detected; this not only squanders the advantages of the VMI technique, but more importantly yields biased or even incorrect results with respect to the speed and angular distributions. Hence, in a laser-desorption experiment with REMPI detection, one has to ensure that (literally) all angles are covered; this can be done by increasing the diameter of one of the two laser beams involved. A comparison with optical slicing methods applied in typical gas-phase imaging experiments is helpful here. In order to let the ion cloud expand, it is possible to dissociate the molecule of interest using a point-focused laser beam, but to detect the fragments using a laser sheet (created by employing a cylindrical lens or by rastering the laser up and down) after some time delay to allow the ion cloud to expand as shown by Suits and co-workers.[23] Counter-intuitively, Chestakov *et al.* used a sheet-focused dissociation laser and a point-focused ionization laser; this setup still achieves the goal that fragments flying in all directions are detected, but this time with a higher laser fluence which can be advantageous for many REMPI detection schemes.[24]

For surface experiments, fragments can be similarly desorbed from a small spot and detected a few mm above the surface using a REMPI laser sheet (dot-sheet); alternatively, a large diameter desorption laser beam can be employed (or a few mm diameter molecular beam impinging on the surface) and fragments ionized using a point-focused ionization laser (sheet-dot), see Fig. 1. While the latter has already been employed and has advantages in terms of REMPI laser fluence,[18] the dot-sheet configuration is more intuitive. However, at a typical surface-laser distance of 5 mm, the REMPI laser sheet has to be 10 mm wide to collect a 90° angle symmetric to the surface normal, and VMI conditions have to prevail in the entire volume in which fragments are ionized.

While the beauty of VMI lies in the fact that the arrival position on the detector is independent of where the ions are formed, but is instead only a function of their velocity, this is only true for a small area around the center axis within the ion optics; this work reports for the first time how far away from the center axis of the VMI spectrometer one can ionize without compromising arrival position or resolution.

II. EXPERIMENTAL SETUP

Our new VMI spectrometer consists of a molecular beam and a TOF chamber, the latter of which contains the VMI optics and detector (shown in Fig. 2). A molecular beam is formed by supersonic expansion of a 1%–3% mixture of the target molecule (here NO_2 or Cl_2) in He through a General Valve (500 μm diameter orifice, 300 μs opening time) pulsed valve at a stagnation pressure $p_{abs} = 1.5$ bars, resulting in a beam velocity of around 1000 m s^{-1}. A Beam Dynamics skimmer (model 2, 1.2 mm orifice) is mounted 15 mm away from the valve exit and separates the beam chamber from the

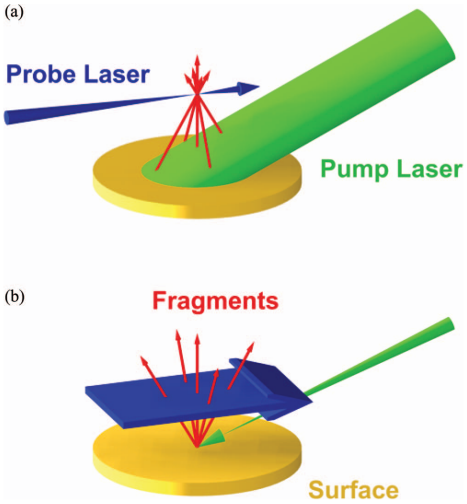

FIG. 1. Illustration of two possible pump-probe geometries to simultaneously detect angular distributions in a surface Velocity Map Imaging spectrometer. The sheet-dot configuration (a) has advantages in terms of probe laser fluence due to the focusing, while the dot-sheet configuration (b) is more intuitive but requires refined Velocity Map Imaging conditions.

TOF chamber. Both chambers are evacuated by 1000 l s^{-1} turbomolecular pumps. The valve and skimmer are mounted inside a brass "birdcage" assembly as found in many laboratories. After a flight path of 25 cm, the molecular beam enters a set of ion optics. The first plate, commonly referred to as repeller plate, is a standard 10 cm diameter stainless steel plate (1 mm thick) with a central 2 mm hole to accept the molecular beam. For the experiments described here, this plate is replaced by a plate with 1.5 mm diameter holes placed 1, 3, 5, and 7 mm below, and 2, 4, and 6 mm above the center axis, see Fig. 3.

The repeller plate is the first of 12 electrodes that constitute the ion optics in our setup, all 1 mm thick with a diameter of 10 cm and spaced 9.5 mm apart. These are surrounded over the entire length by a shielding cylinder with a radius of 6 cm containing a pair of horizontally aligned holes for laser access between the first two electrodes. The ion optics are biased by home-built power supplies based on four Applied Kilovolts (HP005PPP025) modules; the first four

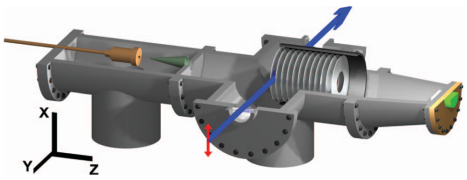

FIG. 2. Schematic of our Velocity Map Imaging spectrometer showing the placement of the ion optics within the vacuum apparatus, and the propagation direction of the REMPI laser which can be translated vertically.

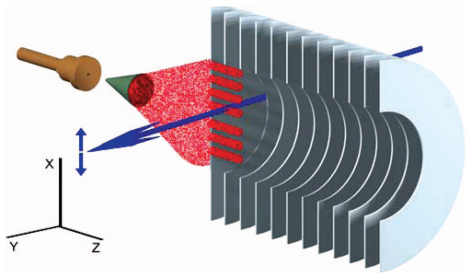

FIG. 3. Close-up cut-out of the first few electrodes showing the vertically offset holes in the repeller plate intersected by the REMPI laser. Distance of the molecular beam valve and skimmer to the ion optics not to scale.

electrodes are controlled by one module using variable external voltage dividers to provide four independently tunable voltages, while electrodes five and six are controlled by a separate module each. The last electrode is permanently grounded, and electrodes 7–11 are controlled in a similar fashion to electrodes 1–4. The optimum ratio of the electric field gradient between the first and second region is around 2.5, and imaging conditions (and magnification) can be most easily tuned by changing that ratio. At an overall acceleration voltage of 1000 V, this setup allows us to have relatively weak fields in the interaction region (~50 V cm^{-1} and ~125 V cm^{-1} in the latter stages of the setup) while still being able to image all fragments in the photodissociation of NO_2 or Cl_2 at ~226 and 351 nm, respectively. The fragments are detected by a 40 mm MCP (Chevron-type, Burle Photonis) coupled to a Phosphor screen mounted on a CF100 flange at the end of a 45 cm flight path. The MCP can be operated in pulsed mode using a DEI PVX-4140 high voltage pulser, which together with our weak extraction conditions allows us to perform DC slicing. Images from the Phosphor screen are recorded using a synchronized charge coupled device (CCD) camera (FOculus FO124TB, 640 × 480), and the captured images transferred to a PC using a National Instruments frame grabber (NI PCI-8254R). Custom-written LabVIEW software is used to accumulate and save the images, centroiding and further analysis can also be performed by this program.

The center between the first and second electrode is at the center of a custom-made 6-way cross where the molecular beam is intersected by a photolysis and detection laser.

Cl_2 is dissociated using a 351 nm Excimer laser (Questek 2110, 15 ns pulsed, 50 mJ $pulse^{-1}$) whose output is split by a quartz window mounted at Brewster's angle to give <2 mJ vertically polarized light which is focused by a 30 cm lens. The third harmonic of a Continuum Powerlite 8020 is used to pump a Radiant Dyes NarrowScan laser using Coumarin 470 to output 7 ns (FWHM) long pulses which are frequency-doubled in a BBO crystal to yield 1–2 mJ of laser radiation between 230 and 235 nm. This light (vertically polarized using a periscope) is tightly focused by a 20 cm lens and counter-propagates the photolysis laser. Chlorine atoms in the electronic ground-state but with different spin-orbit splitting ($^2Cl_{3/2}$ (Cl) and $^2Cl_{1/2}$ (Cl*)) are detected by REMPI spectroscopy via the $^2D_{3/2}$ and $^2P_{3/2}$ transitions at 235.326 and 236.518 nm, respectively. REMPI spectra and images for NO after NO_2 dissociation at around 226 nm were recorded on the (0,0) A ← X band.

III. RESULTS

A. Simulations

In the past, improvements have been made to the standard three plate ion optics design for VMI experiments for various reasons. More sophisticated designs were devised to improve resolution; one or two additional plates were introduced to spread the ion cloud for DC slicing;[23] delayed fields were applied to the optics for slicing;[25] many-plate setups were devised for crossed-molecular beam experiments in order to increase the ionization volume and to derive the velocity in the z dimension (along the TOF) directly;[14,15] and the use of a continuously varying field using a glass tube in order to minimize electric fields in the interaction region for ion beam studies.[13] Our main aim here was to design a relatively simple set of ion optics that can be used for surface VMI studies. As it is imperative to collect fragments leaving the surface under all possible angles, it is necessary (in the case of the more intuitive arrangement where the fragments leave the surface from a small spot) to ionize the fragments over a large area in front of the surface where the surface is typically incorporated into the repeller plate. This in turn requires VMI conditions to prevail over a large area in front of the surface in case of the dot-sheet geometry.

If the fragments are ionized a few mm in front of the surface by a pulsed laser, then this laser probes a subset of the ejected/scattered fragments with a certain speed determined by the surface-probe laser distance and the pump-probe delay; varying the timing of this probe laser with respect to the event causing the fragments to leave the surface allows one to record TOF profiles and ultimately speed distributions along the surface normal. Hence optimizing sliced-VMI conditions in order to derive v_z was not the main aim of our design (albeit nonetheless possible) as this is easier performed recording TOF profiles. The creation of a reasonably large area on which VMI conditions prevail was instead the main aim here, and the experimental validation of how large this area is.

To that end, we settled for a design employing 12 electrodes as a reasonable compromise between experimental complexity and increased VMI area. Trajectory simulations (SIMION 8.0, Scientific Instrument Services, Inc.) were performed with ion origins offset up to ±7.5 mm either side of the center axis of the TOF spectrometer, where the two dimensions x and y parallel to the repeller plate and detector are equivalent due to the cylindrical symmetry of the ion optics. Using conditions chosen to mimic NO_2 photodissociation at 226 nm at seven different positions, the overall resolution at 1000 V overall acceleration voltage is better than 2%, see Fig. 4; this can be compared to the resolution obtained when only the first three electrodes are biased which is >8% (employing a 15 mm distance between ion origins).

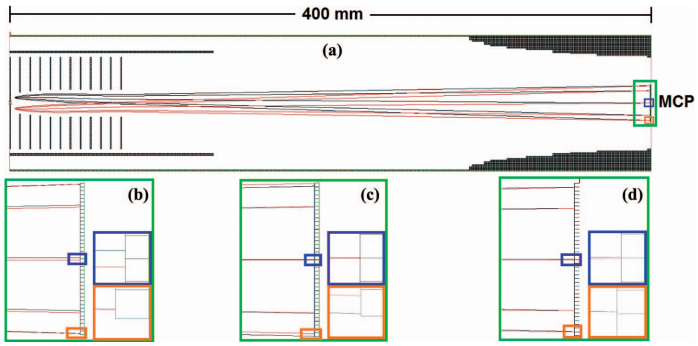

FIG. 4. Ion trajectories simulated using SIMION 8.0 demonstrating the resolution obtained when (b and c) three electrodes, and (d) 12 electrodes are used. The origin of the ions is ±7.5 mm offset from the center axis of the spectrometer. The close-ups show a resolution better than 2% for the more elaborate setup compared to 8% for either 3-plate setup.

B. Calibration

The apparatus was velocity calibrated by studying the well-known photodissociation of Cl_2 at 351 nm using the output of an Excimer laser running XeF.[26,27] The 351 nm beam was reflected off a quartz window mounted at Brewster's angle, and the predominantly vertically polarized beam was focused using a 30 cm plano-convex lens. Cl fragments were recorded via the Cl ($^2D_{3/2}$) (Cl) and the Cl ($^2P_{3/2}$) (Cl*) transition at 235.326 and 236.518 nm, respectively. Integration of the images over all angles delivers peaks at radii with a linear relationship to the predicted velocity. The resolution is around 1% for a 2 mm diameter molecular beam. (Note that the resolution quoted above was from simulations in which the ions' origins deviate by ±7.5 mm from the TOF axis.)

C. Offset results

We used the one-color photodissociation of NO_2 to verify the extent of the VMI area. The molecular beam containing 1%–3% of NO_2 in He was skimmed and after a flight path of 25 cm introduced to the ion optics assembly. NO_2 was dissociated at 226.1 nm and NO($^2\Pi_\Omega$) fragments recorded on the (0,0) A ← X band. At this wavelength, the counter-fragment oxygen is produced as O(^3P) and O(^1D), and through a number of different NO intermediate states, the various known peaks in the NO kinetic energy distribution are formed.[28]

Initially, various different repeller plates were used in succession, each with a single 2 mm hole at a different offset position, and the plates were changed between experiments. However, the position of the electrode assembly after changing the repeller plate was not reproducible, with noticeable consequences for the ion arrival position (offset by up to tens of pixels), and hence an alternative arrangement was devised that avoided having to disassemble the ion optics for each position. A single repeller plate containing multiple vertically arranged holes (1.5 mm diameter) was used instead, see Fig. 3. Over the 25 cm distance between the centrally mounted skimmer and the repeller plate, the molecular beam expands, resulting in a beam diameter >20 mm. Using the multi-hole repeller plate, we hence created a series of almost parallel beams travelling along the TOF axis between the first and second plate. The fact that beams further away from the center axis are not parallel to the center beam is almost negligible but accounted for in the analysis. The dissociation and ionization laser beam can be moved in the vertical direction by means of a translational micrometer stage, thus allowing any one of the multiple molecular beams to be intersected and imaged.

We performed imaging experiments at interaction positions vertically offset by −7, −5, −3, −1, 2, 4, and 6 mm from the TOF axis. These positions were defined by the holes in the repeller plate, and the greatest offsets limited by the size of our viewport. Quadrants of the recorded images are shown in Fig. 5. As our goal was to measure how far away from the center axis fragments could be ionized while still adhering to Velocity Map Imaging conditions, the following conditions must be fulfilled: Not only must the different images be identical in size and shape, but most importantly the images must not move for different molecular beam positions; such a shift of the image position on the detector for fragments with identical velocities but different molecular beam positions would equate to an error in the determination of the velocity, and would significantly limit the resolution of the apparatus. We hence analyzed the images in three ways in order to quantify the validity of VMI conditions: (a) The center of inversion of each image was compared to the image recorded with no molecular beam offset, and the displacement converted to a velocity shift using our calibration function. (b) The peak kinetic energy of the most intense ring was determined for all images to ensure that the magnification does not change significantly. (c) The FWHM in the velocity distributions of the main ring was compared for different images. The determination of the center of inversion of each image was performed using a routine in BASEX.[29] Since the molecular beam originates from one point, namely the centrally mounted

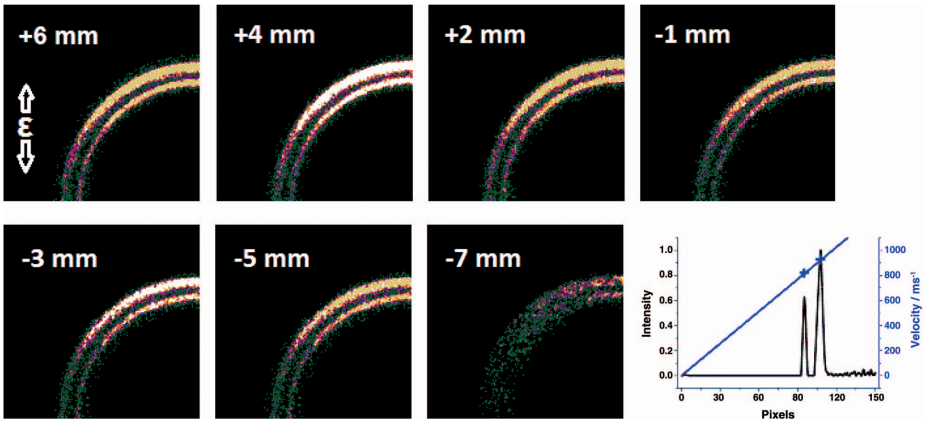

FIG. 5. Ion images (top-left quadrants, not averaged by mirroring) of NO^+ after dissociation of NO_2 at ~226 nm and 1 + 1 REMPI ionization of NO fragments. The potential on the first plate is 1000 V, and the laser polarization is indicated by ε. Final graph is the raw velocity distribution showing the linear relationship between image radius and velocity.

molecular beam valve, each beam has an off-axis velocity component proportional to the offset of the respective hole. We accounted for this shift which does not amount to more than 10 m s^{-1} even for the holes furthest away from the center.

When using VMI for surface studies in the dot-sheet geometry, it is necessary to ensure that all fragments with the same velocity ionized anywhere within a defined volume are imaged onto the same spot on the detector, and that neither the arrival position nor the resolution are compromised. The results shown in Fig. 6 show that with our VMI setup, these conditions are comfortably fulfilled up to a position 5.5 mm away either side of the center of the TOF axis.

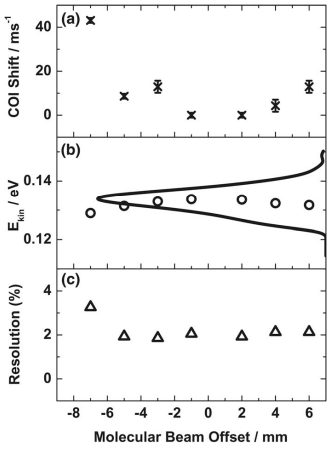

FIG. 6. (a) Displacement of the center-of-inversion (COI) of the seven images shown in Fig. 5 expressed as a perceived velocity shift (compared with the molecular beam aligned along the center axis) as a function of molecular beam offset. (b) Peak kinetic energy of the NO fragment of the most intense channel after NO_2 photodissociation at 226 nm. Also shown on the vertical axis is the kinetic energy distribution of this peak for comparison. (c) Resolution of the most intense NO production channel after 226 nm photolysis of NO_2 as a function of molecular beam offset.

IV. DISCUSSION AND CONCLUSIONS

We set out to experimentally verify how far away from our spectrometer's center axis VMI conditions still prevail. Multi-plate VMI setups have been used in the past primarily to stretch the ion cloud to allow the z-component of the velocity to be resolved with high precision, but also to increase the volume in which VMI conditions prevail for crossed-molecular beam studies; both aims are achieved by using weak extraction fields in the interaction region. We have shown here that our soft focusing conditions using 12 electrodes can image fragments that are up to ±5.5 mm away from the center of the TOF axis while still adhering to VMI conditions, i.e. focusing all fragments with the same velocity onto the same spot on the detector. While we have only tested these conditions in one dimension (vertical or x-direction), our results indicate that VMI conditions prevail in a plane parallel to the surface (or repeller plate) and roughly 95 mm^2 in area due to the cylindrical symmetry of the ion optics; this area can easily be covered by a probe laser sheet. We note that fragments ejected from or scattered off the surface non-symmetrically can also be resolved with our setup. The low electric fields in the interaction region also make the setup less susceptible to variations to the exact position of the probe laser along the direction of the molecular beam (z-direction), however, this has been kept constant in the present experiments, and could also feasibly remain unchanged when using a sheet-focused REMPI laser.

The reported results are relevant to surface studies using the VMI technique in which fragments are ejected from or scattered off a surface. While the signal-to-noise ratio is superior for a geometrical arrangement in which the "pump"-event covers a large area of the surface and the probe laser is focused to a small spot centrally located in front of the pump area, the more intuitive geometry involves a small-diameter desorption laser or molecular beam and a large laser sheet to ionize the fragments. In either case, delaying the probe laser with respect to the pump event and precisely knowing the distance between surface and probe laser allows one to perform TOF measurements which can deliver the speed distribution in the z-direction; in addition, the two speed distributions parallel to the surface (and detector), i.e. in the x- and y-direction, can be recorded to yield three-dimensionally resolved velocity distributions if combined appropriately.

In the few surface VMI experiments reported, the REMPI laser was usually focused between 1.5 and 4 mm in front of the surface.[18–20,22] The solid angle of the cone that is reliably covered by a REMPI laser sheet is given by $2 \times \tan^{-1}(d_\ell/2 \times z)$ where d_ℓ is the diameter of the laser sheet and z is the surface-laser distance. In other words, we could easily choose to record the whole velocity distribution within a 120° cone by placing the laser sheet 3.2 mm in front of the surface.

This is cautioning on the safe side determined by our experimental conditions which yielded a diameter of 11 mm whereas our simulations yielded 15 mm. If a larger surface-laser distance and hence a larger REMPI sheet is required, then the consequence is only a reduction of the resolution by around 2% for each added mm in the diameter of the laser sheet. While this may be unacceptable for the understanding of some surface processes, many surface reactions exhibit quite broad angular scattering distributions which could still be fitted from slightly lower resolution velocity map images.

In summary, we have described our new multi-plate VMI setup and measured the extent of the area parallel to the VMI electrodes in which VMI conditions prevail without compromising VMI conditions. The significance of the size of this area has already been realized for crossed-molecular beam studies, but is even more apparent for surface VMI studies. Our results show that under the right geometric conditions, it will be possible to record fully resolved 3D velocity distributions after surface reactions using the more-intuitive dot-sheet geometry.

ACKNOWLEDGMENTS

We thank the Dalton Cumbrian Facility program in part funded by the Nuclear Decommissioning Authority for financial support, the Photon Science Institute at the University of Manchester for the long-term loan of a YAG-pumped dye laser, and both the mechanical and electronics workshops in the School of Chemistry for their significant contributions during the development of the apparatus.

[1] A. T. J. B. Eppink and D. H. Parker, Rev. Sci. Instrum. **68**, 3477 (1997).
[2] M. N. R. Ashfold, N. H. Nahler, A. J. Orr-Ewing, O. P. J. Vieuxmaire, R. L. Toomes, T. N. Kitsopoulos, I. A. Garcia, D. A. Chestakov, S.-M. Wu, and D. H. Parker, Phys. Chem. Chem. Phys. **8**, 26 (2006).
[3] A. I. Chichinin, K.-H. Gericke, S. Kauczok, and C. Maul, Int. Rev. Phys. Chem. **28**, 607 (2009).
[4] D. Townsend, S. K. Lee, and A. G. Suits, J. Phys. Chem. A **108**, 8106 (2004).
[5] T. Suzuki, Annu. Rev. Phys. Chem. **57**, 555 (2006).
[6] C. S. Lehmann, N. B. Ram, and M. H. M. Janssen, Rev. Sci. Instrum. **83**, 093103 (2012).
[7] W. S. Hopkins, A. P. Woodham, N. M. Tonge, A. M. Ellis, and S. R. Mackenzie, J. Phys. Chem. Lett. **2**, 257 (2011).
[8] D. W. Chandler and P. L. Houston, J. Chem. Phys. **87**, 1445 (1987).
[9] C. R. Gebhardt, T. P. Rakitzis, P. C. Samartzis, V. Ladopoulos, and T. N. Kitsopoulos, Rev. Sci. Instrum. **72**, 3848 (2001).
[10] H. L. Offerhaus, C. Nicole, F. Lépine, C. Bordas, F. Rosca-Pruna, and M. J. J. Vrakking, Rev. Sci. Instrum. **72**, 3245 (2001).
[11] E. Wrede, S. Laubach, S. Schulenburg, A. Brown, E. R. Wouters, A. J. Orr-Ewing, and M. N. R. Ashfold, J. Chem. Phys. **114**, 2629 (2001).
[12] A. J. R. Heck and D. W. Chandler, Annu. Rev. Phys. Chem. **46**, 335 (1995).
[13] D. A. Horke, G. M. Roberts, J. Lecointre, and J. R. R. Verlet, Rev. Sci. Instrum. **83**, 063101 (2012).
[14] J. J. Lin, J. Zhou, W. Shiu, and K. Liu, Rev. Sci. Instrum. **74**, 2495 (2003).
[15] G. Wu, W. Zhang, H. Pan, Q. Shuai, B. Jiang, D. Dai, and X. Yang, Rev. Sci. Instrum. **79**, 094104 (2008).
[16] M. Ryazanov, C. Rodrigo, and H. Reisler, J. Chem. Phys. **136**, 084305 (2012).
[17] G. A. Garcia, L. Nahon, C. J. Harding, E. A. Mikajlo, and I. Powis, Rev. Sci. Instrum. **76**, 053302 (2005).
[18] S. P. K. Koehler, Y. Ji, D. J. Auerbach, and A. M. Wodtke, Phys. Chem. Chem. Phys. **11**, 7540 (2009).
[19] Y. Ji, S. P. K. Koehler, D. J. Auerbach, and A. M. Wodtke, J. Vac. Sci. Technol. A **28**, 807 (2010).
[20] D. Sporleder, D. P. Wilson, and M. G. White, J. Phys. Chem. C **113**, 13180 (2009).
[21] J. R. Roscioli and D. J. Nesbitt, Faraday Discuss. **150**, 471 (2011).
[22] J. R. Roscioli, D. J. Bell, D. J. Nelson, and D. J. Nesbitt, Phys. Chem. Chem. Phys. **14**, 4070 (2012).
[23] D. Townsend, M. P. Minitti, and A. G. Suits, Rev. Sci. Instrum. **74**, 2530 (2003).
[24] D. A. Chestakov, S. M. Wu, G. R. Wu, D. H. Parker, A. T. J. B. Eppink, and T. N. Kitsopoulos, J. Phys. Chem. A **108**, 8100 (2004).
[25] R. L. Toomes, P. C. Samartzis, T. P. Rakitzis, and T. N. Kitsopoulos, Chem. Phys. **301**, 209 (2004).
[26] P. C. Samartzis, I. Sakellariou, T. Gougousi, and T. N. Kitsopoulos, J. Chem. Phys. **107**, 43 (1997).
[27] A. J. Alexander, Z. H. Kim, S. A. Kandel, R. N. Zare, T. P. Rakitzis, Y. Asano, and S. Yabushita, J. Chem. Phys. **113**, 9022 (2000).
[28] I. Wilkinson, M. P. de Miranda, and B. J. Whitaker, J. Chem. Phys. **131**, 054308 (2009).
[29] V. Dribinski, A. Ossadtchi, V. A. Mandelshtam, and H. Reisler, Rev. Sci. Instrum. **73**, 2634 (2002).

References

[1] P. Houston, *Chemical Kinetics and Reaction Dynamics*, Dover Publications Inc., 2006.

[2] http://nobelprize.org/nobel_prizes/chemistry/laureates/1986/.

[3] http://nobelprize.org/nobel_prizes/chemistry/laureates/2007/press.html.

[4] M. Gratzel, *J. Photochem. Photobiol. C: Photochem. Rev.*, 2003, **4**, 145.

[5] G. Porter, *Proceedings of the Royal Society of London, series A, Mathematical and Physical Sciences*, 1950, **200**, 284.

[6] M. M. Wolff and W. E. Stephens, *Rev. Sci. Instrum.*, 1953, **24**, 616.

[7] A. E. Cameron and D. F. E. Jr., *Rev. Sci. Instrum.*, 1948, **19**, 605.

[8] W. C. Wiley and I. H. McLaren, *Rev. Sci. Instrum.*, 1955, **26**, 1150.

[9] G. Hancock, P. J. Pearson, G. A. D. Ritchie and D. F. Tibbetts, *Phys. Chem. Chem. Phys.*, 2003, **5**, 5386.

[10] J. K. Cashion and J. C. Polanyi, *J. Chem. Phys.*, 1958, 455.

[11] J. K. Cashion and J. C. Polanyi, *J. Chem. Phys*, 1959, **30**, 316.

[12] M. N. R. Ashfold and J. E. Baggot, *Molecular Photodissociation Dynamics*, Royal Society of Chemistry, London, 1987.

[13] N. J. Turro, V. Ramamurthy and J. C. Sciano, *Principles of Modern Molecular Photochemistry: An Introduction*, University Science Books, 2008.

[14] A. I. Chichinin, K. H. Gericke, S. Kauczok and C. Maul, *Int. Rev. Phys. Chem.*, 2009, **28**, 607.

[15] P. L. Houston, *J. Phys. Chem.*, 1987, **91**, 5388.

[16] G. E. Hall and P. L. Houston, *Annu. Rev. Phys. Chem.*, 1989, **40**, 375.

[17] A. J. Orr-Ewing and R. N. Zare, *Annu. Rev. Phys. Chem.*, 1994, **45**, 315.

[18] J. P. Simons, *J. Phys. Chem.*, 1987, **91**, 5378.

[19] R. N. Zare and D. R. Herschbach, *Proceedings of the IEEE*, 1963, **51**, 173.

[20] J. Solomon, *J. Chem. Phys.*, 1967, **47**, 889.

[21] A. J. R. Heck and D. W. Chandler, *Annu. Rev. Chem. Phys*, 1995, **46**, 335.

[22] M. N. R. Ashfold, N. H. Nahler, A. J. Orr-Ewing, O. P. J. Vieuxmaire, R. L. Toomes, T. N. Kitsopoulos, I. A. Garcia, D. A. Chestakov, S. M. Wuc and D. H. Parker, *Phys. Chem. Chem. Phys.*, 2005, **8**, 26.

[23] D. Townsend, W. Li, S. K. Lee, R. L. Gross and A. G. Suits, *J. Phys. Chem. A*, 2005, **109**, 8661.

[24] A. G. Suits and O. S. Vasyutinskii, *Chem. Rev.*, 2008, **108**, 3706.

[25] H. Reisler, *Annu. Rev. Phys. Chem.*, 2009, **60**, 39.

[26] http://nobelprize.org/nobel_prizes/chemistry/laureates/1922/aston.html.

[27] L. J. Butler and D. M. Neumark, *J. Phys. Chem.*, 1996, **100**, 12801.

[28] R. W. Diesen, J. C. Ware and S. E. Adler, *J. Chem. Phys.*, 1969, **50**, 3635.

[29] G. King, T. A. A. Oliver, M. G. D. Nix and M. N. R. Ashfold, *J. Phys. Chem. A*, 2009, **113**, 7984.

[30] S. J. Goncher, D. T. Moore, N. E. Sveum and D. M. Neumark, *J. Chem. Phys.*, 2008, **128**, 114303.

[31] S. J. Riley and K. R. Wilson, *Faraday Discuss. Chem. Soc*, 1972, **53**, 132.

[32] G. Hancock, P. J. Pearson, G. A. D. Ritchie and D. F. Tibbetts, *Phys. Chem. Chem. Phys.*, 2003, **5**, 5386.

[33] L. Schnieder, W. Meier, K. H. Welge, M. N. R. Ashfold and C. M. Western, *J. Chem. Phys.*, 1990, **92**, 7027.

[34] D. W. Chandler and P. L. Houston, *J. Chem. Phys.*, 1987, **87**, 1445.

[35] J. J. Lin, J. Zhou, W. Shiu and K. Liu, *Rev. Sci. Instrum.*, 2003, **74**, 2495.

[36] G. Wu, W. Zhang, H. Pan, Q. Shuai, B. Jiang, D. Dai and X. Yang, *Rev. Sci. Instrum.*, 2008, **79**, 94104.

[37] N. T. Form, B. J. Whitaker, L. Poisson and B. Soep, *Phys. Chem. Chem. Phys.*, 2006, **8**, 2925.

[38] S. P. K. Koehler, Y. Ji, D. Auerbach and A. M. Wodtke, *Phys. Chem. Chem. Phys.*, 2009, **11**, 7540.

[39] P. H. Kobrin, G. A. Schick, J. P. Baxter and N. Winograd, *Rev. Sci. Instrum.*, 1986, **57**, 1354.

[40] L. J. Rogers, M. N. R. Ashfold, Y. Matsumi, M. Kawasaki and B. J. Whitaker, *J. Chem. Soc. Faraday Trans*, 1996, **92**, 5181.

[41] A. Garcia-Vela, R. B. Gerber, D. G. Imre and J. J. Valentini, *Phys. Rev. Lett.*, 1993, **71**, 931.

[42] A. T. J. B. Eppink and D. H. Parker, *Rev. Sci. Instrum.*, 1997, **68**, 3477.

[43] A. J. van den Brom, T. P. Ratzikis and M. H. M. Janssen, *J. Chem. Phys.*, 2005, **123**, 164313.

[44] R. A. Rose, A. J. Orr-Ewing, C. H. Yang, K. Vidma, G. C. Groenenboom and D. H. Parker, *J. Chem. Phys.*, 2009, **130**, 34307.

[45] H. Kuhlewind, A. Kiermeier and H. J. Neusser, *J. Chem. Phys.*, 1986, **85**, 4427.

[46] M. L. Lipciuc, A. J. van den Brom, L. Dinu and M. H. M. Janssen, *Rev. Sci. Instrum.*, 2005, **76**, 123103.

[47] B. D. Leskiw, M. H. Kim, G. E. Hall and A. G. Suits, *Rev. Sci. Instrum.*, 2005, **76**, 104101.

[48] L. M. Smith, D. R. Keefer and S. I. Sudharsan, *J. Quant. Spectrosc. Radiat. Transfer*, 1988, **39**, 367.

[49] D. J. D. Rosier and A. Klug, *Nature*, 1968, **217**, 130.

[50] R. N. Strickland and D. W. Chandler, *Applied Optics*, 1991, **30**, 1811.

[51] R. N. Bracewell, *The Fourier Transform and its Applications*, McGraw Hill, 1986.

[52] M. P. Ekstrom, *Digital Image Processing Techniques*, Orlando: Academic, 1984.

[53] L. M. Smith, *IEEE Transactions on Information Theory*, 1988, **34**, 158.

[54] A. G. Suits, R. L. Miller, L. S. Bontuyan and P. L. Houston, *J. Chem. Soc. Faraday. Trans.*, 1993, **89**, 1443.

[55] V. Dribinski, A. Ossadtchi, V. A. Mandelshtam and H. Reisler, *Rev. Sci. Instrum.*, 2002, **73**, 2634.

[56] S. Manzhos and H. P. Loock, *Computer Physics Communications*, 2003, **154**, 76.

[57] T. Kinugawa and T. Arikawa, *J. Chem. Phys.*, 1991, **96**, 4801.

[58] K. Tonokura and T. Suzuki, *Chem. Phys. Lett.*, 1994, **224**, 1.

[59] D. Townsend, M. P. Minitti and A. G. Suits, *Rev. Sci. Instrum.*, 2003, **74**, 2530.

[60] D. A. Chestakov, S. M. Wu, G. Wu, D. H. Parker, A. T. J. B. Eppink and T. N. Kitsopoulos, *J. Phys. Chem. A*, 2004, **108**, 8100.

[61] M. A. Young, *J. Chem. Phys.*, 1995, **102**, 7925.

[62] C. R. Gebhardt, T. P. Rakitzis, P. C. Samartzis, V. Ladopoulos and T. N. Kitsopoulos, *Rev. Sci. Instrum.*, 2001, **72**, 3848.

[63] P. Atkins and J. D. Paula, *Atkin's Physical Chemistry, 8^{th} Ed.*, Oxford University Press, 2006.

[64] G. Scoles, D. Bassi, U. Buck and D. C. Laine, *Atomic and Molecular Beam Methods*, Oxford University Press, USA, 1988.

[65] J. Libuda and H. J. Freund, *Surface Science Reports*, 2005, **57**, 157.

[66] J. Libuda and H. J. Freund, *Surface Science Reports*, 2005, **57**, 157.

[67] G. Scoles, *Atomic and Molecular Beam Methods*, OUP, 1988.

[68] J. M. Hollas, *High Resolution Spectroscopy*, Wiley-Blackwell, 1998.

[69] A. E. Siegman, *Lasers*, University Science Books, 1986.

[70] P. W. Miloni and J. H. Eberly, *Laser Physics*, Wiley, 2010.

[71] J. L. Wiza, *Nuclear Instruments and Methods*, 1979, **162**, 587.

[72] W. Li, S. D. Chambreau, S. A. Lahankar and A. G. Suits, *Rev. Sci. Instrum.*, 2005, **76**, 63106.

[73] http://sine.ni.com/np/app/flex/p/ap/global/lang/en/pg/1/docid/nav-77/.

[74] B. L. Yoder, A. H. C. West, B. Schlappi, E. Chasovskikh and R. Signorell, *The Journal of Chemical Physics*, 2013, **138**, .

[75] G. M. Barrow and E. A. Yerger, *J. Am. Chem. Soc.*, 1954, **76**, 5211.

[76] V. Madison and K. D. Kopple, *J. Am. Chem. Soc.*, 1980, **102**, 4855.

[77] M. L. Aucott, A. McCulloch, T. E. Graedel, G. Kleinman, P. Midgley and Y. Li, *J. Geophys. Res.*, 1999, **104**, 8405.

[78] M. A. K. Khalil, R. M. Moore, D. B. Harper, J. M. Lobert, D. J. Erickson, V. Koropalov, W. T. Sturges and W. C. Keene, *J. Geophys. Res.*, 1999, **104**, 8333.

[79] M. J. Molina and F. S. Rowland, *Nature*, 1974, **249**, 810.

[80] R. S. Mulliken, *J. Chem. Phys.*, 1940, **8**, 382.

[81] X. Yang, P. Felder and J. R. Huber, *Chem. Phys.*, 1994, **189**, 127.

[82] F. Taketani, K. Takahashi and Y. Matsumi, *Phys. Chem. A*, 2005, **109**, 2855.

[83] Y. Matsumi, K. Tonokura, M. Kawasaki, G. Inoue, S. Satyapal and R. Bersohn, *J. Chem. Phys.*, 1991, **94**, 2669.

[84] S. Deshmukh and W. P. Hess, *J. Photochem. Photobiol. A: Chem.*, 1994, **80**, 17.

[85] M. Kawasaki, K. Suto, Y. Sato, Y. Matsumi and R. Bersohn, *J. Phys. Chem.*, 1996, **100**, 19853.

[86] R. A. Brownsword, M. Hillenkamp, T. Laurent, R. K. Vatsa, H. Volpp and J. Wolfrum, *J. Phys. Chem. A*, 1997, **101**, 5222.

[87] C. Romanzin, B. Gans, S. Douin, S. Boy-Pronne and D. Gauyacq, *Chem. Phys.*, 2008, **351**, 77.

[88] D. Townsend, S. K. Lee and A. G. Suits, *J. Phys. Chem. A*, 2004, **108**, 8106.

[89] A. Kramida, Y. Ralchenko, J. Reader and N. A. Team, *NIST Atomic Spectra Database (version 5.0)*, 2012, http://physics.nist.gov/asd/.

[90] Y. Matsumi, K. Tonokura and M. Kawasaki, *J. Chem. Phys.*, 1992, **97**, 1065.

[91] J. R. Roscioli and D. J. Nesbitt, *Faraday Discussions*, 2011, **150**, 471.

[92] http://www.bnl.gov/chemistry/programs/Surface_dynamics.asp.

[93] http://vallance.chem.ox.ac.uk/CVresearch.html#Surface%20imaging.

[94] D. Corr and D. C. Jacobs, *Rev. Sci. Instrum.*, 1992, **63**, 1969.

[95] T. Mull, B. Baumeister, M. Menges, H. J. Freund, D. Weide, C. Fischer and P. Andresen, *J. Chem. Phys.*, 1992, **96**, 9.

[96] S. W. Rosencrance, D. E. Riederer, R. Chatterjee, C. He, N. Winograd and Z. Postawa, *Nuclear Instruments and Methods in Physics Research B*, 1995, **101**, 137.

[97] D. Irimia, R. Kortekaas and M. H. M. Janssen, *PCCP*, 2009, **11**, 3958–3966.

[98] B. Yan, P. F. Claus, B. G. van Oorschot, L. Gerritsen, A. T. Eppink, S. Y. van de Meerakker and D. H. Parker, *Rev. Sci. Instrum.*, 2013, **84**, 023102.

[99] D. A. Dahl, *International Journal of Mass Spectrometry*, 2000, **200**, 3.

[100] http://simion.com.

[101] E. M. McCash, *Surface Chemistry*, Oxford University Press, 2001.

[102] D. P. Woodruff and T. A. Delchar, *Modern Techniques of Surface Science*, University of Cambridge Press, 1994.

[103] J. T. Y. Jr., *Experimental Innovations in Surface Science*, AIP Press, 1997.